UNIVERSIDAD COMPLUTENSE DE MADRID
FACULTAD DE CIENCIAS QUÍMICAS
Departamento de Química Física

TESIS DOCTORAL

Raman spectroscopy: a versatile tool in the multianalitycal characterisation of nuclear fuel

Espectroscopía Raman : herramienta versátil en la caracterización multianalítica del combustible nuclear

MEMORIA PARA OPTAR AL GRADO DE DOCTOR

PRESENTADA POR

Jone Miren Elorrieta Baigorri

Directores

Joaquín Cobos Sabaté
Valentín García Baonza

Madrid 2019

Universidad Complutense de Madrid
Facultad de Ciencias Químicas
Departamento de Química Física

Raman spectroscopy: A versatile tool in the multianalytical characterisation of nuclear fuel

Espectroscopía Raman: Una herramienta versátil en la caracterización multianalítica del combustible nuclear

---

Jone Miren Elorrieta Baigorri

Directores:

Dr. Joaquín Cobos Sabaté

Prof. Valentín García Baonza

Manuscrito presentado para optar al grado de Doctora

Madrid, 2018

GOBIERNO DE ESPAÑA
MINISTERIO DE ECONOMÍA, INDUSTRIA Y COMPETITIVIDAD
Ciemat
Centro de Investigaciones Energéticas, Medioambientales y Tecnológicas

Para ellas…

Ametsik gabeko bizitza, izarrik gabeko gaua.

Nothing in life is to be feared, it is only to be understood.
Now is the time to understand more, so that we may fear less.

Marie Skłodowska Curie

Look up at the stars and not down at your feet. Try to make sense of what you see, and wonder about what makes the universe exist. Be curious.

Stephen Hawking

Agradecimientos/Acknowledgements

A ti que estás leyendo este manuscrito, o al menos los agradecimientos por curiosidad, te pregunto: "¿tú has hecho algo por mi tesis?". Es una larga historia…Seguramente sí, aunque puedas pensar que no. Basta con que hayas pasado por mi vida durante estos últimos cuatro años para que hayas contribuido, mucho o poco, ya sea por distintos motivos: enseñarme, guiarme, ayudarme, aportarme ideas, resolverme dudas, apoyarme en malos o buenos momentos, soportarme, compartir unas cañas, jugar conmigo a fútbol, o simplemente estar ahí en un momento dado haciéndome sonreír.

De cualquier forma, algunas personas obviamente merecen una mención especial, así que aquí intentaré agradecerles personalmente su aportación. Espero que no se me olvide nadie.

A mis directores: **¡Gracias!** A Joaquín, por haberme dado la oportunidad de entrar en el CIEMAT y empezar este proyecto de tesis, y dirigirme durante el camino. A Valen, por haber sacado tiempo para mí de donde no lo había y haberme aportado seguridad desde su experiencia y conocimiento de la espectroscopía Raman.

A l@s de casa: **Eskerrik asko!** A ama y aita, por haberme dado todo lo que tengo y todo lo que soy. A mi hermana Irantzu, la primera Dra. Elorrieta de casa, por haber sido siempre mi ejemplo a seguir (creo que 2018 va a ser un gran año para las dos, ¿eh?). A mi amama, mis tíos y mi prima, por haber estado también siempre ahí. Y por supuesto a Eider, por ser mi gran apoyo y aguantarme durante estos años.

A la gente del CIEMAT: **¡Muchas gracias!** En primer lugar, a Laura (más conocida como LauRaman). Me faltan las palabras para agradecerte tu infinita ayuda y todo lo que he aprendido de ti. En segundo lugar, a mi inigualable compañera de despacho y mejor persona, Nieves, que siempre está dispuesta a echar una mano y a animar con pequeños detalles. También, cómo no, al resto de personas que pertenecen o han pertenecido en algún momento a la URRAA; especialmente, a mi gran compi Iván, Ban-Ana (no olvidaré esos momentos de la hora del café), Hitos, Sofi, Lorena, Sergio, Jose, Juan, Amadeo, Lauri y Luis. Y a mis tronkis Natalia y Eva. Gracias por todos los

grandes momentos que hemos pasado junt@s, me da mucha pena que esta etapa acabe. Por supuesto no me olvido de l@s jóvenes molones, compartiendo esas comidas de martes precarios, con especial mención a l@s que estuvieron al principio de la creación del grupo: Natalia, Marta, Naiara, Isa, Marcos, Julio, Mónica, Lanting...¡Y tampoco puedo olvidarme del equipazo de fútbol "Recreativos Culturetas"!

To my colleagues at JRC Karlsruhe: **Thank you and Grazie!** First, to Dario, the best supervisor I could have ever imagined for my research stay, both professionally and personally. I owe you too much. Also to the rest of the "Safety of Nuclear Fuel Unit", especially to Mohamed for his huge help. I should not forget to thank my wivies Nadya and Joaquina, for sharing such great moments, and all the components of the Fußball Team, for making my stay at Karlsruhe more enjoyable. E, naturalmente, grazie mille alla grande famiglia italiana all'ITU! In particolare a Luana, per tutti i momenti divertenti (e alcuni non così tanto) dentro e fuori dall'ufficio, e a Luca, per il tuo sorriso illimitato che incoraggia chiunque.

A mis amig@s en general: **¡Gracias!** Por estar ahí, preguntar mil veces por la tesis, preocuparos y, en resumen, ¡por hacerme la vida más feliz!

Espero que, a quien se atreva a seguir adelante con las siguientes páginas, le resulte medianamente amena esta tesis. ¡Ánimo y gracias!

Jone M. Elorrieta

Outline

Summary

The present thesis, entitled “Raman spectroscopy: a versatile tool in the multianalytical characterisation of nuclear fuel”, consists of four main blocks. The first part concerns the background information and the consequent introduction to the issue under discussion, emphasising the objectives to be fulfilled. The second part is devoted to the methodology followed throughout the different enclosed studies, in particular with regard to the employment of the Raman spectroscopy technique. Then, the third part corresponds to the core results obtained and the fourth one to the overall conclusions drawn from these outcomes.

The oxidation of uranium dioxide (UO_2), a nuclear fuel used in the majority of nuclear plants in operation across the world, has always raised great interest. This is due to the potential risks that such process might provoke in the event of the presence of any undetected defect in the fuel elements or of a complete shielding failure during its storage after being irradiated in the reactor. If this occurred under dry interim storage conditions, as in the case of the planned Spanish ATC, the contact of atmospheric oxygen with the spent nuclear fuel (SNF), which presents a large physicochemical complexity and high radiotoxicity, might induce the oxidation of the UO_2 matrix up to U_3O_8. The latter phenomenon is facilitated by the effect of the high temperature aroused from the SNF radioactive decay heat. Given that the conversion to U_3O_8 entails a volume increase of ~36%, SNF integrity loss (pulverisation) might take place, hindering its future retrieval and management, either with the aim of reprocessing the SNF or refurbishing it for its final disposal in geological formations.

In spite of the wide variety of studies that have been carried out in this regard, a more specific characterisation of the different uranium oxides involved in UO_2 oxidation is still necessary, for the purpose of gaining a better understanding of the structural and chemical evolution of the system. Moreover, it is important to know how the presence of those transuranic elements (Pu, Am…) embedded in the SNF matrix, which are formed in small proportions during fission in the nuclear reactor, may affect such reaction.

Hence, this work presents various advances in the analysis of the SNF matrix and its oxidation as a function of distinct factors (namely temperature

and the presence of transuranic elements), making use of Raman spectroscopy as the primary characterisation technique. Specifically, the main studies performed and the general results attained from them can be summarised as follows: 1) Analysis of the influence of oxygen incorporation into UO_2, obtaining an oxidation degree estimation method for the hyperstoichiometry range; 2) Application of the previous method for *in situ* tracking the early-stage oxidation of UO_2, considering the additional effect of temperature; 3) Development of a laser heating method for the purpose of *in situ* characterising the oxidation reaction of UO_2 and simultaneously estimating the temperature at which the different oxidation products are formed; 4) Evaluation of the temperature effect, under anoxic atmosphere, on the Raman spectrum of UO_2; 5) Analysis of the effect caused by Pu incorporation into UO_2, especially with regard to its influence on the mixed dioxide oxidation; and 6) Analysis of the effect caused by Ce incorporation into UO_2, especially with regard to its influence on the mixed dioxide oxidation, as well as the assessment of $(U, Ce)O_2$ as an appropriate surrogate for $(U, Pu)O_2$.

As a matter of fact, it is evident from the obtained outcomes that Raman spectroscopy can be regarded as a useful and versatile tool for analysing the SNF condition and its stability against oxidation under dry interim storage conditions. This becomes a key point for properly and safely refurbishing the SNF after its future retrieval from the temporary storage, either for its reprocessing or its final deep geological disposal.

Resumen

La presente tesis, titulada “Espectroscopía Raman: una herramienta versátil en la caracterización multianalítica del combustible nuclear”, consiste de cuatro bloques principales. La primera parte concierne los antecedentes y la consecuente introducción al tema en discusión, enfatizando los objetivos a cumplir. La segunda parte está dedicada a la metodología seguida a lo largo de los distintos estudios incluidos, en particular en lo que se refiere al empleo de la técnica de espectroscopía Raman. Así, la tercera parte corresponde a los resultados fundamentales obtenidos y la cuarta a las conclusiones generales deducidas de ellos.

La oxidación del dióxido de uranio (UO_2), combustible nuclear usado en la mayoría de centrales nucleares en operación en el mundo, ha suscitado siempre gran interés. Esto es debido a los potenciales riesgos que dicho proceso podría provocar si llegara a producirse, durante su almacenamiento una vez irradiado en el reactor, la presencia de un defecto desapercibido en los elementos combustibles o un fallo de barreras de contención. Si esto ocurriera en condiciones de almacenamiento temporal en seco, como en el caso del planeado ATC español, el contacto del oxígeno atmosférico con el combustible irradiado (CI), el cual presenta una gran complejidad físico-química y alta radiotoxicidad, podría inducir a la oxidación de la matriz de UO_2 hasta U_3O_8. Este fenómeno se ve facilitado por el efecto de la alta temperatura generada por el calor residual, proveniente del decaimiento radiactivo del CI. Dado que esta conversión a U_3O_8 conlleva un aumento del ~36% en volumen, podría llegar a ocurrir la pérdida de integridad (pulverización) del CI, dificultando su futura recuperación y gestión, tanto con el fin de reprocesarlo como de su acondicionamiento para un almacenamiento definitivo en formaciones geológicas.

A pesar de la gran variedad de estudios llevados a cabo, aún resulta necesaria una caracterización más específica de los distintos óxidos de uranio que toman parte en la oxidación del UO_2, con el objetivo de lograr una mejor comprensión de la evolución estructural y química del sistema. Asimismo, es importante conocer cómo puede afectar a dicha reacción la presencia de elementos transuránicos (Pu, Am…) incorporados en la matriz del CI, los

cuales se forman en pequeñas proporciones durante la fisión en el reactor nuclear.

Por ello, este trabajo presenta diversos avances en el análisis de la matriz del CI y de su oxidación en función de distintos factores (principalmente temperatura y presencia de elementos transuránicos), haciendo uso de la espectroscopía Raman como técnica principal de caracterización. En concreto, los diferentes estudios realizados y los resultados generales logrados a partir de éstos se resumen a continuación: 1) Análisis de la influencia de la incorporación de oxígeno en el UO_2, obteniendo un método de estimación del grado de oxidación en el rango de hiperestequiometría; 2) Aplicación del método anterior para seguir *in situ* la oxidación preliminar del UO_2, considerando el efecto adicional de la temperatura; 3) Desarrollo del método de calentamiento por láser con el fin de caracterizar *in situ* la reacción de oxidación del UO_2 y estimar simultáneamente la temperatura a la que se forman los distintos productos de oxidación; 4) Evaluación del efecto de la temperatura, bajo atmósfera anóxica, en el espectro Raman del UO_2; 5) Análisis del efecto causado por la incorporación de Pu en el UO_2, en particular con respecto a su influencia en la oxidación del dióxido mixto; y 6) Análisis del efecto causado por la incorporación de Ce en el UO_2, en particular con respecto a su influencia en la oxidación del dióxido mixto, así como la evaluación del $(U, Ce)O_2$ como análogo adecuado para el $(U, Pu)O_2$.

De esta forma, a partir de los resultados obtenidos resulta evidente que la espectroscopía Raman puede considerarse una herramienta útil y versátil a la hora de analizar el estado del combustible nuclear y su estabilidad frente a la oxidación en condiciones de almacenamiento temporal en seco. Este hecho constituye un punto clave para poder acondicionar apropiadamente y de forma segura el CI tras su futura recuperación de dicho almacén temporal, tanto a efectos de reprocesarlo como de depositarlo de forma definitiva en el almacenamiento geológico profundo.

List of main abbreviations

ATC	Spanish centralised temporary storage
BSE	BackScattered-Electron detector
CCD	Charge-Coupled Device
CEA	French atomic energy commission
CF	Crystal Field
CTD	Charge Transfer Device
DLS	Dynamic Light Scattering
EBS	Ethyl Bis Stearamide
EDS	Energy Dispersive X-ray Spectroscopy
fcc	Face Centred Cubic
FP	Fission Products
GCR	Gas Cooled Reactor
HLW	High Level Waste
IR	Infrared
JRC	Joint Research Centre
LWR	Light Water Reactor
MOX	Mixed OXide fuel
NA	Numerical Aperture
ND	Neutral Density
SE	Secondary-Electron detector
SEM	Scanning Electron Microscopy
SNF	Spent Nuclear Fuel
UV	UltraViolet
XAS	X-ray Absorption Spectroscopy
XRD	X-Ray Diffraction

Part 1

Key concepts and objectives

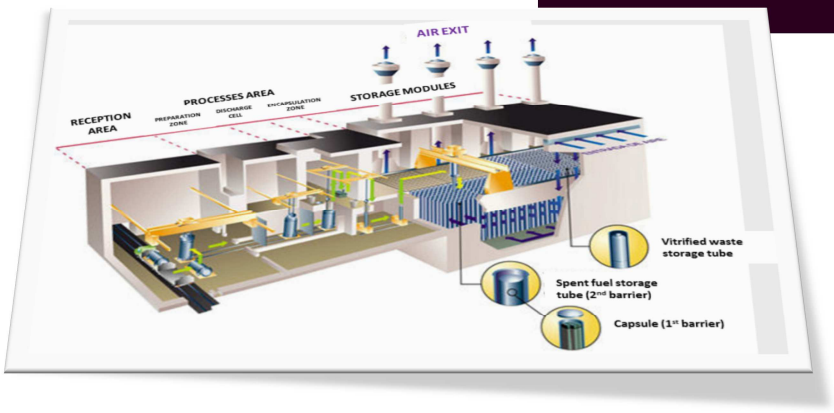

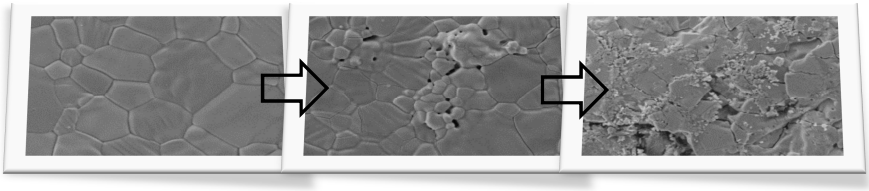

After Hiroshima and Nagasaki bombings in 1945, the fear towards nuclear energy started to spread amongst the population; some decades later, due to nuclear disasters such as the ones occurred in Three Mile Island (1979), Chernobyl (1986) and, especially, Fukushima (2011), the debate on nuclear electricity generation took on particular relevance.

Nuclear energy is considered a reliable and non-polluting source, what constitutes a positive point with regard to climate change. Nevertheless, it presents two fundamental problems that deeply concern to society: the safety of nuclear power plants and the management of the radioactive waste generated throughout the nuclear fuel cycle.

The present thesis is developed in the field of the second issue, specifically focusing on the Raman spectroscopy analysis of the spent fuel stability under dry interim storage conditions.

1.1. Spent nuclear fuel management. Alternatives

The production of nuclear waste in the form of spent nuclear fuel (SNF) is an intrinsic feature of any current nuclear plant. Every one-two years, between a third and a quarter of the fuel elements in a nuclear reactor core are replaced by new ones [1]. Those removed are considered as "spent fuel". Nonetheless, "irradiated fuel" would be a more appropriate name since, although no longer usable from a safety and economic perspective, their energy-production capacity is not completely spent.

Almost all the nuclear reactors currently in operation around the world use uranium as nuclear fuel, which depending on the kind of reactor can be present in either oxide or metallic pellet form, and isotopically enriched (with a greater proportion of U^{235} than the 0.7% natural content of uranium) or not. The fuel elements introduced into the reactor core are composed of a set of metallic rods containing the latter fuel pellets, which are vertically stacked. The metallic rod itself is commonly named fuel cladding and it is considered the primary protective barrier for the nuclear fuel. By way of example, Figure 1.1 shows the components of a conventional UO_2 fuel element/assembly.

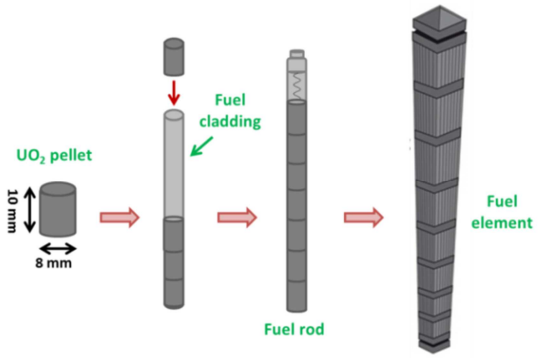

Fig. 1.1. Scheme of the component parts of a conventional UO_2 fuel element.

During fuel irradiation in the reactor, both neutron capture and nuclear fission reactions take place, giving rise to fission products (FP), activation products, and the generation of plutonium and other minor actinides such as neptunium, americium and curium, that contribute significantly to the fuel radiotoxicity. All this together with a great heat generation that leads to a thermal gap of ~1300ºC between the fuel centre and its surface [2]. In this way, the resulting SNF contains practically all the elements of the periodic table, being the major part of them in continuous evolution until they attain stability; in other terms, emitting ionising radiation and the known as decay heat throughout their radioactive decay process. The radiotoxic inventory evolution of a UO_2 spent fuel with a burnup (irradiation to which the fuel is subjected in order to extract a given electric energy amount) of 60 GWd/tU is reflected in Figure 1.2 [3].

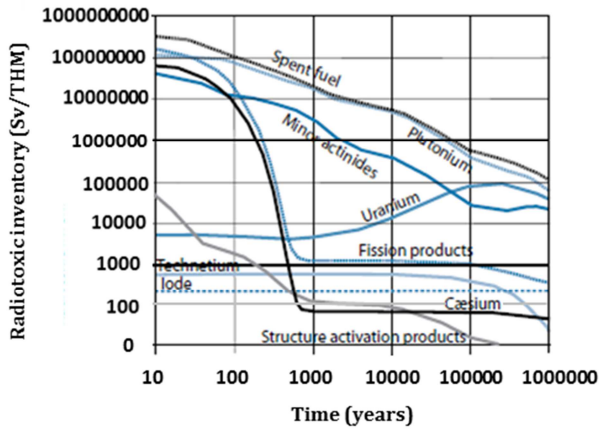

Fig. 1.2. Radiotoxic inventory evolution of a UO_2 spent fuel with a 60 MWd/tU burnup *[expressed in Sieverts per tonne of initial heavy metal (uranium) (Sv/THM) versus time (years)]* [3].

Moreover, the original fuel suffers significant microstructural modifications owing to the physicochemical changes –swelling, cracking (see Figure 1.3), recrystallization, defects formation, etc.– caused by both the irradiation and thermal cycles undergone in the reactor. Likewise, the fuel cladding experiences embrittlement, mainly due to hydrogen absorption during irradiation (see Figure 1.3) [4].

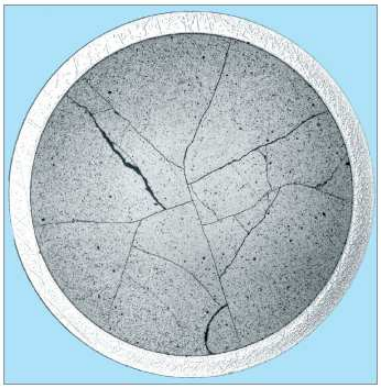

Fig. 1.3. Radial optical microscopy image of a SNF, evidencing the existence of radial cracks in the oxide and hydrides in the cladding [4].

Owing to the high complexity and radiotoxicity of the SNF, it is clear that its management is not a trivial matter. In all cases, right after its removal from the core, the SNF is kept for several years under water in the reactor pool (Figure 1.4) with the aim of ensuring both cooling and radiation shielding [5].

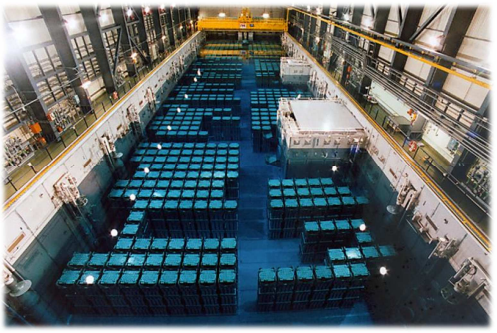

Fig. 1.4. Storage of SNF elements in a nuclear reactor pool [6].

Thereafter, two management alternatives are considered, which directly rely on the policies of each country: the once-through (or open) fuel cycle and the

closed fuel cycle. The main difference between them lies in the reprocessing, which is deemed by the closed fuel cycle for the purpose of recycling the usable part of the SNF and reducing the waste volume and radiotoxicity, but not by the once-trough cycle, whose only target is the safe storage of the SNF as it is until its permanent disposal. Anyhow, regardless of the cycle followed, after its temporary storage in the reactor pool the SNF must be transferred to interim storage facilities (concerning either dry or wet storage), where it will be kept until it is ultimately reprocessed or prepared for its final disposal [7]. Figure 1.5 shows an overview of the different steps involved in the nuclear fuel cycle, which comprises from the mining process up to the final disposal of the SNF, taking into account the two possible cycles previously described.

Fig. 1.5. The nuclear fuel cycle: from mining to final disposal of the SNF. Once-through and closed cycles differ in the reprocessing and recycling steps, which only the latter undertakes [6].

Since the SNF contains about 96% of uranium and 1% of plutonium [5] and these materials can still be recycled due to their remaining energy content, some countries, *e.g.* France, United Kingdom or Japan, have opted for reprocessing the SNF in order to recover them (conventional closed cycle). In this way, uranium can be reused as fuel, and the same occurs with the recovered plutonium, which mixed with uranium can be used as mixed oxide fuel (MOX) in current nuclear reactors. On the other hand, the residual high level waste (HLW) is solidified in

appropriate matrix forms such as vitreous forms, in order to both immobilise it and reduce its volume for its eventual management.

A more advanced closed cycle would be based on the partitioning (separation from the SNF) of the main actinides and long-lived FP, recycling them in the form of advanced fuels for their transmutation (irradiation) in fast neutron reactors [8]. Doing so, the volume and radiotoxicity of the HLW would be reduced to a large extent (see Figure 1.2) and further energy would be produced. Although this challenging alternative has not yet been commercialised, significant research is being undertaken in this regard [8].

As for the mentioned final disposal, a general consensus has been reached at the global level, consisting in the deposition of the nuclear waste –being this either the SNF as it is or the vitrified waste coming from the reprocessing– in geologic formations where a multi-barrier protection system is considered (see Figure 1.6) [9]. This is the so-called deep geological repository. Its expected life time is in the order of a million years, time needed for its radioactivity to decay down to the inherent levels of natural uranium.

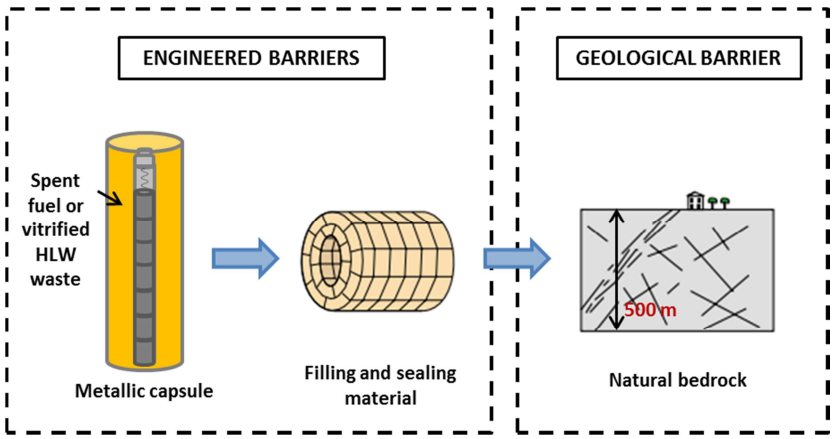

Fig. 1.6. Scheme of the multi-barrier design of a deep geological repository (adapted from [2]).

To the present day, Finland is the only country which is already carrying out construction activities on their deep geological repository (ONKALO, at Olkiluoto nuclear plant site), planning to put it into operation in the early 2020s [10].

1.2. Spanish strategy on SNF management

In Spain there are, at present, seven nuclear reactors in operation (see Figure 1.7), distributed in five nuclear power plants across the country and providing a total power of ~7400 MWe [11]. As shown in Figure 1.7, three other reactors have already been disconnected, two of which are undergoing dismantling –the third (Garoña) has recently been shut down [12]–. All Spanish reactors belong to the LWR (Light Water Reactor) type, except for one of those out of operation, Vandellós I, which was a GCR (Gas Cooled Reactor) [1].

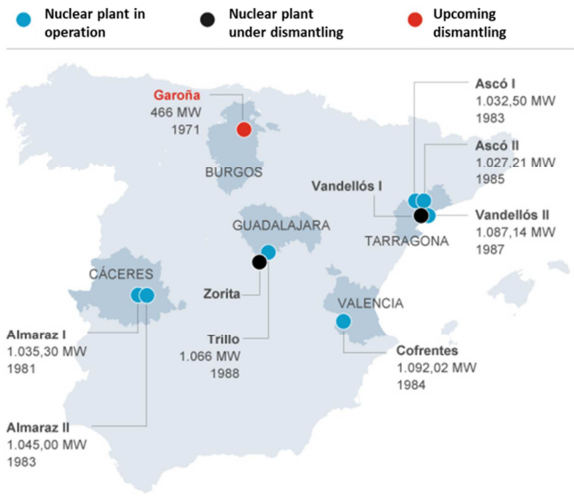

Fig. 1.7. Nuclear power stations in Spain [13].

The traditional nuclear fuel used in LWRs consists of uranium (U^{238}) dioxide, with a slight enrichment of the fissile U^{235} –normally about 3-5%– to sustain the chain reaction [14]. Thus, for the moment, the SNF that needs to be managed in Spain presents a UO_2 matrix, since all the SNF from the GCR-type reactor (based on metallic uranium) was reprocessed several years ago at COGEMA facilities in France for technical reasons [1].

Another potential fuel that could be used in the Spanish reactors (and thus has been taken into consideration as a subject of study in this thesis) is the already mentioned MOX fuel, widely used nowadays by several countries in some of their traditional LWRs. This reprocessed fuel, composed of a mixture of depleted uranium and plutonium, with a content of the latter that can reach up to 12% (containing around two thirds of fissile isotopes, *i.e.* ~50% Pu^{239} and ~15% Pu^{241})

[15], is a suitable alternative to enriched UO_2. Both fuels behave in a similar way, and the single change required for the use of MOX in a conventional LWR is an increase in the amount of control rods (neutrons absorbers to moderate the fission rate). Anyway, the replacement of UO_2 by MOX fuel can only be performed partially, between one-third and half of the core loading, and greater proportions of MOX would require new designs of current or future reactors [15].

In relation to the SNF management, Spain has decided to follow the once-through cycle, planning as part of its strategy the construction of a dry interim centralised storage (where the SNF is expected to be kept until its final deep geological disposal) [1]: the ATC facility –an acronym that comes from its Spanish name, *Almacén Temporal Centralizado*–. The choice of a centralised storage arises as a result of 1) the necessity of complementary temporary storage capacity, given the foreseen saturation of the storage facilities in the nuclear plants, and 2) the preference of storing all the Spanish SNF in one single site, considering the obvious advantages that the management of a sole facility involves in comparison with that of spread facilities. On the other hand, the dry storage option has been chosen on the basis of the wide international experience dealing with dry cask technologies [7].

The ATC is projected to store, during 60 years (being its design life of 100 years), all the SNF and HLW derived from 40 years of Spain's nuclear plants operations [1], as well as those produced over the coming years. Its design is based on a modular and reversible vault storage system (Figure 1.8), similar to that of the HABOG facility currently in operation in the Netherlands, which is being taken as a point of reference [16]. In Spain, such a dry storage is licensed for SNF surface temperatures up to 400ºC [7].

The main feature of the ATC is its multi-barrier and passive –natural convection ventilation– system, which ensures the confinement of the nuclear waste and the facility safety [16]. In particular, after the reception and preparation of the SNF canisters, the fuel rods discharged from them are planned to be inserted into a cask/capsule (first barrier) under inert atmosphere, which will then be kept inside a tube (second barrier) in the storage modules (see Figure 1.8).

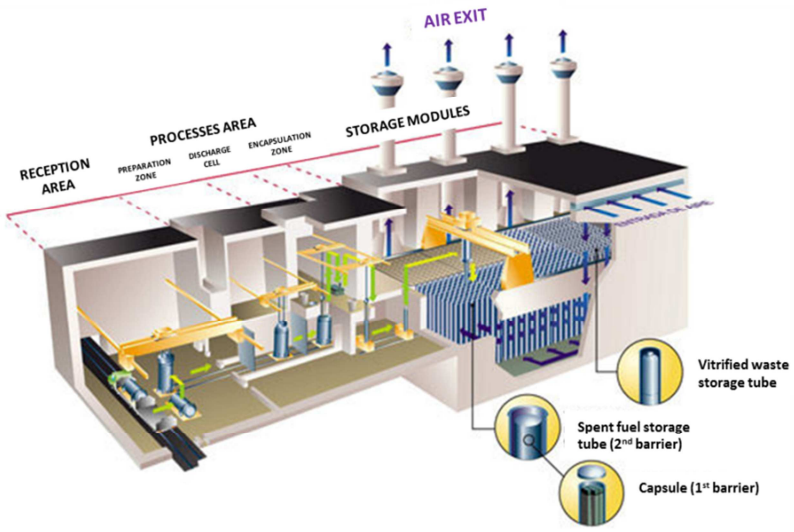

Fig. 1.8. ATC project (Spanish dry interim centralised storage) [16].

Although starting operations were scheduled for 2017, various political issues have led to a delay in its commission, whose date has not yet been defined.

With regard to partitioning and transmutation of long-lived radionuclides in order to reduce the volume and radiotoxicity of the nuclear waste, these alternative management options are not considered relevant enough at the moment [1]. However, it has been established that Spain should follow up the advances carried out in these fields, and accordingly participate in the corresponding international programs.

Furthermore, if a change in the current policies were to take place in the future, implying the willingness to retrieve the SNF for its reprocessing, the reversible feature of the ATC would make it possible. In this context, the condition of the SNF at the time of such retrieval becomes an important point to take into consideration.

1.3. SNF matrix oxidation: A potential risk during dry storage

In order to develop an adequate management of the SNF, it is crucial to know each and every property derived either from its initial features and from the processes it has been subjected to during its irradiation in the reactor.

The stability of the SNF against oxidation is one of those properties that must be taken into account. Most of the transuranic elements (which commonly appear in the form of oxides) and FP, are embedded inside the SNF dioxide matrix [2]. Thus, their potential release will basically depend on the behaviour of this matrix. Given the magnitude of the effects on the population and the environment that such a release might provoke, even the least likely but possible scenarios concerning the dry storage of SNF, as in the case of the ATC, must be examined.

In the event of the presence of any undetected defect in the fuel elements (produced either during fabrication, irradiation cycles, transport or manipulation) or of a complete shielding failure during storage, the SNF might come into contact with the atmospheric oxygen. And it is well known that the UO_2 matrix, which is the one that current Spanish SNF presents, is not thermodynamically stable under these oxidising conditions [17].

UO_2 oxidation reaction has been extensively investigated throughout more than 50 years. One of the reasons why this oxidation has aroused so much interest is the volume increase, of approximately 36%, undergone by the UO_2 SNF matrix through its transformation into U_3O_8 [18]. Under the temperature conditions expected at the ATC, being the maximum licensed temperature of 400ºC [7] as already mentioned, different oxidised phases of uranium might be formed in the presence of oxygen, even possibly occurring full conversion to U_3O_8 (further oxidation to UO_3 can occur, but this oxide is usually not taken into account since it rapidly decomposes in air to the much more stable U_3O_8) [17]. The dashed square in Figure 1.9 shows the latter possible oxides, although it should be noted that no properly updated and consensual phase diagram is available in the literature [19]. The swelling effect suffered by the SNF matrix would then lead to an increased strain on the fuel cladding and, consequently, to an elevated risk of its structural integrity loss [20]. In that case, the safety of the future handling of the SNF –when the time comes to reprocess it or permanently dispose it– would be seriously compromised.

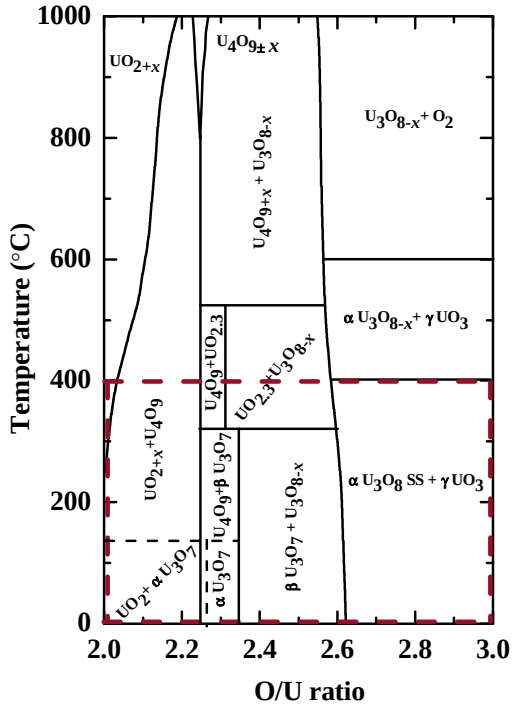

Fig. 1.9. Uranium-oxygen temperature/composition phase diagram (adapted from [18]).

Thereby, a thorough understanding of UO_2 oxidation becomes a matter of priority when assessing the stability of the Spanish SNF under dry interim storage conditions. Likewise, the behaviour against oxidation of other potential fuel matrices in this same scenario, such as the mixed uranium-plutonium dioxide matrix of MOX fuels, is an important subject that should be beared in mind.

1.3.1. UO_2 matrix oxidation

The oxidation of uranium dioxide is described, in general terms, by the following reaction sequence [21]:

$$UO_2 \rightarrow U_4O_9 \rightarrow U_3O_7 \rightarrow U_3O_8 \qquad \text{(Eq. 1.1)}$$

The first and second steps, traditionally regarded as one single step [17], are related to an oxygen diffusion mechanism that leads to the formation of the intermediate U_4O_9 and U_3O_7 phases [17,21], while the final conversion to U_3O_8 corresponds mainly to a nucleation and growth process [17,21,22].

Stoichiometric UO_2 presents a fluorite-type cubic structure with a lattice parameter of around 5.47 Å [23]. In this structure, uranium ions (U^{4+}) occupy the positions corresponding to the fcc (face centre cubic) lattice, whilst oxygen ions (O^{2-}) are located in the tetrahedral positions (see Figure 1.10).

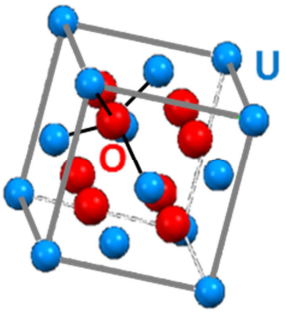

Fig. 1.10. Fluorite-type cubic structure of stoichiometric UO_2.

The incorporation of oxygen into the UO_2 lattice causes a slight distortion in the latter, giving rise to hyperstoichiometric UO_{2+x} [24]. Owing to the excess of hosted oxygen atoms in UO_{2+x}, the cubic crystalline lattice reportedly experiences an overall contraction as the oxidation degree increases [23,25-28]. In this way, the altered cubic structure is maintained up to $x \sim 0.25$ (in UO_{2+x}) [24], limit corresponding to U_4O_9 (also considered a hyperstoichiometric oxide [21]). As shown in Table 1.I, the lattice parameter is significantly reduced in the course of UO_2 oxidation to U_4O_9. In consequence, U_4O_9 is usually known as "superlattice", being capable of hosting a higher amount of oxygen atoms –arranged in clusters– while preserving its cubic structure [29].

It is noteworthy that there are too few experimental data in the literature with regard to the structural transitions taking place over this hyperstoichiometry region. He and Shoesmith [30] studied the defect structures in UO_{2+x} oxides and identified four structural defect regions: i) a random point defect structure [24] ($x \leq 0.05$ (in UO_{2+x})); ii) a non-stoichiometry region where point defects are gradually substituted by Willis 2:2:2 clusters [31] ($0.05 \leq x \leq 0.15$); iii) a mixture of Willis and cuboctahedral clusters [32] ($0.15 \leq x \leq 0.23$); and iv) cuboctahedral clusters ($x \geq 0.23$). However, a more detailed analysis is needed in order to confirm such assumptions and to give further explanation to the maintenance of the cubic structure during the evolution from UO_2 to U_4O_9.

Oxygen integration beyond U_4O_9 generates distortions which lead to a change in the crystallographic system, from cubic to tetragonal, thus resulting in the

U_3O_7 phase (see Table 1.I) [33]. Furthermore, if oxidation still proceeds, the orthorhombic structure of U_3O_8 is formed [34]. The density of U_3O_8 is much lower than that corresponding to UO_2 (see Table 1.I), *i.e.* its volume is much larger, what hence induces spalling and even pulverisation in the case of U_3O_8 formation on pellets (Figure 1.11).

The UO_2 matrix of the SNF thus undergoes this same oxidation process, the only difference lying in the kinetics, which has been observed to change due to the presence of those transuranic elements and FP formed (~5%) during fuel irradiation as well as to the alteration provoked by irradiation itself [35-37].

Table 1.I. Structural characteristics of the main uranium oxides [34].

OXIDE	CRYSTALLOGRAPHIC STRUCTURE	UNIT CELL (Å)	DENSITY (g/cm^3)
UO_2	Cubic	a=5.47	10.96
U_4O_9	Cubic	a=5.44	11.30
U_3O_7	Tetragonal	a=5.47; c=5.39	11.40
U_3O_8	Orthorhombic	a=4.15; b=11.97; c=6.72	8.35

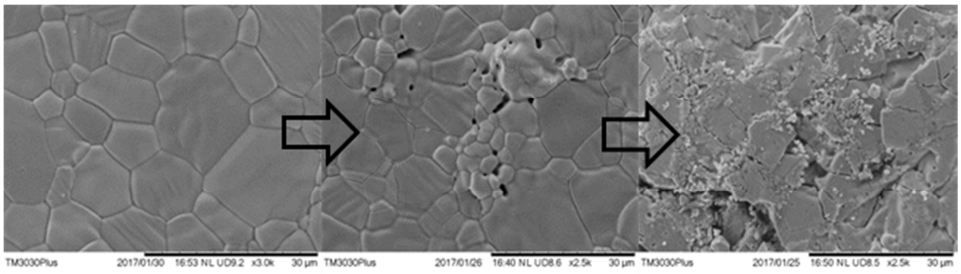

Fig. 1.11. Swelling (middle) and consequent spalling (right) produced by U_3O_8 formation during oxidation of a UO_2 pellet (left). (*SEM images acquired at CIEMAT facilities*)

In particular, the oxidation rate of the UO_2 SNF matrix, when compared to unirradiated UO_2, is considerably higher for the first step related to U_4O_9 formation. This effect is partly on account of the concentration of FP gas bubbles in the grain boundaries, what provides an easy access to oxidation [38]. In contrast, once U_4O_9 is formed there appears to be a certain stabilisation of this phase (which may host oxygen over its corresponding $UO_{2.25}$ stoichiometry, even up to $UO_{2.5}$ [39]) and an inhibition/delay of the complete oxidation to U_3O_8, possibly because of the presence of those elements that have been dissolved in the matrix [34,37,40-42].

1.3.2. MOX fuel matrix oxidation

Uranium-plutonium mixed oxides have also been often investigated with the aim of understanding how the matrix of MOX SNF behaves in air and the effect of Pu content on its oxidation. This kind of studies are of special interest given that they may provide, at the same time, useful information for assessing the influence of the presence of transuranic elements on the oxidation of a conventional UO_2 SNF matrix, taking very low concentrations of Pu as a reference (in the order of 1%, as contained in an UO_2 SNF [5]).

The (U, Pu)O_2 matrix of a MOX SNF can be considered as a UO_2 cubic lattice where U^{4+} ions have been partially substituted by Pu^{4+} ions. Indeed, since PuO_2 oxidation in air has been reported to be quite unlikely [43], it is not surprising that oxidation of such a uranium-plutonium mixed dioxide will be basically governed by the reaction pathways of UO_2 (those described in Section 1.3.1).

Back in the 1970s, the first oxidation analyses performed by X-ray diffraction (XRD) on (U_{1-y}, Pu_y)O_2 oxides with different *y* values between 0.2 and 0.3 [44,45] showed the transformation of the initial MO_2 phase –where M=U, Pu– into two mixed product phases: an orthorhombic M_3O_8 and a cubic M_4O_9 phase (with an observed maximum O/M ratio of ~2.35). Besides, it was found that an increase in Pu content in that range resulted in a hindering effect on the M_3O_8 phase formation, with a consequently lower mechanical degradation of the samples [44]. Other recent studies focused on the reactivity of uranium-plutonium mixed oxides when subjected to air oxidation [46,47] have likewise noticed the strong dependency on Pu content of the M_3O_8 formation resistance and, by extension, of the longer stabilisation of the cubic M_4O_9 phase.

The small amount of studies focused on the latter issue is mainly due to the hazardous feature of plutonium, which complicates both the handling and analysis of this kind of samples considerably. For this reason, analogous measurements are usually performed making use of the non-radioactive CeO_2 as a surrogate for PuO_2, what will be further addressed in Result 6 of Part 3.

In the latest years, owing to the progress achieved in the better adaptation of the different techniques to working under extreme conditions, especially with regard to Raman spectroscopy (as will be detailed in Section 1.4), actual MOX irradiated fuels have been characterised and their air oxidation resistance evaluated [48]. The latter study, whose overall results are in quite good agreement with those obtained on unirradiated (U, Pu)O_2 mixed oxides, has

actually confirmed the significant impact of plutonium content on the stability of the MOX matrix against oxidation. In this way, Pu-enriched agglomerates heated in air under the laser beam present a great structural stability, with M_4O_9 phase stabilisation and no M_3O_8 formation detected.

Although not yet ascertained, the oxidation-hindering behaviour produced by the presence of plutonium might be mainly associated with the effect that these cations cause on the lattice parameter of (U, Pu)O_2, which decreases linearly with the increase in Pu content following Vegard's law (see Table 1.II) –mainly due to the smaller crystal radius Pu^{4+} ions present as compared to the substituted U^{4+} ions– [47,49-55].

Table 1.II. Evolution of the lattice parameter *a* with Pu content in (U_{1-y}, Pu_y)O_2 [50].

***y* (at.% Pu)**	***a* (Å) [XRD]**	***a* (Å) [Vegard's law]**
0	5.470(2)	5.47
7	5.465(2)	5.4648
15	5.457(2)	5.4589
30	5.444(2)	5.4478
50	5.434(2)	5.4330
100	5.398(2)	5.3960

Nonetheless, no systematic Raman analysis of (U, Pu)O_2 oxidation as a function of Pu content has been carried out so far, what would provide deeper understanding on the subject, as hereunder described. For instance, such study would help to confirm whether the effect of Pu on the dioxide oxidation follows a continuous trend as the content of this transuranic element increases.

1.4. Use of Raman spectroscopy for studying nuclear materials

It may be interesting to note at this point that the major part of the studies carried out in relation to the SNF matrix oxidation concerns the use of traditional characterisation techniques, such as thermogravimetry analysis and XRD. In contrast, Raman spectroscopy, which has been shown to be a very helpful technique in several scientific and technological areas, is not yet broadly spread in the field of nuclear materials. As a matter of fact, despite its growing use on

the latter field over the last years [30,32,46,48,56-74], the existing Raman databases corresponding to the oxidation products of the UO_2 matrix and other uranium-based nuclear fuels are quite scarce.

Even in the particular case of UO_2, which can be considered the simplest system among uranium-based oxide fuels, some of its oxidation products have not yet been properly characterised by Raman spectroscopy. For example, the hyperstoichiometric UO_{2+x} oxides have not been quantitatively analysed as a function of the oxidation degree, and the Raman spectrum corresponding to the U_3O_7 phase has never been reported. In addition, a deep study on all the vibrational modes featured in the Raman spectrum of UO_2, such as on their temperature dependence, has not been carried out. The typical Raman spectrum of UO_2 and that of its identified oxidation products are reflected in Figure 1.12.

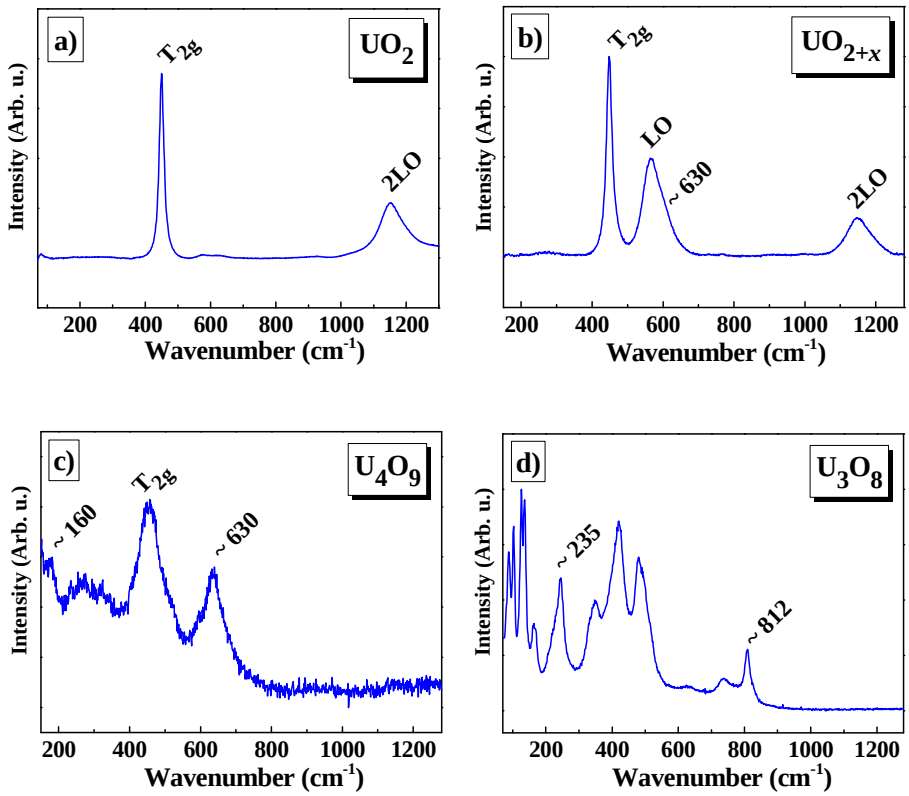

Fig. 1.12. Typical Raman spectrum of a) UO_2, b) UO_{2+x}, c) U_4O_9 and d) U_3O_8. The main characteristic Raman bands of each oxide have been marked.

The high sensitivity of Raman spectroscopy for differentiating between chemically similar compounds [30,32,57] as well as for detecting various structural defects –like those due to irradiation [61,63] or doping [64,68,69,72]– and, especially, its fulfilment of the safety requirements necessary for handling nuclear materials, make this technique a point of reference. To this effect, among the wide variety of advantages it offers, the following can be highlighted: 1) it does not require any special preparation of the sample, 2) it allows the analysis of a very small amount of sample, 3) it requires no direct contact between the experimental set-up and the analyte, 4) it can be easily implemented (remote analysis, Raman probes, handheld systems, etc.) for different applications, and 5) it is a non-destructive technique, as far as the excitation laser power density is controlled.

Moreover, the latest advances in the use of fibre optics [48,62] and the enhancement of local confinement techniques for highly radioactive samples (Figure 1.13) [67], both with the aim of avoiding nuclearisation of the Raman equipment partially or totally, are fostering new studies focused on hazardous compounds nearly unexplored so far.

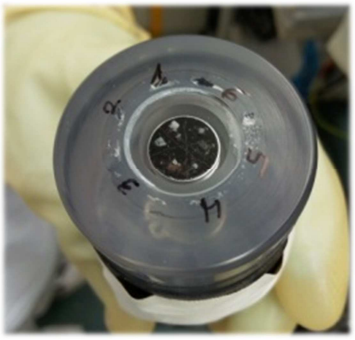

Fig. 1.13. α-shielding Plexiglas capsule developed at JRC-Karlsruhe [67] for the measurement of radioactive samples.

All in all, given the relevant information that Raman spectroscopy can provide (see Part 2 for further information), the employment of this technique needs to be considered if a deeper comprehension of the air oxidation process experienced by actual and potential SNF dioxide matrices is to be achieved. In this sense, Raman databases regarding the corresponding oxidation products of the latter processes must be further developed (characterising them in detail) and, in parallel, new methods enhancing the functionality and applicability of the Raman technique to radioactive materials must be pursued.

1.5. Objectives of this thesis

The importance of further understanding the oxidation process of the spent nuclear fuel matrix under dry storage conditions has been highlighted, as well as the assets that Raman spectroscopy can provide in this field. Hence, the main aim of this thesis entails the application of the Raman technique to the analysis of the SNF matrix oxidation in air, taking into account various factors (like temperature and the presence of transuranic elements) that may affect the reaction.

In particular, after the recent introduction to the key concepts of the subject in question and the methodology hereafter described (Part 2), the following general objectives are addressed throughout this work. They have been organised in different sets of chapters to give the necessary consistency:

- Attainment of a deeper insight into UO_2 and its oxidation process on the basis of Raman spectroscopy. It involves the commissioning of the Raman technique for a better characterisation of the UO_2 SNF matrix and its higher oxidation-state oxides, thus developing advances and/or improvements in this regard (Part 3: Results 1-4).

- Assessing the influence of the presence of transuranic elements on the SNF dioxide matrix oxidation. This consists in the application of the previously developed Raman methodology to the analysis of more complex and realistic systems, such as the air oxidation of uranium-based mixed dioxides (Part 3: Result 5 and Result 6).

Finally, the overall conclusions drawn from all the findings exposed along these six chapters –each of which corresponds to a scientific article, as listed in Section 1.6– are compiled in Part 4.

1.6. List of publications

The different scientific articles that have been comprised in this thesis are hereunder detailed, merely adapted in format. They correspond, in order of appearance, to Results 1-6 of Part 3:

- J. M. Elorrieta, L. J. Bonales, N. Rodríguez-Villagra, V. G. Baonza and J. Cobos, “A detailed Raman and X-ray study of UO_{2+x} oxides and related

structure transitions", *Phys. Chem. Chem. Phys.*, **18**, 28209-28216 (2016). DOI: 10.1039/c6cp03800j.

- J. M. Elorrieta, L. J. Bonales, N. Rodríguez-Villagra, V. G. Baonza and J. Cobos, "Spent fuel matrix oxidation studies under dry storage conditions", *MRS Advances*, **2 (12)**, 675-680 (2017). DOI: 10.1557/adv.2017.3.

- J. M. Elorrieta, L. J. Bonales, M. Naji, D. Manara, V. G. Baonza and J. Cobos, "Laser-induced oxidation of UO_2: A Raman study", *J. Raman Spectrosc.*, 1-7 (2018). DOI: 10.1002/jrs.5347.

- J. M. Elorrieta, L. J. Bonales, V. G. Baonza and J. Cobos, "Temperature dependence of the Raman spectrum of UO_2", *J. Nucl. Mater.*, **503**, 191-194 (2018). DOI:10.1016/j.jnucmat.2018.03.015.

- J. M. Elorrieta, D. Manara, L. J. Bonales, J. F. Vigier, O. Dieste, M. Naji, R. C. Belin, V. G. Baonza, R. J. M. Konings and J. Cobos, "Raman study of the oxidation in (U, Pu)O_2 as a function of Pu content", *J. Nucl. Mater.*, **495**, 484-491 (2017). DOI: 10.1016/j.jnucmat.2017.08.043.

- J. M. Elorrieta, L. J. Bonales, S. Fernández, N. Rodríguez-Villagra, L. Gutiérrez-Nebot, V. G. Baonza and J. Cobos, "Pre- and post-oxidation Raman analysis of (U, Ce)O_2 oxides", *J. Nucl. Mater.* (2018). (Submitted).

Other related publications, issued during the development of this thesis, are:

- L. J. Bonales, J. M. Elorrieta, C. Menor-Salvan and J. Cobos, "The behavior of unirradiated UO_2 and uraninite under repository conditions characterized by Raman", *MRS Advances*, **1 (62)**, 4157-4162 (2016). DOI: 10.1557/adv.2017.203.

- L. J. Bonales, J. M. Elorrieta, A. Lobato and J. Cobos, "Raman Spectroscopy, a Useful Tool to Study Nuclear Materials", *Applications of Molecular Spectroscopy to Current Research in the Chemical and Biological Sciences*, Dr. Mark Stauffer (Ed.), InTech (2016). ISBN 978-953-51-2681-2. DOI: 10.5772/64436.

- D. Manara, M. Naji, S. Mastromarino, J. M. Elorrieta, N. Magnani, L. Martel and J. -Y. Colle, "The Raman fingerprint of plutonium dioxide: Some example applications for the detection of PuO_2 in host matrices", *J. Nucl. Mater.*, **499**, 268-271 (2018). DOI: 10.1016 /j.jnucmat.2017.11.042.

1.7. References

[1] MITYC, *Sixth General Radioactive Waste Plan*, Ministry of Industry, Tourism and Trade, Madrid (2006).
[2] J. Astudillo, *El almacenamiento geológico profundo de los residuos radiactivos de alta actividad. Principios básicos y tecnología*. ENRESA, S.A. (2001).
[3] S. Gordelier, C. Nordborg and C. Pescatore, *NEA News*, **24 (1)**, 7-10 (2006).
[4] CEA, *Nuclear Fuels*, CEA Saclay and Groupe Moniteur (Éditions du Moniteur), Paris (2009). ISBN 978-2-281-11345-7.
[5] International Atomic Energy Agency, *Radioactive Waste Management Objectives*, IAEA Nuclear Energy Series No. NW-O, IAEA, Vienna (2011).
[6] IAEA. International Atomic Energy Agency. https://www.iaea.org
[7] International Atomic Energy Agency, *Spent Fuel Performance Assessment and Research*, IAEA-TECDOC-1771, IAEA, Vienna (2015).
[8] International Atomic Energy Agency, *Status of Accelerator Driven Systems Research and Technology Development*, IAEA-TECDOC-1766, IAEA, Vienna (2015).
[9] International Atomic Energy Agency, *Geological Disposal Facilities for Radioactive Waste*, IAEA Safety Standards Series No. SSG-14, IAEA, Vienna (2011).
[10] *POSIVA Annual Report 2016*, POSIVA, Helsinki (2017).
[11] UNESA. *Spanish nuclear power plants in 2016*. Directorate of Nuclear Energy, Madrid (2017).
[12] CSN. Spanish Nuclear Safety Council.
https://www.csn.es/en/centrales-nucleares-de-espana
[13] MINETAD. Ministry of Energy, Tourism and the Digital Agenda.
http://www.minetad.gob.es/en-US/
[14] *Nuclear Energy Encyclopedia: Science, Technology, and Applications*. John Wiley & Sons, Inc. (2011).
[15] OECD/NEA. *Management of Recyclable Fissile and Fertile Materials*, NEA #6107, Paris (2007).
[16] ENRESA. *Centralised Interim Storage Facility*.
http://www.enresa.es/eng/index/activities-and-projects/cts
[17] R. J. McEachern and P. Taylor, *J. Nucl. Mater.*, **254**, 87-121 (1998).
[18] P. Taylor, D. D. Wood, A. M. Duclos and D. G. Owen, *J. Nucl. Mater.*, **168**, 70 (1989).

[19] M. V. Glazoff, I. J. van Rooyen, B. D. Coryell and C. J. Parga, *Comparison of Nuclear Fuels for TREAT: UO_2 vs U_3O_8*, INL/EXT-16-37972 (2016).
[20] D. G. Boase and T. T. Vandergraaf, *Nucl. Technol.*, **32**, 60 (1977).
[21] G. Rousseau, L. Desgranges, F. Charlot, N. Millot, J. C. Niepce, M. Pijolat, F. Valdivieso, G. Baldinozzi and J. F. Berar, *J. Nucl. Mater.*, **355**, 10-20 (2006).
[22] A. Poulesquen, L. Desgranges and C. Ferry, *J. Nucl. Mater.*, **362**, 402-410 (2007).
[23] F. Grønvold, *J. Inorg. Nucl. Chem.*, **1,** 357-370 (1955).
[24] B. T. M. Willis, *Nature*, **197**, 755 (1963).
[25] L. Lynds, W. A. Young, J. S. Mohl and G. G. Libowitz, *Adv. Chem.*, **39**, 58-65 (1962).
[26] T. Ishii, K. Naito and K. Oshima, *Solid State Commun.*, **8**, 677-683 (1970).
[27] T. Matsui and K. Naito, *J. Nucl. Mater.*, **56**, 327-335 (1975).
[28] V. A. Alekseyev, L. A. Anan'yeva and R. P. Rafal'skiy, *Int. Geol. Rev.*, **23**, 1229-1236 (1981).
[29] D. J. M. Bevan, I. E. Grey and B. T. M. Willis, *J. Solid State Chem.* **61**, 1–7 (1986).
[30] H. He and D. Shoesmith, *Phys. Chem. Chem. Phys.*, **12**, 8108-8117 (2010).
[31] B. T. M. Willis, *Acta Cryst.*, **A34**, 88-90 (1978).
[32] L. Desgranges, G. Baldinozzi, P. Simon, G. Guimbretière and A. Canizares, *J. Raman Spectrosc.*, **43**, 455-458 (2012).
[33] P. Jolibois, *C. R. Acad. Sci.*, **224**, 1395-1396 (1947).
[34] B. D. Hanson. *The Burnup Dependence of Light Water Reactor Spent Fuel Oxidation*. Pacific Northwest National Laboratory, U.S. Department of Energy, PNNL-11929 (1998).
[35] T. Smith. Canoga Park, Calif.: Atomics International (1960).
[36] L. E. Thomas, R. E. Einziger and H. C. Buchanan, *J. Nucl. Mater.*, **201**, 310-319 (1993).
[37] G. -S. You, K. -S. Kim, D. -K. Min and S. -G. Ro, *J. Nucl. Mater.*, **277**, 325-332 (2000).
[38] L. E. Thomas, J. M. McCarthy and E. R. Gilbert, *Proc. 3rd Int. Spent Fuel Storage/Technology Symp./Workshop, CONF-860417*, Seattle, WA, 40 (1986).
[39] R. E. Einziger, L. B. Thomas, H. C. Buchanan and R. B. Stout, *J. Nucl. Mater.*, **190**, 53 (1992).
[40] J. -W. Choi, R. J. McEachern, P. Taylor and D. D. Wood, *J. Nucl. Mater.*, **230**, 250-258 (1996).
[41] K. H. Kang, S. H. Na, K. C. Song, S. H. Lee and S. W. Kim, *Thermochim. Acta*, **455**, 129-133 (2007).

[42] J. Cobos, D. Papaioannou, J. Spino and M. Coquerelle, *J. Alloys Compd.*, **271**, 610-615 (1998).
[43] D. A. Andersson, J. Lezama, B. P. Uberuaga, C. Deo, S. D. Conradson, *Phys. Rev. B*, **79**, 024110-1 (2009).
[44] V. J. Tennery and T. G. Godfrey, *J. Am. Ceram. Soc.*, **56**, 129-133 (1973).
[45] N. C. Jayadevan, R. G. Hadap and D. M. Chackraburtty, *J. Nucl. Mater.*, **82**, 195-198 (1979).
[46] C. Jégou, R. Caraballo, S. Peuget, D. Roudil, L. Desgranges and M. Magnin, *J. Nucl. Mater.*, **405**, 235-243 (2010).
[47] M. Strach, R. C. Belin, J. -C. Richaud and J. Rogez, *Inorg. Chem.*, **53**, 12757-12766 (2014).
[48] C. Jégou, M. Gennisson, S. Peuget, L. Desgranges, G. Guimbretière, M. Magnin, Z. Talip and P. Simon, *J. Nucl. Mater.*, **458**, 343-349 (2015).
[49] T. Tsuji, M. Iwashita, T. Yamashita and K. Ohuchi, *J. Alloys Compd.*, **271-273**, 391-394 (1998).
[50] P. Martin, S. Grandjean, C. Valot, G. Carlot, M. Ripert, P. Blanc and C. Hennig, *J. Alloys Compd.*, **444-445**, 410-414 (2007).
[51] R. C. Belin, M. Strach, T. Truphémus, C. Guéneau, J. -C. Richaud and J. Rogez, *J. Nucl. Mater.*, **465**, 407-417 (2015).
[52] R. Vauchy, A.-C. Robisson, R. C. Belin, P. M. Martin, A. C. Scheinost, F. Hodaj, *J. Nucl. Mater.*, **465**, 349-357 (2015).
[53] J. F. Vigier, P. M. Martin, L. Martel, D. Prieur, A. C. Scheinost and J. Somers, *Inorg. Chem.*, **54 (11)**, 5358-5365 (2015).
[54] M. Strach, R. C. Belin, J. -C. Richaud and J. Rogez, *J. Phys. Chem.C*, **119 (40)**, 23159-23167 (2015).
[55] T. Truphémus, R. C. Belin, J. -C. Richaud, M. Reynaud, M. -A. Martínez, I. Félines, A. Arredondo, A. Miard, T. Dubois, F. Adenot and J. Rogez, *J. Nucl. Mater.*, **432**, 378-387 (2013).
[56] M. L. Palacios and S. H. Taylor, *Appl. Spectrosc.*, **54**, 1372-1378 (2000).
[57] D. Manara and B. Renker, *J. Nucl. Mater.*, **321**, 233-237 (2003).
[58] T. Livneh and E. Sterer, *Phys. Rev. B*, **73**, 085118-085119 (2006).
[59] E. A. Stefaniak, A. Alsecz, I. E. Sajó, A. Worobiec, Z. Máthé, S. Török and R. Van Grieken, *J. Nucl. Mater.*, **381**, 278-283 (2008).
[60] F. Pointurier and O. Marie, *Spectrochim. Acta B*, **65**, 797-804 (2010).
[61] G. Guimbretière, L. Desgranges, A. Canizares, G. Carlot, R. Caraballo, C. Jégou, F. Duval, N. Raimboux, M. R. Ammar and P. Simon, *Appl. Phys. Lett.*, **100**, 251914 (2012).

[62] M. J. Sarsfield, R. J. Taylor, C. Puxley and H. M. Steele, *J. Nucl. Mater.*, **427**, 333-342 (2012).
[63] L. Desgranges, G. Guimbretière, P. Simon, C. Jégou and R. Caraballo, *Nucl. Instrum. Methods Phys. Res. Sect. B*, **315**, 169-172 (2013).
[64] R. Böhler, M. J. Welland, D. Prieur, P. Cakir, T. Vitova, T. Pruessmann, I. Pidchenko, C. Hennig, C. Guéneau, R. J. M. Konings and D. Manara, *J. Nucl. Mater.*, **448**, 330-339 (2014).
[65] D. Ho Mer Lin, D. Manara, P. Lindqvist-Reis and T. Fanghänel, *Vib. Spectrosc.*, **73**, 102-110 (2014).
[66] D. Horlait, R. Caraballo, F. Lebreton, C. Jégou, P. Roussel and T. Delahaye, *J. Solid State Chem.*, **217**, 159-168 (2014).
[67] M. Naji, J.-Y. Colle, O. Benes, M. Sierig, J. Rautio, P. Lajarge and D. Manara, *J. Raman Spectrosc.*, **46**, 750-756 (2015).
[68] F. Lebreton, D. Horlait, R. Caraballo, P. M. Martin, A. C. Scheinost, A. Rossberg, C. Jégou and T. Delahaye, *Inorg. Chem.*, **54 (20)**, 9749-9760 (2015).
[69] M. Chollet, D. Prieur, R. Böhler, R. Belin and D. Manara, *J. Chem. Thermodyn.*, **89**, 27-34 (2015).
[70] G. Guimbretière, A. Canizares, N. Raimboux, J. Joseph, P. Desgardin, L. Desgranges, C. Jégou and P. Simon, *J. Raman Spectrosc.*, **46 (4)**, 418-420 (2015).
[71] G. Guimbretière, A. Canizares, L. Desgranges, R. Caraballo, F. Duval, C. Jégou, M. Magnin and P. Simon, *J. Nucl. Mater.*, **478**, 172-175 (2016).
[72] Z. Talip, S. Peuget, M. Magnin, L. Berardo, C. Valot, R. Vauchy and C. Jégou, *J. Raman Spectrosc.*, **48 (5)**, 765-772 (2017).
[73] M. Naji, N. Magnani, L. J. Bonales, S. Mastromarino, J.-Y. Colle, J. Cobos and D. Manara, *Phys. Rev. B*, **95**, 104307 (2017).
[74] Z. Talip, S. Peuget, M. Magnin, M. Tribet, C. Valot, R. Vauchy and C. Jégou, *J. Nucl. Mater.*, **499**, 88-97 (2018).

Part 2

Methodology

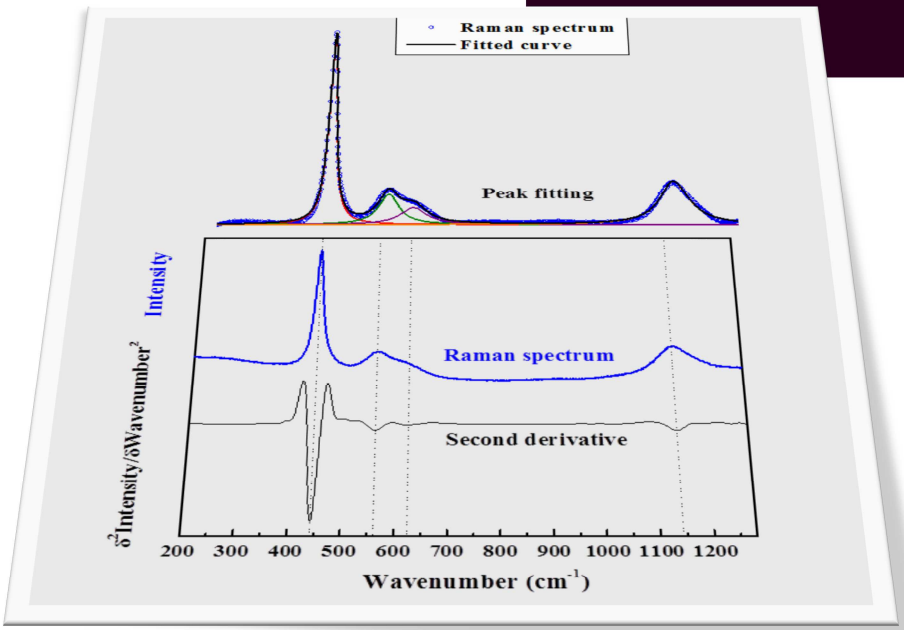

Various characterisation techniques can be currently employed for the analysis of uranium-based dioxide fuels and their oxidation products, presumably being XRD the most common. Anyhow, Raman spectroscopy might provide valuable help to the study of the latter systems. Owing to its high sensitivity, slight changes or structural defects occasionally undetectable by other techniques can be conversely observed by Raman spectroscopy.

A detailed analysis of the acquired Raman spectrum supplies relevant information on chemical composition and structural properties. Indeed, the application of such an analysis has allowed us to track the evolution of defects associated with oxygen incorporation during oxidation, vacancies or with cations substitution (doping), as will be shown throughout this thesis.

The present part is focused on the methodology applied for the accomplishment of the Raman studies compiled in Part 3. In this sense, the general structure followed is first exposed and, thereafter, the fundamentals of Raman spectroscopy, the equipment used, the samples preparation and the spectral analysis procedure are described in detail.

2.1. General structure of this thesis

All the studies gathered in the results part (Part 3) are mainly based on the application of the Raman spectroscopy technique to UO_2, although assessing different affecting/complicating factors in each one. In this way, these Raman studies can be structured and defined as follows:

- Result 1. Analysis of the influence of oxygen incorporation into UO_2, obtaining an oxidation degree estimation method for the hyperstoichiometry range.
- Result 2. Application of the previous method for *in situ* tracking the early-stage oxidation of UO_2, considering the additional effect of temperature.
- Result 3. Development of a laser heating method for the purpose of *in situ* characterising the oxidation reaction of UO_2 and simultaneously estimating the temperature at which the different oxidation products are formed.

- Result 4. Evaluation of the temperature effect, under anoxic atmosphere, on the Raman spectrum of UO_2.
- Result 5. Analysis of the effect caused by Pu incorporation into UO_2, especially with regard to its influence on the mixed dioxide oxidation.
- Result 6. Analysis of the effect caused by Ce incorporation into UO_2, especially with regard to its influence on the mixed dioxide oxidation. Assessment of (U, Ce)O_2 as an appropriate surrogate for (U, Pu)O_2.

The latter results structure can be appreciated in the graphical scheme shown in Figure 2.1.

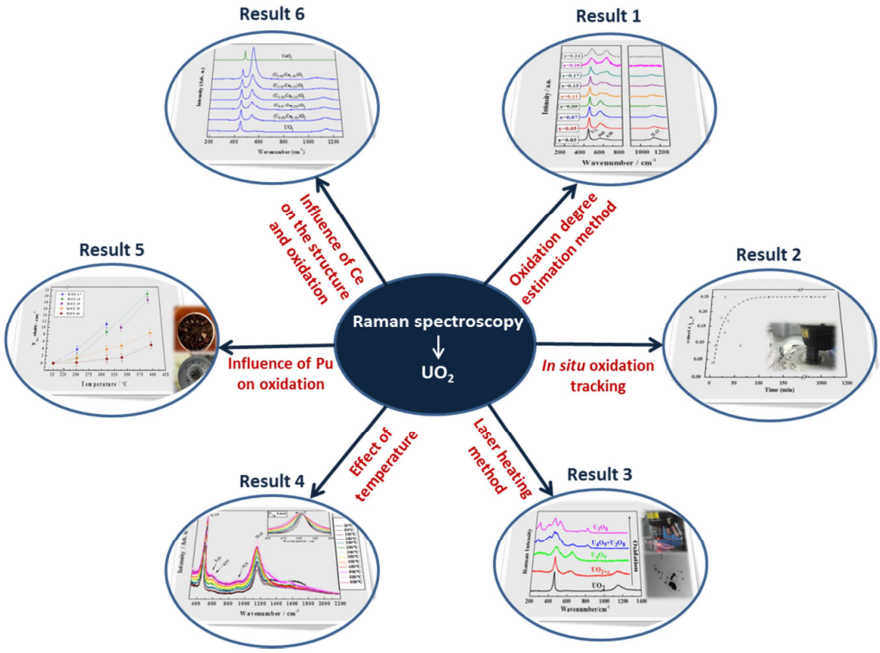

Fig. 2.1. Graphical scheme describing the results structure followed in this thesis.

Therefore, an introduction to Raman spectroscopy as well as a thorough description of the specific Raman methodology followed can be hereunder found. It is noteworthy that the characterisation techniques used in a complementary fashion to Raman spectroscopy, *i.e.* XRD, thermogravimetry analysis and scanning electron microscopy (SEM), are namely detailed in the corresponding chapters.

2.2. Introduction to Raman spectroscopy

The designation of Raman spectroscopy is due to C. V. Raman, who experimentally discovered this effect in 1928 when observing the scattering of light produced by molecules (although it had already been predicted by Smekal [1]). His rigorous and complete study [2] was recognised with the Nobel Prize in 1930. Anyway, it was not until the emergence of the laser in 1960 that it was possible to examine the Raman Effect more thoroughly.

2.2.1. Some fundamental notions

When impinging a monochromatic radiation, *i.e.* laser, on some substances and plotting the intensity of the scattered radiation vs. the difference between the incident and scattered radiation frequencies (ν_0-ν_s), a characteristic Raman spectrum of the particular substance is obtained. Indeed, practically the same spectrum is acquired for any frequency of the excitation source (ν_0), being the acquired frequencies (Raman lines positions) maintained [3]. By way of illustration, Figure 2.2 shows a comparison between the Raman spectrum of UO_2 acquired with a red laser and the one acquired with a green laser, where the two main characteristic Raman lines are observed at exactly the same position, although their relative intensities have notably changed.

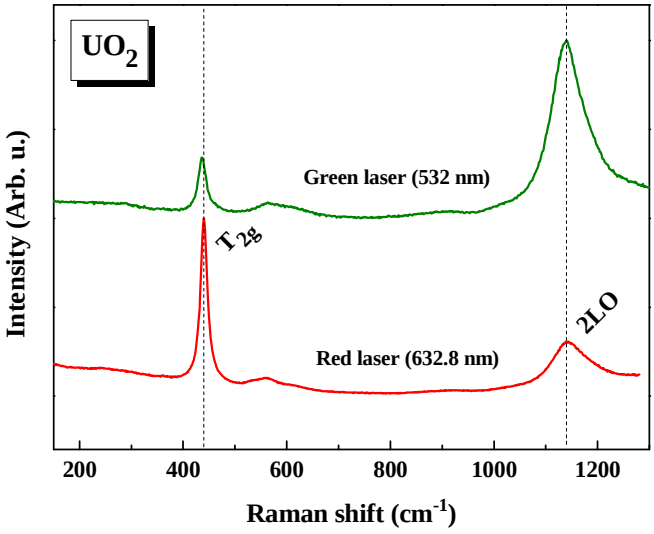

Fig. 2.2. Raman spectrum of UO_2 acquired with different excitation frequencies.

In the Raman Effect the scattered photons appear almost instantly after the radiation incidence (~10^{-15} s), unlike an elastic absorption process where the response is slower (10^{-9}-10^{-12} s) [4]. In this way, it is considered an inelastic scattering process between the incident light and matter.

In order to induce the Raman phenomenon, the employed incident frequency needs to be low enough –usually in the ultraviolet-visible (UV-visible) region– not to produce an electronic transition. Thus, in this case, the frequencies (ν_0-ν_s) of the Raman lines obtained correspond to the spacing between vibrational or rotational energy levels [4]. In essence, the incident photon of energy $\hbar\nu_0$ interacts with a molecule and produces one of those transitions, what entails an energy transfer of $\hbar(\nu_0$-$\nu_s)$. The scattered photon then emerges with an energy $\hbar\nu_s$, which is shifted with respect to the incident energy in a quantity equal to the energy lost or gained by the molecule. The intermediate higher-energy state reached in the latter process is virtual [3], meaning that it does not correspond to one of the characteristic energy states of the molecule as in the case of absorption phenomena.

The Raman Effect can be similarly described either in the context of quantum [5] or classical [6] mechanics, simplifying the system to the case of a diatomic molecule that vibrates as a result of its interaction with the incident light (Figure 2.3).

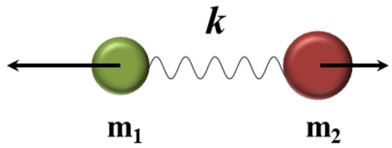

Fig. 2.3. Simplified model of a diatomic molecule (adapted from [7]).

In fact, since in both interpretations the harmonic oscillator approximation is taken into account, the vibration frequency (ν) of the molecule can be basically defined in terms of its bond strength (k) and reduced mass (μ) [4]:

$$\nu = \frac{1}{2\pi}\sqrt{\frac{k}{\mu}} \qquad \text{(Eq. 2.1)}$$

being

$$\mu = \frac{m_1 m_2}{m_1 + m_2} \qquad \text{(Eq. 2.2)}$$

where m_1 and m_2 are the masses of the atoms that compose the molecule.

As for the vibrational virtual states reached by the molecule in the Raman process, the quantum description accordingly relates them to the energy levels (E_n) of a one-dimensional harmonic oscillator [4],

$$E_n = \left(n + \frac{1}{2}\right) h\nu \qquad n = 0,1,2\ldots \qquad \text{(Eq. 2.3)}$$

Where n is the vibrational quantum number, h is Planck's constant and ν represents the frequency of vibrational quanta called phonons, which are responsible for inelastically scattering the incident photon [8].

Considering a classical interpretation, such virtual states would be created as a consequence of the polarisation (or change in polarisability) induced by the interaction between the electric field of the incident light and the electron cloud of the molecule [8].

If a polyatomic molecule of N atoms is reckoned, the corresponding normal modes of vibration are 3N-6, exceptionally being 3N-5 in the case of a linear one. These normal modes represent the vibrations that simultaneously take place in different parts (chemical bonds) of the molecule. In order to qualitatively determine the normal modes induced in a particular molecule, group theory needs to be applied, taking into account the molecular point group that defines its symmetries and consequent selection rules [9].

It hence becomes clear that a Raman spectrum contains essential information about vibration frequencies, which are specific of the studied substance since they are related to the molecular structure and its surroundings.

2.2.2. Contributions to the Raman spectrum

As Raman scattering is induced, three simultaneous processes actually take place, basically differing in the relation between the incident (ν_0) and scattered (ν_s) photon frequencies [8]. These processes, graphically represented in Figure 2.4 along with an infrared (IR) absorption process for the sake of comparison, are divided as follows:

- For $\nu_0 > \nu_s$: Raman Stokes transitions→ Set of frequencies corresponding to a transition where the molecule ends in a higher energy state than the initial one.

- For $\nu_0 < \nu_s$: Raman anti-Stokes transitions→ Set of frequencies corresponding to a transition where the molecule ends in a lower energy state than the initial one.
- For $\nu_0 = \nu_s$: Rayleigh elastic scattering→ Frequency corresponding to that of the incident light (the excitation frequency).

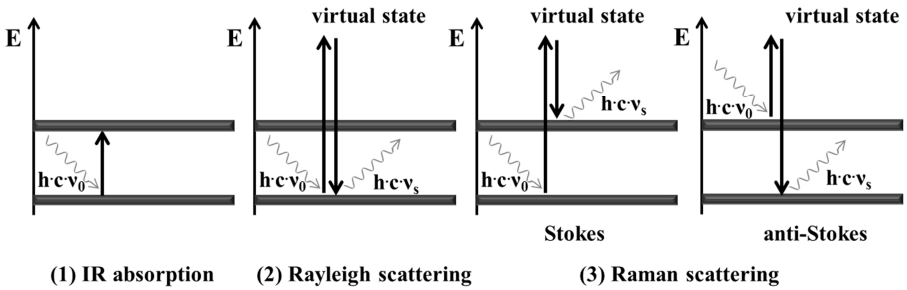

Fig. 2.4. Energy level diagrams describing the physical phenomenon of (1) IR absorption, (2) Rayleigh scattering, and (3) Raman scattering (adapted from [7]).

Even though it is not a Raman transition, Rayleigh scattering is unavoidable when performing Raman spectroscopy. This radiation constitutes the major part of the scattered beam intensity, making it difficult to isolate the much weaker Raman-scattered light. As a matter of fact, in the latter case the incident/emergent intensities ratio is only of the order of 10^{-5}-10^{-8} [8], what requires an intense excitation radiation as well as the correct removal of the Rayleigh Effect contribution. In this sense, different elements or configurations are used in conventional Raman spectrometers (see Section 2.3.1) to avoid the Rayleigh straight-scattered light, *e. g.* notch filters (which are high-pass filters that only remove a frequency range close to the excitation frequency) or edge filters (which remove the latter range and all frequencies below, not allowing to acquire the anti-Stokes Raman lines).

As for the Stokes and anti-Stokes lines, these are analogous in the Raman spectrum (being like a reflection of each other with regard to their positions), while their intensities differ notably. This occurs because the intensity of a given Raman line is closely related to the population of those levels involved in its corresponding Raman transition [4]. In this respect, the intensities of the anti-Stokes lines are always lower due to their lower transition probability –their related levels are less populated– [8]. Such difference in intensities can be clearly appreciated in Figure 2.5, where both the Stokes and anti-Stokes contributions of the Raman spectrum of UO_2 are shown.

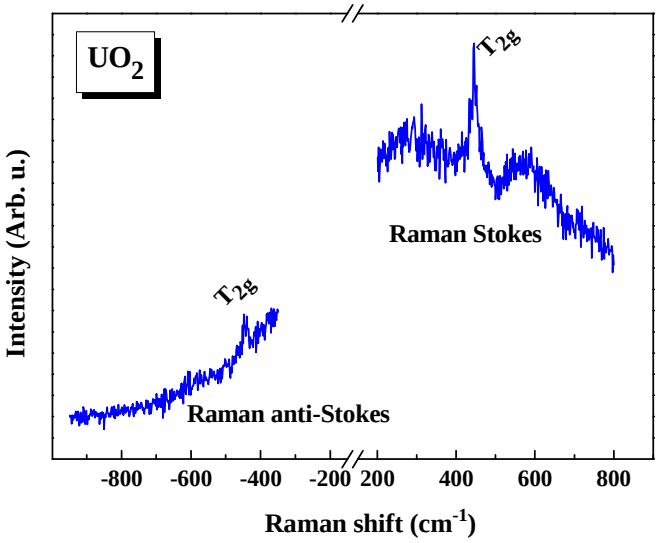

Fig. 2.5. Raman spectrum of UO_2, where both Stokes and anti-Stokes lines have been acquired.

The relation between the intensities of equivalent Stokes and anti-Stokes lines is thus dependent on the population of the molecule states and, consequently, taking into account the Boltzmann distribution, on temperature as follows [10]:

$$\frac{I_{anti-Stokes}}{I_{Stokes}} = \left(\frac{\omega_0+\omega_j}{\omega_0-\omega_j}\right)^4 e^{-\frac{hc\omega_j}{k_B T}} \qquad \text{(Eq. 2.4)}$$

where ω_0 is the wavenumber of the excitation line, ω_j are the wavenumbers of the different Raman lines, $I_{anti\text{-}Stokes}$ and I_{Stokes} are the intensities of the anti-Stokes and Stokes lines, k_B is the Boltzmann constant, c is the speed of light, h is Planck's constant and T is temperature.

It should be noted that, as in the latter expression, Raman frequency shifts are typically expressed in wavenumber units (cm^{-1}). This comes from the following conversion:

$$\Delta\omega = \frac{1}{\lambda_0} - \frac{1}{\lambda_s} \qquad \text{(Eq. 2.5)}$$

where $\Delta\omega$ corresponds to the Raman shift expressed in wavenumber, λ_0 is the excitation wavelength and λ_s are the different wavelengths measured by the spectrometer.

Taking advantage of the statistical relation of Equation 2.4, the system temperature can be roughly estimated (as reflected in Result 3 of Part 3). Anyhow, as both Stokes and anti-Stokes lines provide the same information, if the temperature estimation is not required it is common to measure the Stokes lines only, whose probability is higher and thus a better spectrum can be acquired.

Occasionally, electronic excitation may be induced together with vibrational excitation when working in the UV-visible region, being originated from a so-called vibronic transition (electronic and vibrational transitions coupling due to resonance Raman scattering) [8]. Thus, in these cases electronic contributions may also be detected in the Raman spectrum (an example of this feature can be seen in Figure 3.4.4a of Result 4).

If we go back to Equation 2.1, it is easy to notice that vibrations of light atoms will present high frequencies, whereas those of heavy atoms will conversely present low frequencies. Thereby, Raman shifts (hereafter indistinctly referred to as wavenumbers) may be mainly found in the range covering from approximately 10 to 4000 cm^{-1} [4], evidently depending on the type of substance analysed.

2.2.3. Temperature influence and anharmonicity

So far, we have been discussing about single molecules but, in order to take a more realistic approach, it becomes necessary to consider the studied sample as a set of molecules that interact with each other. Indeed, given that all samples used in the present work are crystalline solids, we will hereon conceive our system as a crystal lattice where atoms are found sequentially ordered. In this case, lattice vibrations induced by Raman scattering can likewise be associated with phonons [8].

The marked effects produced in the Raman spectrum of a crystal when this is subjected to heating are strongly related to anharmonicity [11], indicating that the atoms actually behave like anharmonic oscillators within the lattice. Those variations of thermal origin are, as a function of temperature, a change in the frequency shifts as well as a change in the width and integrated intensity of the Raman lines [12]. It should be noted that each line in the spectrum is influenced in a different manner, since it corresponds to a particular normal mode. By way of example, the effect of temperature on the Raman spectrum of UO_2 is shown in Figure 2.6, where a downshift, a slight broadening and a decrease in intensity can be observed for the two main characteristic Raman lines as a function of

increasing temperature. For this reason, the evolution of the frequency shifts and linewidths with temperature is commonly used as a source of information on the anharmonic interactions taking place within the lattice (lines intensities are not used since they are highly influenced by extrinsic factors).

It is well-known that, when temperature increases, crystals experience lattice expansion. This obviously implies an increase in the lattice parameters, what is an evidence of anharmonicity and would arise from the impact of temperature on the population of the energy levels of each normal mode [13]. A lattice parameter growth consists basically in an increase in the inter-atomic distances and a subsequent weakening of the bonding forces [14]. Such a weakening thus contributes to a lowering of the vibrational frequencies (see Equation 2.1). However, the variation with temperature of the frequency shifts corresponding to the different normal modes does not only depend on thermal expansion, but also on the originated anharmonic phonon interactions, where non-equilibrium phonons decay into lower-energy phonons or their frequencies change due to the scattering they suffer by means of thermal phonons [13].

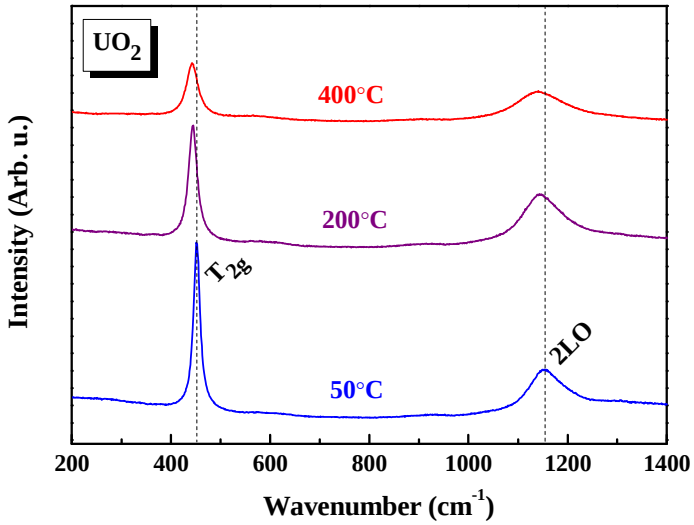

Fig. 2.6. Raman spectrum of UO_2 acquired at different temperatures under inert atmosphere.

On the other hand, despite the theoretical sharp shape that Raman lines should feature –representing a specific mode frequency–, an intrinsic width is experimentally observed, being these lines in consequence generally called bands.

The factors that contribute to this actual width may be divided as follows: 1) factors which are independent of temperature, such as the finite resolution of the spectrometer [15], impurities and defects provoking elastic scattering processes [16], or natural isotopic dispersion [16], and 2) the anharmonic decay of phonons [17], which is a temperature-dependent process. Hence, since the lattice anharmonicity that generates expansion only affects the frequency shifts, the change in linewidth with temperature would exclusively reflect the anharmonic phonon damping caused by decay to lower-energy phonons [17], accordingly resulting in line broadening.

All in all, Raman spectroscopy is capable of identifying different expressions of anharmonicity, as we have just seen with regard to the influence of temperature on the Raman spectrum. The weak allowance of overtones is, for example, another evidence of anharmonicity. Overtones, which consist in multiples of a fundamental vibration (occurring when more than one quantum of energy corresponding to that vibration frequency reach the molecule), are forbidden in the harmonic approximation but can sometimes be detected in the Raman spectrum [18]. In fact, their frequency is a multiple of their corresponding fundamental frequency under any perturbation (a bit less due to anharmonicity) [18], thus presenting the same temperature evolution as the fundamental vibration (see Result 4).

2.3. Raman equipment

The instruments that have been required for the Raman spectroscopy measurements performed along this thesis are, in short, two different Raman spectrometers and a temperature controlled microscope stage. The reason for using an additional spectrometer to the one available at CIEMAT facilities lies in the necessity of special features or conditions that this could not fulfil: 1) the acquisition of the anti-Stokes Raman lines in order to estimate the system temperature (Result 3), since it employs an edge filter; and, most notably, 2) its adequate conditioning inside a radioactive facility to measure highly radioactive materials as plutonium-containing samples (Result 5). The Raman spectrometer available at JRC Karlsruhe facilities, in turn, met both circumstances.

2.3.1. Raman spectrometers

The fundamental components of Raman dispersive spectrometers, as those employed in this work, can be enlisted as follows [7]:

Excitation source: Traditionally, mercury arc lamps were used as light sources until being replaced by laser sources. Laser beams are highly monochromatic, present small diameter and, with the help of different optic devices, can be focused on small samples. In addition, in order to enhance the laser quality it is possible to employ a pass-band filter, designed to pass only a certain band of frequencies while attenuating all signals outside this band. This component is commonly known as interferometric filter.

Sample illumination system and collection optics: The collimation and focusing optics of the exciting radiation onto the sample depends on the experimental setup. In principle, excitation and collection from the sample can be accomplished in any geometry, although 90 and 180°C (backscattering) are more frequently employed. On the other hand, the use of fiber optics helps to make the spectrometers more versatile, although they remarkably reduce the incident light intensity.

Wavelength selectors and/or separators: The separation or removal of the intense Rayleigh scattering can be achieved by using two different types of filters: notch and edge filters. Notch filters allow the acquisition of the anti-Stokes and Stokes Raman spectra down to ~30 cm^{-1}, but their use is expensive since they must be replaced very frequently (~2 years). For this reason, the use of edge filters is widespread. These are wide pass-band filters, which imply that the anti-Stokes Raman spectrum cannot be obtained and typical minimum wavenumbers are ~50 cm^{-1}. After removal or suppression of the Rayleigh radiation, the separation of the different Raman radiations scattered by the sample should be performed. The first Raman spectrometers used prisms, but nowadays these are replaced by gratings that are typically holographically produced. It is worth noting that filters can be neglected if coupling of two or three monochromators is set in a series. This configuration allows not only to separate the Raman lines but also to remove the Rayleigh scatter.

Detectors: Just like in other spectrometers, the former detectors, that is, photographic films, were substituted first by photodiode array detectors and then by charge transfer devices (CTDs) such as charge-coupled devices (CCDs). CCDs are silicon-based semiconductors arranged as an array of photosensitive

elements, each one generating photoelectrons and storing them as an electrical charge. Charges are stored on each individual pixel as a function of the number of photons striking that pixel and then read by an analog-to-digital converter [6].

In the micro-Raman technique, as it is our case, a microscope is integrated in a conventional Raman spectrometer, enabling both visual and spectroscopic measurements. As can be seen in the schematic representation of Figure 2.7, in these types of equipment the focusing and collection optics of the scattered radiation are identical [7]. These spectrometers present several advantages, such as the possibility of performing an analysis of a single point or mapping and imaging measurements.

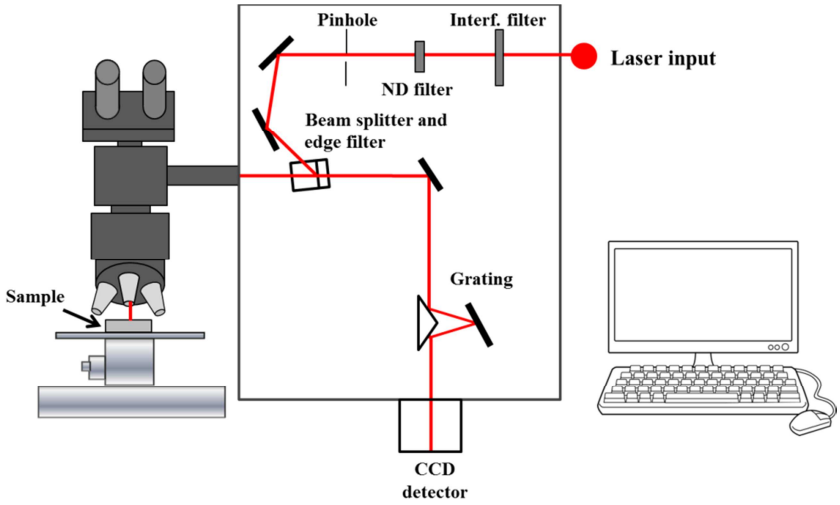

Fig. 2.7. Scheme of the main components of a micro-Raman spectrometer [7].

2.3.1.1. Raman spectrometer at CIEMAT

The major part of the studies that shape this thesis was carried out making use of the Raman spectrometer available at CIEMAT facilities: a Horiba LabRAM HR Evolution spectrometer (Jobin-Yvon Technology) (Figure 2.8). Therefore, a deeper description of the main features and configuration of this instrument becomes suitable.

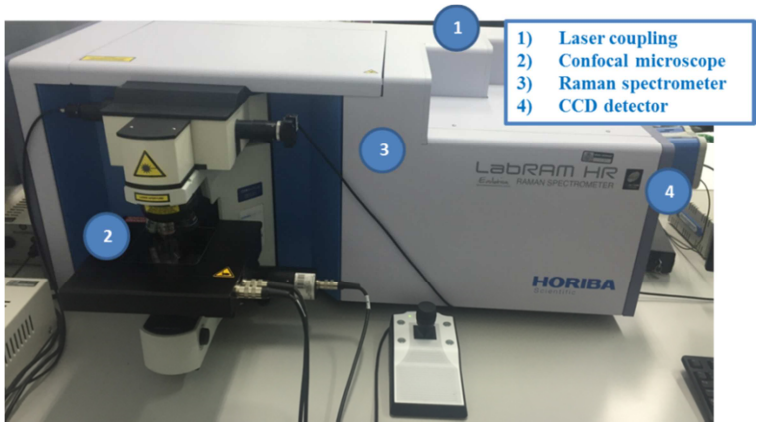

Fig. 2.8. General view of the Horiba LabRAM HR Evolution spectrometer.

Laser coupling: Different lasers can be coupled to the spectrometer optical system, although consequently adjusting the optical path to their specific features (see 1 in Fig. 2.8). It should be noted that all Raman spectra were acquired at an excitation wavelength of 632.8 nm (1.96 eV) provided by a He-Ne laser of 20mW nominal power.

Confocal microscope and sample platform: The laser beam can be focused on the sample through different objectives (5x, 20x, 50x and 100x) of a confocal microscope (see 2 in Fig. 2.8). This microscope holds a motorised precision platform where the sample to be measured is placed on, enabling its movement along the three spatial directions (X, Y, Z) with a 0.1 µm resolution. Orientation in the X-Y plane is used for the sample zone selection, whereas Z motion allows focusing. In this work the laser beam was commonly focused onto the sample through the 100x objective, except for those cases where the use of the long focal distance 50x objective was required, *e.g.* when surface irregularities were largely present in oxidised pellets or when the temperature controlled stage was employed.

Guidance optical system*:* For the sake of clarity, the main components located within the optical system of the spectrometer (see 3 in Fig. 2.8) are individually described along the successive lines, in the order followed by the optical path (see Fig. 2.9).

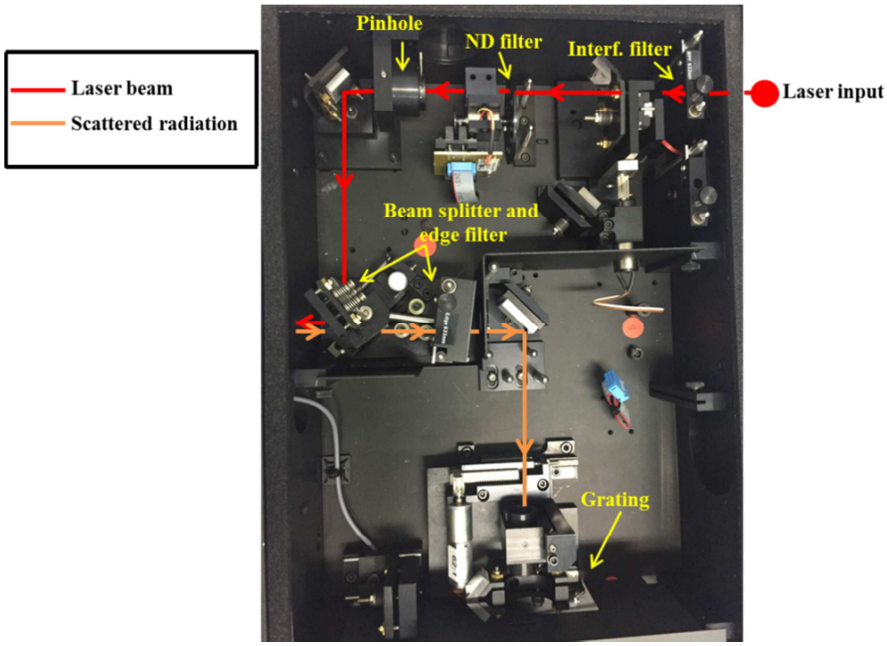

Fig. 2.9. Guidance optical system of the Horiba LabRAM HR Evolution spectrometer, where its main components have been labelled.

1) *Interferometric filter*: There is an interferometric line filter for each laser, since the adjacent wavelength lines to be removed are obviously not the same if the wavelengths of the monochromatic lasers employed are different. These filters are placed at the laser output and motorised in order to select one or another, depending on the required laser configuration.

2) *Neutral-density (ND) filter*: This set of filters allows us to attenuate in a controlled way the laser power reaching the sample.

3) *Beam splitter:* After crossing the ND filter, the laser beam is directed through a pinhole to the beam splitter. This component enables both leading the laser to the sample and thereafter collecting de scattered radiation that comes from the microscope in a ~180º configuration with respect to the excitation beam (pseudo-backscattering).

4) *Edge filter*: For the correct removal of the unwanted Rayleigh contribution, a characteristic edge filter is manually attached to the beam splitter according to the employed laser. In addition, when changing the

edge it is also necessary to modify the beam splitter-edge angle configuration with the help of a separator (see white point in Fig. 2.9). The edge filter used for the 632.8 nm (red) laser cuts the scattered radiation at <50 cm^{-1}.

Spectral analyser: Once the edge filter cuts the Rayleigh and Raman anti-Stokes contributions, the Raman Stokes radiation is directed to the diffraction grating (see Fig. 2.9), which divides the signal into its constituent parts (wavelength separation). A 600 grooves/mm holographic grating was used in all cases, providing a spatial resolution of ~1 cm^{-1}/ pixel and a spectral resolution of better than 3 cm^{-1}.

Detector: The wavelength-separated radiation is finally registered in a Peltier-cooled CCD of 1024 x 256 pixels (see 4 in Fig. 2.8).

In addition to the above mentioned components, different lenses and mirrors can be found throughout the whole optical path, whose function is to correctly direct the beam within the optical system. Due to the amount of components that the laser beam encounters along its way before reaching the sample, a consequent power reduction of around 50% takes place. Nevertheless, the power attained at the sample surface is still sufficient to properly carry out the experiments.

2.3.1.2. Raman spectrometer at JRC Karlsruhe

The Raman equipment available at JRC Karlsruhe facilities consisted in a Jobin-Yvon T64000 spectrometer (Figure 2.10).

The excitation source used in this case was the 647 nm (1.91 eV) line of a Kr^+ laser with a controllable nominal power up to 0.5 W. The laser was focused onto the sample using a 50x long focal objective, what was necessary due to the employment of the α-shielding capsules (see Section 2.4.2).

The spectrometer was used in the single spectrograph configuration when the temperature estimation was not required (Result 5), that is, as a conventional single-spectrometer based system employing an edge filter. However, in those experiments concerning temperature estimation (Result 3), the spectrometer was used in the triple stage operation mode (triple monochromator mode), which permitted access to both Stokes and anti-Stokes Raman spectrum lines while blocking the elastic Rayleigh line.

The backscattered radiation was dispersed, in both configurations, using an 1800 grooves/mm holographic grating and recorded by a low noise liquid nitrogen cooled Symphony CCD detector. The single spectrograph mode enabled a spectral resolution of ~1 cm^{-1}, whereas the one obtained in triple stage mode was better than 1 cm^{-1}.

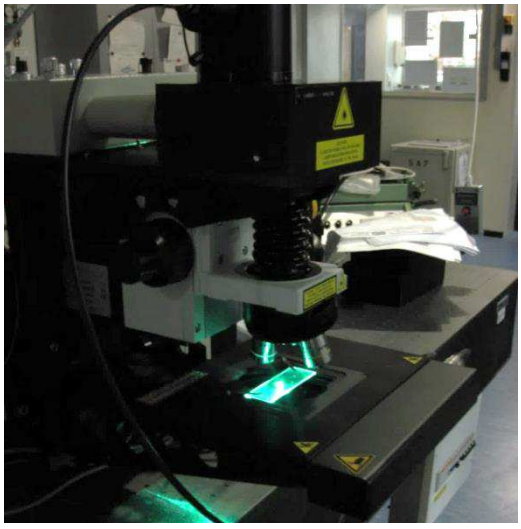

Fig. 2.10. Partial view of the Jobin-Yvon T64000 spectrometer (a general view cannot be shown due to JRC Karlsruhe security standards).

2.3.2. Temperature controlled stage

Temperature dependent micro-Raman spectroscopy experiments were carried out by means of a Linkam THMS600 temperature controlled stage (Figure 2.11), coupled to the BX41 Olympus microscope of the LabRAM HR Evolution spectrometer at CIEMAT facilities.

The atmosphere used while heating the samples depended on the kind of experiment required. In this way, a synthetic air flow was supplied throughout the oxidation processes (Result 2 and Result 6). Conversely, reducing (N_2+4.7%H_2) and inert (Ar) flows were applied to UO_2 and U_4O_9 samples, respectively, in those cases where the effect of temperature on their characteristic Raman spectra was examined (Result 2 and Result 4).

A heating ramp of 10°C/min was applied in all cases to reach the desired temperatures. Thereafter, a thermalisation time of 15 minutes was applied at each

selected temperature before acquiring the corresponding Raman spectra. The mechanical design and electronics of the Linkam stage provided precise control and a temperature stability better than 0.2 degrees over the whole temperature range.

Fig. 2.11. General view of the Linkam THMS600 stage, coupled to the microscope.

2.4. Samples preparation for Raman measurements

Owing to their hazardous nature, special care needs to be taken when handling radioactive materials such as the ones analysed in this work, containing either uranium or uranium-plutonium mixtures. The main advantage of micro-Raman spectroscopy in this regard (see Section 1.4) is the minor quantity of sample needed, especially when powdered samples are used, what largely facilitates the fulfilment of the safety conditions required for radiation protection.

In addition, since good quality Raman spectra can be acquired with no special sample preparation, the handling is basically reduced to the placement of each specimen on its corresponding holder. Nonetheless, while it seems a quite trivial procedure, the handling of radioactive samples requires to be carefully done, particularly when working with powdered samples due to their easiness to spread. Naturally, this procedure resulted much more complicated when it concerned uranium-plutonium mixed oxides at JRC Karlsruhe, given their greater hazard and their consequent confinement requisite.

The treatment performed (if applicable) on the different samples prior to their Raman characterisation is specifically detailed in each corresponding chapter.

2.4.1. Samples preparation at CIEMAT facilities

The preparation procedure for the Raman characterisation of samples at CIEMAT facilities simply consisted in placing the particular uranium-containing oxide, which in some cases was in the form of disk and in other cases as powder, on a common microscope sample holder (Figure 2.12a) or on the Linkam stage holder if temperature dependent experiments were carried out (Figure 2.12b).

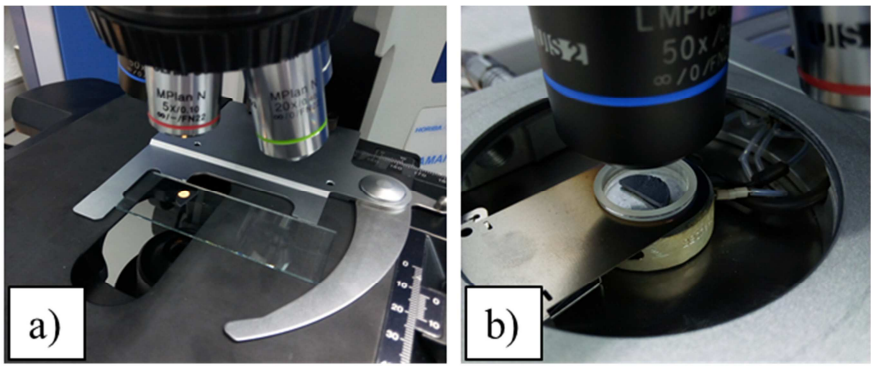

Fig. 2.12. a) Microscope sample holder containing a powdered uranium oxide and b) quartz holder of the Linkam temperature stage containing a UO_2 half disk.

Since the Raman spectrometer is not located inside a radioactive facility, it was necessary to previously ensure that all the samples were exempt, that is, below the radioactivity limits imposed for a conventional laboratory.

2.4.2. Samples preparation at JRC Karlsruhe facilities

In contrast, the Raman spectrometer available at JRC Karlsruhe is located inside a radioactive facility, making it possible to work with higher radioactivity levels. This gave us the opportunity to characterise uranium-plutonium and uranium-americium mixed oxides (the latter not included in this thesis), what otherwise would not have been feasible.

The UO_2 sample employed for the Raman laser heating experiments at JRC Karlsruhe (Result 3) was also placed on a conventional microscope sample holder. On the other hand, when it came to performing Raman spectroscopy measurements on uranium-plutonium mixed oxides (Result 5), which are highly radioactive, confinement of the sample was needed.

In this case, the confinement solution lied in the insertion of the uranium-plutonium oxides into α-shielding Plexiglas capsules recently designed and developed by JRC Karlsruhe [19]. Figure 2.13 shows different steps of this procedure. Some fragments of the various oxides were placed on the sample holder sticker (Figure 2.13a), inside a glove-box. Once all the pieces were properly stuck (Figure 2.13b), the sample holder was introduced in its capsule and carefully withdrawn from the glove-box (Figure 2.13c), sealing the lower plastic part of the capsule. Raman spectra were thus acquired through the top quartz window of these capsules (Figure 2.13d).

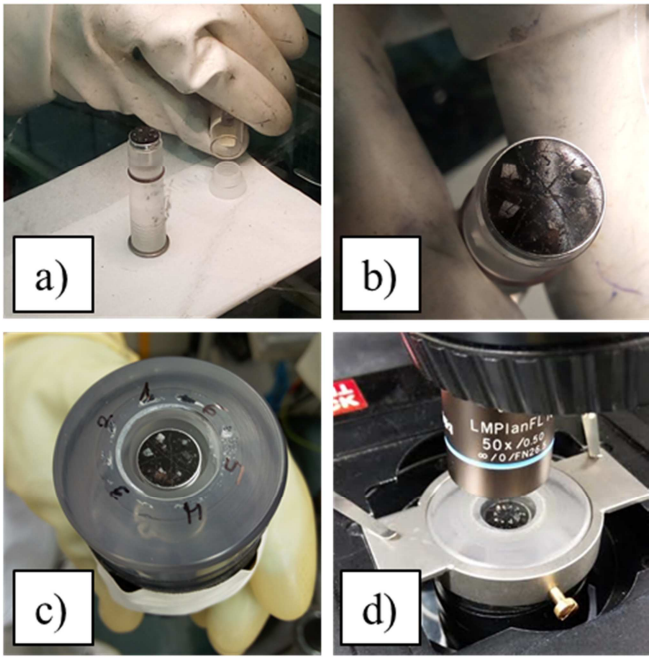

Fig. 2.13. From a) to d), different steps followed during the samples preparation for Raman measurements at JRC Karlsruhe facilities.

2.5. Raman spectra analysis

A reliable Raman analysis is based, firstly, on the proper acquisition of the Raman spectrum and, secondly, on its subsequent delicate processing. Both steps become very important if one intends to obtain as much information as possible from the Raman characterisation of a given sample.

2.5.1. Spectra acquisition and calibration

As already mentioned, the micro-Raman technique allows the user to subtract spectroscopic data from a particular area on the sample surface. In order to acquire a Raman spectrum, the previously prepared sample is placed under the microscope objective and the excitation laser is then focused onto the area of interest, whose size will be defined by the laser spot size. This process is by no means negligible, since a bad focusing leads to a reduction of the laser power density reaching the sample and, hence, to a diminution of the scattered light intensity.

Another point to be aware of is that, during a measurement, the sample surface may undergo localised laser heating, what may lead to its alteration if the laser power density is high enough. Thus, the latter parameter needs to be optimised in each experiment, taking into account the particular sensitivity of the sample to alteration effects such as oxidation or thermal decomposition. Other parameters that require optimisation are, essentially, the acquisition time (dependent on the accumulation time and the amount of such accumulations) and the hole width, both with the aim of obtaining a fine signal-to-noise ratio.

In our case, all those parameters were adequately selected according to the sample used and its form. The goal was to acquire a good quality Raman signal while avoiding undesirable oxidation, which would have directly affected the scope of this work. While the disks or fragments presented very low sensitivity under the laser beam, probably due to their lower specific surface [20], care needed to be taken when using powdered samples. For example, UO_2 and intermediate uranium oxides (UO_{2+x} and U_4O_9) in the form of powder easily oxidised to higher oxides if the laser power density was not sufficiently low (as can be observed in Result 3); and U_3O_8, which only appears as powder, underwent degradation so readily that the laser power density required to be substantially decreased for performing the measurements. By extension, when working with highly sensitive samples, in particular those powdered, longer acquisition times (of the order of 300 seconds x 6 accumulations) were needed to attain a Raman spectrum with a suitable signal-to-noise ratio, given the lower laser power densities applied. Actually, in most of these cases the sum of several spectra was additionally carried out in order to enhance the final spectrum quality.

Furthermore, every Raman spectrum shown in the following chapters was subjected to calibration, which is a key aspect to prevent uncertainties derived from temperature or improper laser alignment effects. The spectra acquired with the Raman spectrometer available at CIEMAT were calibrated by registering, immediately after the acquisition of each spectrum, the emission lines of a Ne lamp in the same wavenumber interval (see Figure 2.14 as an example). Since these lines are perfectly known [21], their expected position (wavenumber) values were plotted against the observed ones and, thus, the corresponding calibration equation was obtained from the linear fitting of the plotted data. This equation was then applied to the X-axis of the Raman spectrum for its calibration. Figure 2.15 shows an illustrative example of the latter procedure. In contrast, at JRC Karlsruhe facilities it was the spectrometer which was daily calibrated, prior to the Raman measurements, using the T_{2g} phonon (520.5 cm^{-1}) of a silicon single crystal [22].

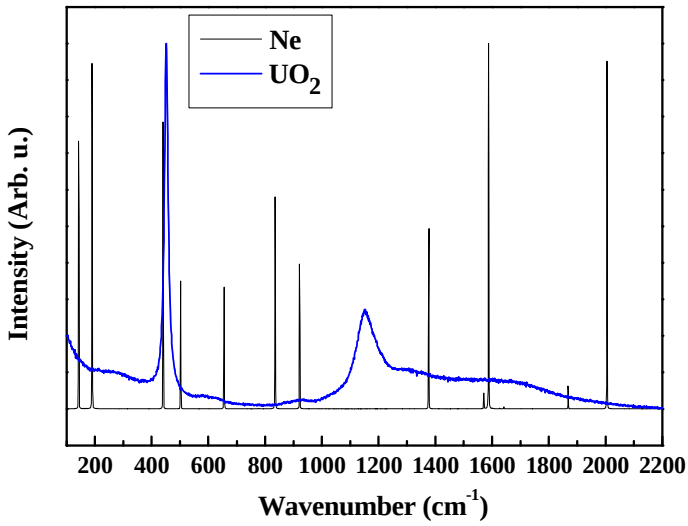

Fig. 2.14. First step of the calibration procedure followed at CIEMAT, consisting in acquiring the emission lines of a Ne lamp right after acquiring the Raman spectrum of interest.

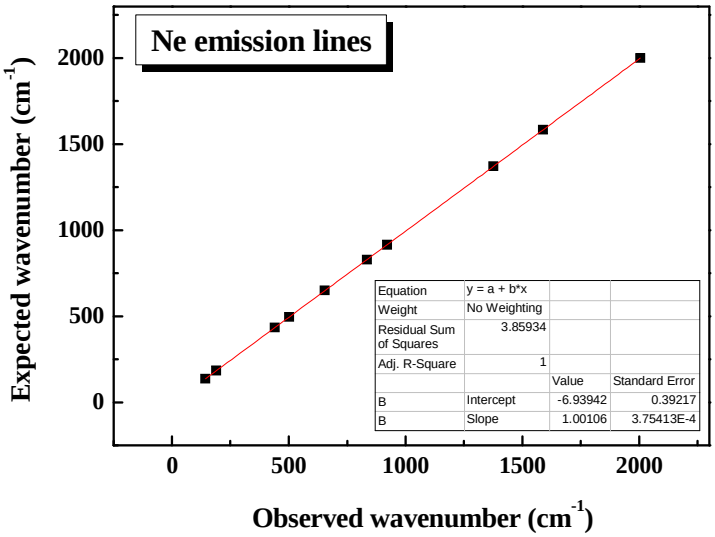

Fig. 2.15. Second step of the calibration procedure followed at CIEMAT, consisting in plotting the wavenumber values expected for the Ne lines present in the measured interval vs. the observed values, for the purpose of obtaining the calibration equation from their linear fitting.

2.5.2. Second derivative analysis and peak fitting

At this point, the treatment and processing conducted on the calibrated spectra should be described. In order to accurately determine the different experimental observables obtainable from a Raman spectrum, a profile analysis needs to be carried out. Such profile analysis entailed, in the major part of the studies compiled in this thesis, a first step concerning the second derivative spectral methodology [23] and a second step related to the peak fitting. Anyhow, this treatment was reduced to the exclusive application of the second derivative analysis in those cases where only information on the bands positions was required or the signal-to-noise ratio was not good enough to perform a reliable peak fitting on some spectral regions.

The second derivative analysis method enables identifying the various bands present in a Raman spectrum, which appear as minima (see Figure 2.16a), and obtaining their precise position without being affected by the background.

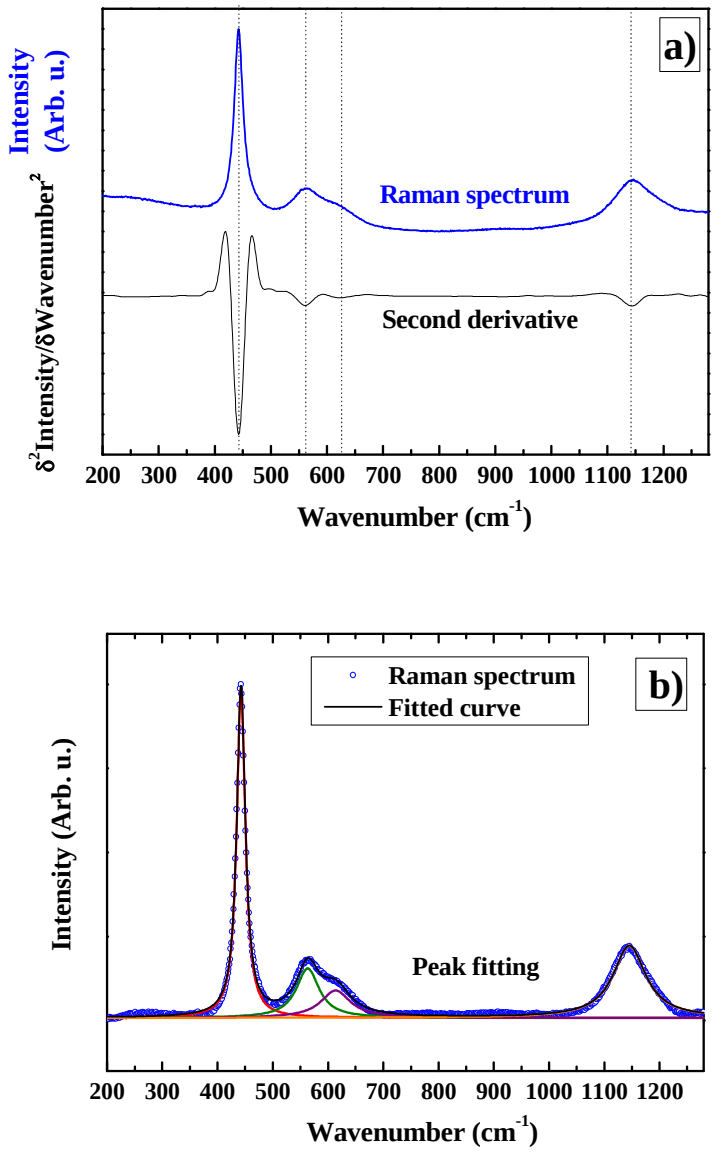

Fig. 2.16. a) Second derivative analysis (bottom) performed on a calibrated Raman spectrum corresponding to a hyperstoichiometric oxide (top), where four bands were identified. b) Lorentzian multiple peak fitting carried out on the latter Raman spectrum after subtracting the background.

Since, conversely, background subtraction is necessary for the peak fitting, what may lead to artefacts in the spectrum and spurious bands, it seems that the previous performance of the second derivative analysis helps to provide reliance on the bands positions determination. Besides, this method becomes very useful when some contributions are close to each other, given that it makes it possible to identify how many of them are there, as shown in the 500-700 cm^{-1} region of Figure 2.16a.

Therefore, the combination of the second derivative analysis with a subsequent peak fitting provides more accurate information than the one that peak fitting alone would provide. In this way, the bands positions obtained in the second derivative analysis of each Raman spectrum were used as starting parameters in the peak fitting. The spectral bandshapes were in all cases found to be well represented by Lorentzian functions (Figure 2.16b), what thereby determined their corresponding bandwidth and integrated intensity values. These two characteristic parameters, together with the bands positions, allowed us to obtain valuable information on the analysed samples, as will be shown in the successive chapters.

2.6. References

[1] A. Smekal, *Naturwissenschaften*, **11**, 873–875 (1923).
[2] C. V. Raman and K. S. Krishnan, *Nature*, **121**, 501–502 (1928).
[3] G. Panczer, D. De Ligny, C. Mendoza, M. Gaft, A. Seydoux-Guillaume and X. Wang, *Raman and fluorescence*, Raman Spectroscopy Applied to Earth Sciences and Cultural Heritage, J. Dubessy, M. -C. Caumon and F. Rull (Eds.), EMU Notes in Mineralogy, **12**, 61-82, European Mineralogical Union (2012).
[4] A. Requena and J. Zuñiga, *Espectroscopía*, PEARSON EDUCACIÓN, S.A., Madrid (1994). ISBN 84-205-3677-6.
[5] R. P. Feynman, *The Strange Theory of Light and Matter*, Princeton University Press, Princeton, New Jersey, USA (1985).
[6] W. Willes and R. Merlin (Eds.), *Raman Scattering in Materials*, Springer Series in Materials Science, **42**, Springer-Verlag, Berlin (2000).
[7] L. J. Bonales, J. M. Elorrieta, A. Lobato and J. Cobos, *Raman Spectroscopy, a Useful Tool to Study Nuclear Materials*, Applications of Molecular Spectroscopy to Current Research in the Chemical and Biological Sciences, Dr. Mark Stauffer (Ed.), InTech (2016).

[8] F. Rull, *The Raman Effect and the vibrational dynamics of molecules and crystalline solids*, Raman Spectroscopy Applied to Earth Sciences and Cultural Heritage, J. Dubessy, M. -C. Caumon and F. Rull (Eds.), EMU Notes in Mineralogy, **12**, 1-60, European Mineralogical Union (2012).
[9] F. Albert Cotton, *Chemical Applications of Group Theory*, Wiley (1990). ISBN 10: 0471510947.
[10] H. Knözinger, *Catalysis Today*, **32**, 71-80 (1996).
[11] C. V. Raman, *Proc. Indian Acad. Sci.*, **26**, 339 (1947).
[12] P. K. Narayanaswamy, *Proc. Indian Acad. Sci.*, **26**, 511 (1947).
[13] Z. Dohcevic-Mitrovic, Z. V. Popovic, and M. Scepanovic, *Acta Phys. Pol. A*, **116 (1)**, 36–41 (2009).
[14] R. S. Krishnan, *Proc. Indian Acad. Sci.*, **24**, 45 (1946).
[15] P. Verma, S. C. Abbi and K. P. Jain, *Phys. Rev. B*, **51**, 16660 (1995).
[16] M. Millot, R. T. Zaera, V. M. Sanjose, B. J. Marc and J. Gonzalez, *Appl. Phys. Lett.*, **96**, 152103 (2010).
[17] K. Samanta, P. Bhattacharya and R. S. Katiyar, *Phys. Rev. B*, **75**, 035208 (2007).
[18] D. N. Sathyanarayana, *Vibrational Spectroscopy: Theory and Applications*, New Age International (P) Ltd., New Delhi (2004). ISBN: 81-224-1517-2.
[19] M. Naji, J.-Y. Colle, O. Benes, M. Sierig, J. Rautio, P. Lajarge and D. Manara, *J. Raman Spectrosc.*, **46**, 750-756 (2015).
[20] R. J. McEachern and P. Taylor, *J. Nucl. Mater.*, **254**, 87-121 (1998).
[21] R. Lide, *Handbook of Chemistry and Physics*, CRC Press: Boca Ratón, Florida (1990).
[22] H. Richter, Z. Wang, and L. Ley, *Solid State Commun.*, **39**, 625 (1981).
[23] G. Talsky, *Derivative Spectrophotometry: Low and High Order*, Verlagsgesellschaft, Weinheim (Federal Republic of Germany) and Inc., New York, NY (USA), 1994. ISBN 3-527-28294-7.

Part 3

Main results

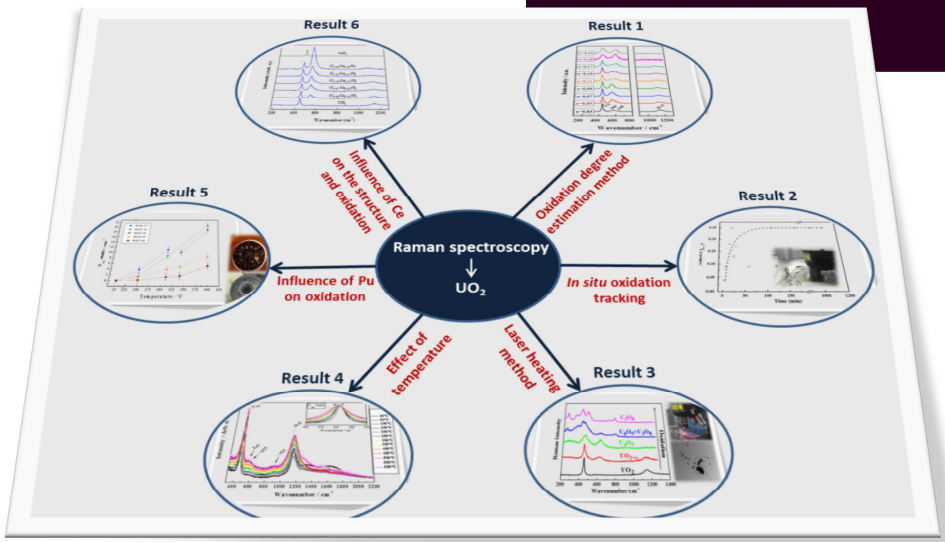

Result 1

Setting up a quantitative Raman method for the oxidation degree estimation in UO_{2+x}

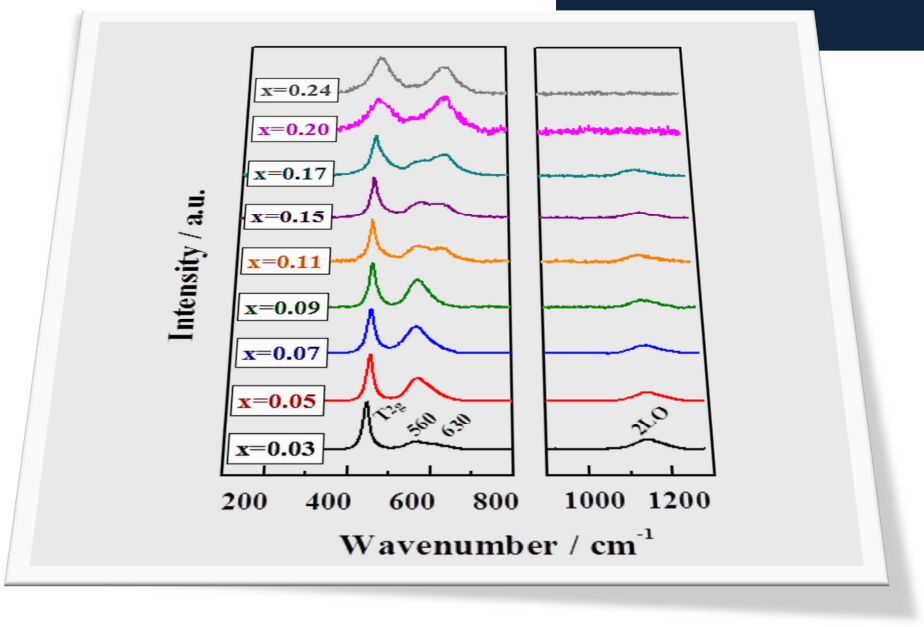

Published as "A detailed Raman and X-ray study of UO_{2+x} oxides and related structure transitions", **J. M. Elorrieta, L. J. Bonales, N. Rodríguez-Villagra, V. G. Baonza and J. Cobos**, *Phys. Chem. Chem. Phys.*, **18**, 28209-28216 (2016). DOI: 10.1039/c6cp03800j

Abstract

This work presents a detailed study of hyperstoichiometric UO_{2+x} ($0 < x < 0.25$) oxides and an assessment of the structural evolution taking place as oxidation proceeds. For this purpose, different UO_{2+x} powder samples, with controlled degree of non-stoichiometry, have been identified by thermogravimetric analysis and characterised by X-ray diffraction (XRD) and Raman spectroscopy. XRD analysis reflects that the commonly assumed Vegard's law is not applicable over the whole hyperstoichiometry range, since a slight increase of the lattice parameter is observed for $0.13 < x < 0.20$. A quantitative Raman analysis of the UO_{2+x} spectra as a function of the oxidation degree is also shown. A new method to characterise any UO_{2+x} sample (for $x < 0.20$), based on the shift of the 630 cm^{-1} band observed in the Raman spectrum, is proposed here for the first time. Moreover, three structure transitions have been detected at $x = 0.05$, 0.11 and 0.20, giving rise to four distinct regions associated with consecutive structural rearrangements over the hyperstoichiometry range: $x < 0.05$, $0.05 < x < 0.11$, $0.11 < x < 0.20$ and $0.20 < x < 0.25$.

3.1.1. Introduction

The oxidation of uranium dioxide (UO_2) has been widely studied due to the potential risks that this process may cause in the event of shielding failure during the storage of such a nuclear fuel [1]. In case of failure under dry interim storage conditions, the UO_2 matrix of the spent nuclear fuel (SNF) might be oxidised owing to its contact with the atmospheric oxygen and the high temperatures present due to the decay heat of the SNF [2]. The transformation of UO_2 into U_3O_8 via the two-step reaction [1] $UO_2 \rightarrow U_4O_9/U_3O_7 \rightarrow U_3O_8$ entails an increase in volume of around 36% and, consequently, it might cause the loss of integrity of the UO_2 matrix. Since this fuel matrix is responsible for retaining the fission products and transuranium elements formed by the irradiation process, release of radionuclides into the biosphere might occur.

UO_2 presents a fluorite-type crystal structure (*Fm-3m* space group, fcc), where uranium U^{4+} ions occupy the octahedral sites and oxygen ions (O^{-2}) are located in the tetrahedral positions [3]. Owing to the presence of numerous empty

interstitial sites, the UO_2 lattice is capable of accommodating additional oxygen ions. A slight lattice distortion in the cubic structure arises from the appearance of such point defects, thus leading to hyperstoichiometric UO_{2+x} [4]. As the amount of incorporated oxygen increases, the structure rearranges and extended defect-structures are formed. The most energetically favourable defect-structure proposed for around $UO_{2.12}$ is the 2:2:2 Willis cluster, which contains two anion vacancies, two <111> interstitial oxygens and two <110> interstitial oxygens, with no appreciable alteration of the uranium sublattice [5,6]. The limit phase preserving the fluorite structure is U_4O_9 [7], recently described as a superstructure of UO_2 consisting of "clusters of interstitial oxygen atoms embedded in a distorted UO_2 lattice" [8]. Further oxidation produces a change from the cubic to the tetragonal structure, corresponding to U_3O_7 [9], in which the cuboctahedral clusters are so close to each other (even sharing edges) that the cubic lattice suffers distortion and, subsequently, the *c/a* lattice parameters ratio is no longer equal to 1 [10]. He and Shoesmith [6] studied the defect structures and phase transition in hyperstoichiometric UO_{2+x}, also including the tetragonal region of U_3O_7 ($0 < x < 0.33$ in UO_{2+x}), and identified four structural defect regions over the stoichiometry range: i) a random point defect structure ($x \leq 0.05$); ii) a non-stoichiometry region where point defects are gradually substituted by Willis 2:2:2 clusters ($0.05 \leq x \leq 0.15$); iii) a mixture of Willis and cuboctahedral clusters ($0.15 \leq x \leq 0.23$); and iv) cuboctahedral clusters ($x \geq 0.23$). Furthermore, it is well known that accommodation of a higher amount of oxygens within the U_3O_7 lattice results in a phase transition to orthorhombic U_3O_8 [9].

Traditionally, the techniques employed to analyse the reaction of UO_2 at atmospheric conditions have mainly consisted in thermogravimetry and X-ray diffraction (XRD). Thermogravimetric analyses reveal the kinetic behaviour of UO_2 under these conditions, as well as the different mechanisms involved in each step of the process: diffusion governs the oxidation to U_4O_9/U_3O_7 (parabolic reaction kinetics) while the following step to U_3O_8 is controlled by a nucleation and growth mechanism (sigmoidal reaction kinetics) [1]. Nevertheless, there are some uncertainties that have not yet been clarified, such as the real number of kinetic time domains and their detailed origin, as suggested by the studies carried out by Rousseau *et al.* [11] and Quémard *et al*. [12] On the other hand, XRD characterisation has not only managed to determine the evolution of the already mentioned crystalline phases throughout the reaction [13] but, specifically, the change in the lattice parameter of UO_2 during its transformation to U_4O_9/U_3O_7 (hyperstoichiometric range) [7,14-19]. A Vegard's law-like behaviour over the

whole hyperstoichiometric range has been proposed to explain such changes, but some scatter of the results is observed and discrepancies arise for the transition in the $0.125 < x < 0.17$ region [15]. This may be due to the complex oxide phase transformations that take place during the oxidation reaction [11].

In recent years, an emerging technique like micro-Raman spectroscopy is gaining ground, since it meets two relevant features: it allows focusing on a particular area of the size of few micrometres, and provides a spectral fingerprint to differentiate between chemically similar compounds. Raman spectra of several uranium oxide phases, such as UO_2, U_4O_9, U_3O_7 and U_3O_8 have been previously published [8,20-23]. Likewise, some studies have achieved to identify a progressive variation of the UO_{2+x} Raman spectrum according to the degree of non-stoichiometry [6,24,25]. However, none of these studies has analysed this variation both quantitatively and associating a specific stoichiometry (x in UO_{2+x}) to each spectrum.

In spite of the large number of studies that have been carried out on this matter, a more specific characterisation of the different uranium oxides involved in the conversion of UO_2 into U_3O_8 needs to be done for a better understanding of the structural and chemical evolution of the system. On this basis, the present study is focused on the first oxidation stage, from UO_2 to U_4O_9, with the aim of characterising the UO_{2+x} ($x < 0.25$) hyperstoichiometric oxides in detail. For this purpose, several UO_{2+x} oxides with x ranging from ~ 0 to ~ 0.25 have been prepared, their stoichiometries have been checked by thermogravimetric analysis and characterised by Raman spectroscopy and XRD. Our aim here is to shed some light on the structural evolution of the $UO_2 \rightarrow U_4O_9$ reaction, based on the analysis of the measured lattice parameters and Raman shifts of a UO_{2+x} series of compounds.

3.1.2. Experimental

3.1.2.1. Sample preparation

U_3O_8 powder provided by ENUSA was reduced in an alumina furnace at 1000°C under a constant N_2:H_2 96:4.7 v/v gas flow to ensure that quasi-stoichiometric UO_2 powder was obtained. Afterwards, this powder was subjected to different times and temperatures in air atmosphere in order to attain homogeneous UO_{2+x} specimens with x ranging from ~ 0 to ~ 0.25. In this way,

nine samples were prepared and their stoichiometry thereafter determined by thermogravimetric analysis.

3.1.2.2. Characterisation techniques

Thermogravimetry experiments were carried out by means of a TA Instruments Q50 thermobalance under a synthetic air flow with a constant rate of 60 mL per minute. The samples were heated to 700°C in order to attain a complete conversion to U_3O_8. The weighing precision of the thermobalance was 0.01%. The O/U atomic ratios of the initial samples were then calculated by assuming that oxidation to U_3O_8 was fully completed. U_3O_8 complexion was afterwards verified by XRD (data not shown).

Raman spectroscopy analyses were performed with a Horiba LabRAM HR Evolution spectrometer with 800 mm focal length. All spectra were acquired at an excitation wavelength of 632.8 nm provided by a He-Ne laser. The laser beam was focused on the sample through the 100x objective of an Olympus BX41 microscope. The excitation power was optimised and minimised to ~ 1 mW in order to avoid alteration of the samples. The scattered radiation was then collected in backscattering geometry, dispersed using a 600 grooves/mm holographic grating and recorded using a CCD detector (256 x 1024 pixels), obtaining a ~1 cm^{-1}/ pixel spatial resolution and a spectral resolution better than 3 cm^{-1}. For the analysis of each sample, an average of 20 spectra recorded at different locations of the sample were acquired over the wavenumber range that goes from 250 to 1300 cm^{-1}.

XRD characterisation was performed by means of a Philips PANalytical X'Pert MPD diffractometer using Cu K_α radiation (λ=1.54056 Å) and operating at 45 kV and 40 mA. Bragg-Brentano configuration geometry was used. The 2θ range covered was from 20° to 120°, at 0.04° scanning steps. Four to six XRD patterns were acquired under identical conditions for each sample. The uncertainty of each XRD measurement was estimated as the standard deviation of the individual measurements.

Both Raman and XRD experiments were performed in air under STP conditions.

3.1.3. Results and discussion

3.1.3.1. Thermogravimetric analysis

Figure 3.1.1 shows the thermogravimetric curves obtained for selected samples, which reflect the typical two-step oxidation of UO_2 ($UO_2 \rightarrow U_4O_9/U_3O_7 \rightarrow U_3O_8$) [1]. All the samples present a similar general behaviour when heating them to 700ºC: a weight gain is first observed when a temperature of 200-250ºC is reached; at that point, the samples begin to oxidise (weight gain increase) until a plateau appears at around 300-400ºC, associated with U_4O_9/U_3O_7 [26]; finally, oxidation continues and at 450-500ºC another plateau is reached, indicating that conversion to U_3O_8 has been fully completed [26].

The stoichiometry of the different samples was calculated from the weight-gain data recorded in the thermogravimetric analyses, thus determining their correspondence to the hyper-stoichiometric oxides $UO_{2.03}$, $UO_{2.05}$, $UO_{2.07}$, $UO_{2.09}$, $UO_{2.11}$, $UO_{2.15}$, $UO_{2.17}$, $UO_{2.20}$ and $UO_{2.24}$, with a relative sampling error around 1%.

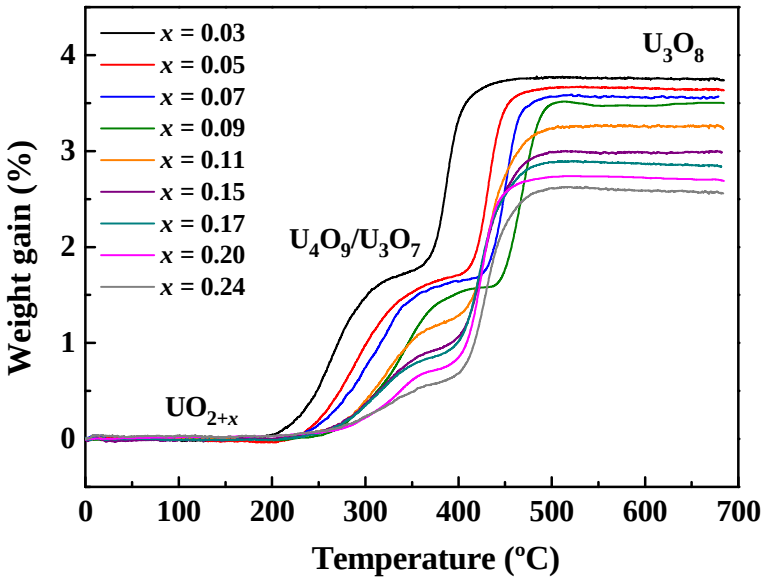

Fig. 3.1.1. Thermogravimetric curves of the UO_{2+x} hyper-stoichiometric oxides.

It should be noted in Figure 3.1.1 that each hyperstoichiometric oxide starts to oxidise at a different temperature, which is lower as the initial degree of non-stoichiometry increases. Likewise, the first (short) plateau reached, related to U_4O_9/U_3O_7 [26], is narrower for more oxidised samples. It can also be appreciated that the oxidation rate (slope) in both steps ($UO_{2+x} \rightarrow U_4O_9/U_3O_7$ and $U_4O_9/U_3O_7 \rightarrow U_3O_8$) significantly varies for the different hyperstoichiometric oxides, especially in the initial transformation to U_4O_9/U_3O_7.

3.1.3.2. XRD analysis

Typically three X-ray diffractograms were acquired for each sample. As an example, we show in Figure 3.1.2 selected reflections of the different oxides patterns: (111), (200), (220) and (311). For the sake of comparison, we reproduce (open symbols) the diffraction pattern of the cubic structure of stoichiometric UO_2 reported by Fritsche (ICDD 00-041-1422) [27].

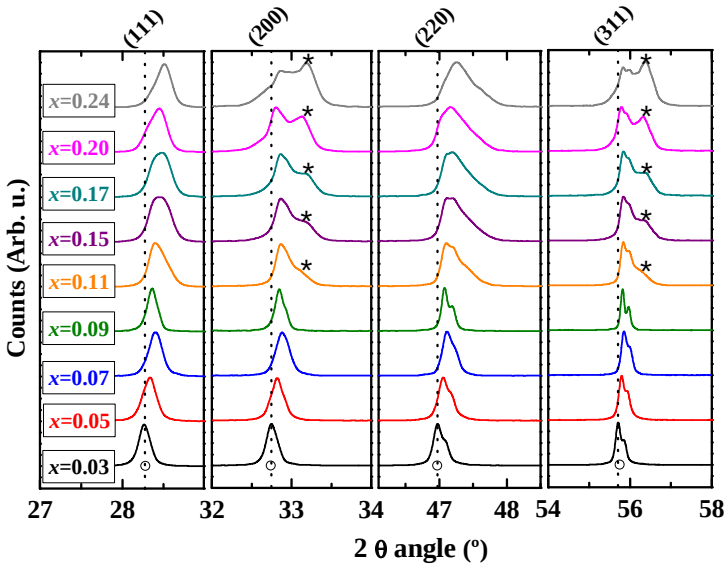

Fig. 3.1.2. Comparison of the (111), (200), (220) and (311) XRD reflections of the hyperstoichiometric oxides studied. Asterisks indicate the appearance of a new diffraction peak. Open symbols correspond to the ICDD 00-041-1422 UO_2 pattern [27].

A general upshift in 2θ of all the peaks can be appreciated as the degree of non-stoichiometry increases, being particularly remarkable for the (111) reflection (see dotted line in Figure 3.1.2). It is also noteworthy that both (200)

and (311) reflections show satellite peaks at higher angles (asterisks in Figure 3.1.2) from $UO_{2.11}$ on, their contributions becoming more relevant with increasing x. This has been attributed both to the U_3O_7 tetragonal phase and to the U_4O_9 cubic superlattice [28-31], and their observation must be related to the formation of cuboctahedral oxygen clusters, as postulated by Nowicki *et al*. [32], because U_4O_9 and U_3O_7 polytypes only differ in the spatial arrangement of such clusters and the subsequent lattice distortion.

In order to quantify the evolution of the structure with x, the lattice parameter (a_0) of every UO_{2+x} oxide was calculated from the results shown in Figure 3.1.2 applying Bragg's law and assuming that the system remains cubic throughout the whole hyperstoichiometric range [7]; the analysis is shown in Figure 3.1.3, showing rather good agreement with data from other authors measured under similar conditions [14-18]. Differences observed with the results of Lynds *et al.* [15] in the $0.7 < x < 0.12$ range might be due to the elevated-temperature quenching treatment performed by these authors during sample preparation.

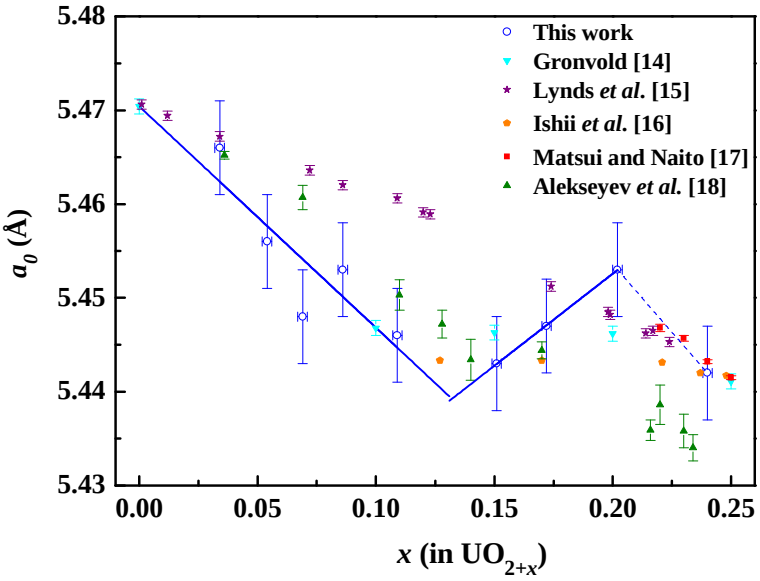

Fig. 3.1.3. Lattice parameter as a function of x for the different UO_{2+x} oxides. Open symbols represent experimental data obtained in this work, whereas solid symbols illustrate data published by other authors indicated in the legend. Straight lines correspond to linear fits (see text for details).

The variation of the UO_{2+x} lattice parameter is assumed to follow Vegard's law in the hyperstoichiometric range ($0 < x < 0.25$) [7,14-18], which implies a linear decrease on the lattice parameter with an increase in the degree of non-stoichiometry. This law seems to hold in the $0 < x < 0.13$ range, but a change in the slope is observed around $x = 0.15$ to again decrease in the $0.17\text{-}0.22 < x < 0.25$ region, which is commonly associated with U_4O_{9-y} [15-17,33].

Vegard's law in the $0 < x < 0.13$ range yields Equation 3.1.1, which has been obtained from a linear fit to our experimental data.

$$a_0\,(\text{Å}) = 5.470 \pm 0.006 - (0.24 \pm 0.08)\,x, \quad (0 < x < 0.13) \qquad \text{(Eq. 3.1.1)}$$

The intercept in Equation 3.1.1, *i.e.* the lattice parameter for stoichiometric UO_2 (5.470 Å), is in good agreement with the values estimated by other authors [14,15,18,34]. Nevertheless, larger discrepancies are observed with the slopes reported by Lynds *et al.* [15] (-0.094) and Alekseyev *et al.* [18] (-0.1495), very likely due to the different preparation and measurement conditions employed by these authors.

In spite of the consensus observed for $x < 0.13$, some uncertainty was reported by Lynds *et al.* [15] concerning the variation of the lattice parameter in the intermediate region $0.13 < x < 0.17$. These authors obtained scattered results of the lattice parameter in this region and were unable to obtain a unique Vegard equation across the whole hyperstoichiometric range; instead, they split it into two different equations below $x = 0.13$ and above $x = 0.17$. They attributed this observation to a transition detected at $x = 0.125$ by some authors when analysing the partial molar free energy of oxygen in UO_{2+x} [35]. Moreover, scarce values concerning this intermediate region have been reported [14,16,18]. However, our results clearly demonstrate an increase of the lattice parameter in the region $0.13 < x < 0.20$, which can be described by Equation 3.1.2.

$$a_0\,(\text{Å}) = 5.4133 \pm 0.0005 + (0.196 \pm 0.003)\,x, \quad (0.13 < x < 0.20) \qquad \text{(Eq. 3.1.2)}$$

Previously published lattice parameter values within $0.13 < x < 0.20$ are indeed in accordance with the trend observed here; however, to the best of our knowledge, this is the first time that a non-Vegard behaviour is reported for this particular region. This obviously confirms that a single linear equation is not sufficient to calculate x over the whole UO_{2+x} range.

Concerning the lattice parameter in the $0.20 < x < 0.25$ region, *i.e.* U_4O_{9-y} range, it seems to follow a Vegard's law-like behaviour (dashed line in Figure

3.1.3), in accordance with results published by different authors [15-17,33]. Nevertheless, additional data are required in order to verify such tendency and to establish an equation over the entire U_4O_{9-y} region; ongoing work is being carried out in our laboratory on this subject. In any case, the important conclusion that can be derived from the results of Figure 3.1.3 is that it is impossible to give a reliable value of the oxidation degree (x) of a given UO_{2+x} oxide in the $0.05 < x < 0.25$ range only with the help of an X-ray pattern. So we need complementary techniques in order to properly characterise hyperstoichiometric oxides.

The above XRD results, however, help to identify two structural transitions at $x = 0.11$ and $x = 0.20$. As the oxidation degree increases, the lines of the XRD patterns fairly correspond to those of UO_2 (see Figure 3.1.2), except for their steady displacement to higher angles commonly associated with non-stoichiometry in UO_{2+x} [13]. Then, a change is appreciated starting around $x = 0.11$ with the appearance of a new peak next to some reflections (labelled with asterisks in Figure 3.1.2), which was already attributed to the formation of cuboctahedral oxygen clusters. This clearly might correspond to the transition observed at $x = 0.125$ by some authors [35], and agrees with the kink in the variation of the lattice parameter around $x = 0.13$. A second transition is observed at around $x = 0.20$, attributed to U_4O_{9-y}, as revealed by the trend of the lattice parameter, and the Vegard's law is recovered indicating that a lattice contraction is again taking place.

3.1.3.3. Raman spectra analysis

Several Raman spectra recorded at different points of every sample were analysed and compared. All spectra acquired for each particular oxide were very similar, thus confirming the homogeneity of the samples. Each spectrum plotted in Figure 3.1.4 corresponds to the average of at least 20 individual spectra to improve the signal-to-noise ratio, and each of these average spectra was then normalised to the maximum height of the T_{2g} band, located around 445 cm^{-1}.

Since the space group corresponding to the fluorite-type structure of uranium dioxide is *Fm-3m* (O_h) [36], group theory predicts two vibrational modes for UO_2: a triply degenerate Raman active mode (T_{2g}) and an infrared active mode (T_{1u}). The Raman spectrum of a stoichiometric UO_2 shows two bands located at 445 cm^{-1} and 1150 cm^{-1}, respectively [36]. The band observed around 445 cm^{-1} can therefore be attributed to the T_{2g} vibrational mode [37], while the band observed around 1150 cm^{-1} has been assigned by Livneh and Sterer [38] to a

second order longitudinal optic phonon (2LO), despite the fact that it was previously assigned to a crystal field electronic transition [39].

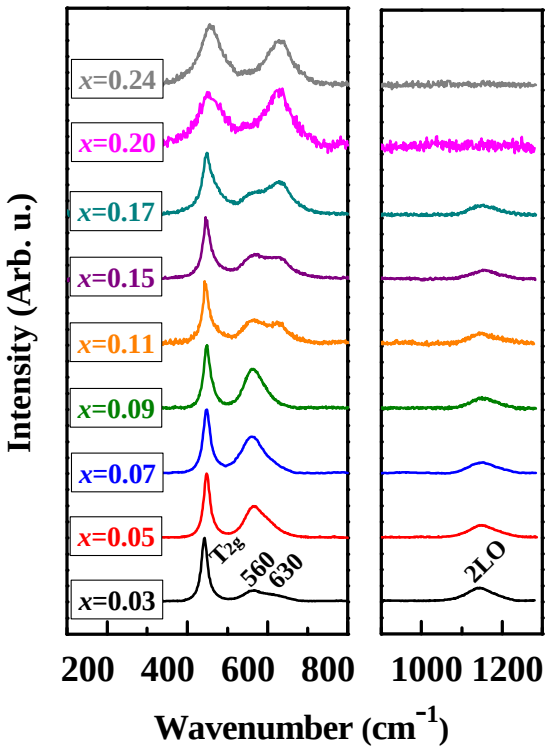

Fig. 3.1.4. Raman spectra of the UO_{2+x} hyper-stoichiometric oxides.

The initial hyperstoichiometric $UO_{2.03}$ spectrum contains the same Raman bands as stoichiometric UO_2 and an additional broad and asymmetric feature (500-700 cm^{-1}) which can be considered the result of two main contributions centred around 560 and 630 cm^{-1}. The first can be associated with the 555 cm^{-1} broad band observed by Guimbretière *et al.*[40] at the grain boundary of non-irradiated UO_2 and the one around 550 cm^{-1} found by Livneh and Sterer [38] when characterising UO_2 at low excitation energies, as well as with the so-called U* band in the recent study of Onofri *et al.* [41]. The band observed around 630 cm^{-1} has been attributed to anion sublattice distortions [11], which in our case would be caused by the excess of oxygen. However, this band has been also specifically associated with a structural defect of cuboctahedral (U_4O_9) symmetry [8].

The evolution of the Raman spectrum at different degrees of oxidation is shown in Figure 3.1.4. The changes observed can be summarised as follows: 1) a continuous broadening and upshifting of the 445 cm^{-1} band, 2) a significant decrease in intensity of the 2LO band, which essentially disappears at a certain point between $UO_{2.17}$ and $UO_{2.20}$, 3) a continuous increase in the intensity of the ~630 cm^{-1} band as the oxygen content increases, and 4) changes in the relative intensity of the ~560 cm^{-1} band, showing a maximum around $x = 0.09$.

A detailed band-profile analysis of the spectra was carried out to track the evolution of the characteristic wavenumbers, including those bands contributing to the broad feature observed in the 500-700 cm^{-1} spectral range. A second derivative analysis [42] allowed us to obtain the wavenumber of four main contributions, namely, the T_{2g} band at around 445 cm^{-1}, two overlapping bands at ~560 and ~630 cm^{-1} and the 2LO band at ~1150 cm^{-1}. Then, a multiple Lorentzian fit was conducted, using the obtained wavenumber values as fixed parameters. An example of this profile analysis is given in Figure 3.1.5 for $UO_{2.03}$ and $UO_{2.24}$ in the 300-800 cm^{-1} range. The following changes were found between the wavenumbers of the main Raman bands in both compounds: the 445 cm^{-1} band is shifted to 459 cm^{-1} for $UO_{2.24}$ and the bands observed at 562 and 623 cm^{-1} in $UO_{2.03}$ are centred at 547 and 637 cm^{-1} in $UO_{2.24}$.

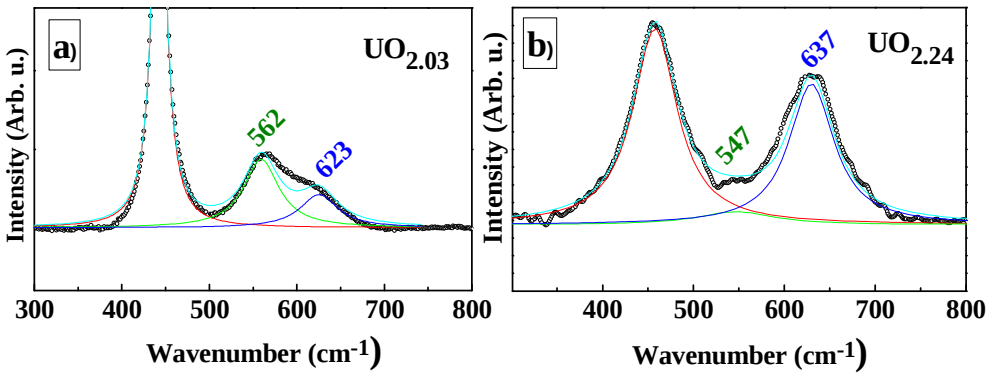

Fig. 3.1.5. Profile analysis of a) $UO_{2.03}$ and b) $UO_{2.24}$, illustrative of the two bands detected in the 500-700 cm^{-1} range for all UO_{2+x} oxides: the ~560 and ~630 cm^{-1} bands.

A quantitative analysis of the evolution of the Raman spectra with x, similar to that performed above with our XRD results, can be performed on the basis of the 445 cm^{-1} (T_{2g}) band shift, which provides information about the overall fluorite lattice, and the intensity and shift of the 630 cm^{-1} band, which can be

associated with a distorted oxygen sublattice [11]. As can be seen in Figure 3.1.6a, the 445 cm^{-1} band first upshifts from $UO_{2.03}$ to $UO_{2.05}$, and then remains almost constant in frequency until $UO_{2.11}$ is reached. At this point, the band begins to substantially move towards higher wavenumbers, reaching the value of 459 cm^{-1} for $UO_{2.24}$. Figure 3.1.6b shows the intensity (maximum height) of the 630 cm^{-1} band normalised with respect to the intensity (maximum height) of the T_{2g} band, *i.e.* I_{630}/I_{445}, as a function of *x*. As can be observed, the band at 630 cm^{-1} continuously increases in intensity as oxygen content increases. Concerning the wavenumber variation as a function of *x*, shown in Figure 3.1.6c, an initial downshift is appreciated until $UO_{2.09}$; at that point, it drastically shifts to a much higher wavenumber and continues downshifting from $UO_{2.11}$ to $UO_{2.20}$. Data corresponding to $UO_{2.24}$ do not follow the tendency of the latter oxides, what must be due to the fact that it belongs to the U_4O_{9-y} region, as indicated by the XRD results described above.

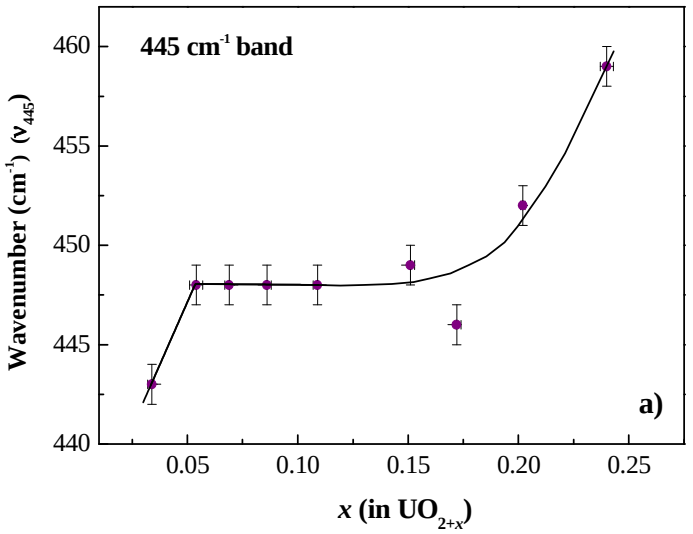

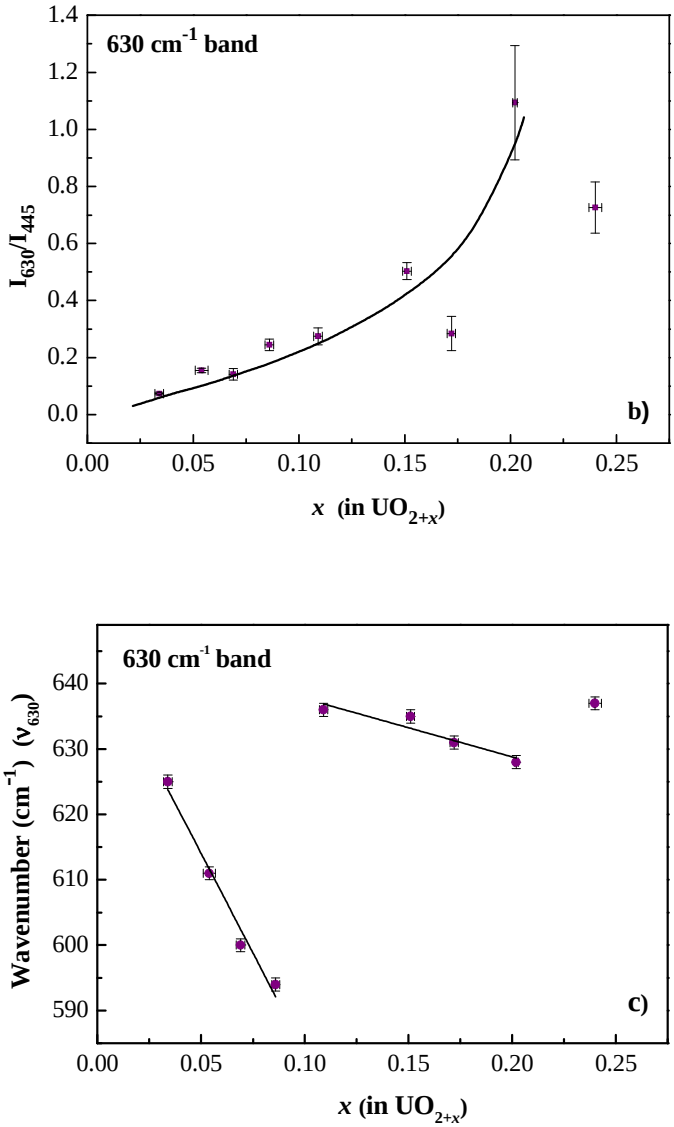

Fig. 3.1.6. a) Wavenumber of the 445 cm^{-1} band (v_{445}), b) normalised maximum intensity, with respect to the 445 cm^{-1} band, of the 630 cm^{-1} band (I_{630}/I_{445}) and c) wavenumber of the 630 cm^{-1} band (v_{630}), as a function of x (in UO_{2+x}). Lines are guides to the eye.

These results allow us to develop a reliable method to characterise the oxidation degree of any UO_{2+x} sample for $x < 0.20$ using Raman spectroscopy. Since the wavenumber of the 630 cm^{-1} band (v_{630}) shows two well defined and

differentiated trends before and after $UO_{2.09}$-$UO_{2.11}$ (Figure 3.1.6c), Equations 3.1.3 and 3.1.4 can be applied in different ranges of the I_{630}/I_{445} ratio (Figure 3.1.6b), which is directly related to x. It is important to note that these equations are only valid when an excitation wavelength of 632.8 nm is used, since it is well known that some excitation wavelengths may possibly lead to resonance conditions and no quantitative analysis could thus be carried out [8].

$$v_{630} = 645 \pm 4 - (610 \pm 60)\, x, \quad (I_{630}/I_{445} < 0.24) \qquad \text{(Eq. 3.1.3)}$$

$$v_{630} = 647 \pm 4 - (90 \pm 20)\, x, \quad (0.27 < I_{630}/I_{445} < 1.09) \qquad \text{(Eq. 3.1.4)}$$

Considering now the outcomes of the Raman spectroscopy characterisation, the same structure transitions as from XRD results can be detected around x = 0.11 and x = 0.20. These are remarkably noticed in the wavenumber evolution of the 630 cm^{-1} band, where clear discontinuities are found around these values of x (Figure 3.1.6c), revealing relevant changes in the anion sublattice. The transition at x = 0.11 can also be observed in the wavenumber evolution of the 445 cm^{-1} (T_{2g}) band, which shows an upshift at higher compositions (Figure 3.1.6a). The T_{2g} band is assigned to the U-O fundamental stretching vibration, so an upshift implies a gradual increase in the bond-strength for x > 0.11, what might be explained by a higher amount of surrounding oxygen atoms that produce U-O bond compression, thus confirming the idea that oxidation degree and pressure are related quantities [43]. On the other hand, the transition found at x = 0.20 is marked by vanishing of the 2LO band (Figure 3.1.4), what is commonly associated with a cation sublattice distortion significant enough to alter the special arrangement conditions which make such phonon band featurable [6]. Interestingly, an additional transition around x = 0.05, not identified in the XRD analysis, is suggested from the analysis of the shift of the T_{2g} band (Figure 3.1.6a). This band considerably upshifts from $UO_{2.03}$ to $UO_{2.05}$, very likely caused by a higher amount of surrounding oxygens when the composition $UO_{2.05}$ is reached.

3.1.3.4. Structural evolution in UO_{2+x}

Taking into account the transitions detected both by XRD and Raman analyses, four main regions with distinct behaviours within the UO_{2+x} range have been identified: x < 0.05, 0.05 < x < 0.11, 0.11 < x < 0.20 and 0.20 < x < 0.25. On this basis, the following structural evolution may be presumed:

i) $0 < x < 0.05$. As soon as quasi-stoichiometric UO_2 oxidation begins, the lattice starts to contract (marked upshift of the T_{2g} Raman band and a_0 lattice parameter decrease). This behaviour should be due to the progressive incorporation of oxygen atoms within interstitial sites [4]. He and Shoesmith identified the same region by analysing the small drop in intensity of the 2LO band and the slight increase in intensity of the 630 cm^{-1} band [6]. In this study we have observed a continuous decrease in intensity of the 2LO band and a continuous increase in intensity of the 630 cm^{-1} band around $UO_{2.05}$, with no detectable change in our band analysis.

ii) $0.05 < x < 0.11$. In this region, as extensively assumed, a_0 decreases following a Vegard's law-like behaviour. This can be interpreted as follows: at some point around $UO_{2.05}$, the concentration of interstitial oxygen is so high that oxygens start to rearrange themselves in an ordered manner to accommodate the additional oxygens entering the lattice, what yields a gradual lattice contraction due to the formation of new ordered defect structures: the so-called Willis clusters [5]. On the other hand, since the T_{2g} band wavenumber remains almost constant within this x range, the sublattice contraction is not significant, and some kind of structure rearrangement takes place, what would corroborate the Willis clusters assumption.

iii) $0.11 < x < 0.20$. The T_{2g} band gradually upshifts throughout this region, reflecting a continuous increase in the U-O bond-strength, what can be attributed to a higher and closer amount of surrounding oxygen atoms as oxidation proceeds. Hence the following structure evolution, assumed by He and Shoesmith over the $0.15 \leq x \leq 0.23$ range [6], can be taken into consideration: at around $UO_{2.11}$, part of the Willis defect structures start to develop to more densely packed regular distributions (cuboctahedral clusters) in order to allow further oxygen incorporation. This should involve a global gradual lattice expansion, as reflected by the increase in the a_0 lattice parameter observed in this study. In addition, the appearance of a new peak in the X-ray pattern at $UO_{2.11}$ confirms the latter assumption of an incipient formation of cuboctahedral clusters.

iv) $0.20 < x < 0.25$. Between $UO_{2.20}$ and $UO_{2.25}$, a_0 recovers the Vegard's law-like behaviour and the T_{2g} band continues upshifting, what indicates lattice contraction is again taking place. In addition, the disappearance of the 2LO band around $UO_{2.20}$ suggests distortion of the cation sublattice, which remained undisturbed at lower oxidation degrees, and the possible formation of U_4O_{9-y}

phase, since it has been previously associated with the 0.17-0.22 < x < 0.25 region [15-17,33]. This suggests that, when $UO_{2.20}$ is reached, the complete rearrangement of the oxygen atoms in cuboctahedral clusters leads to a new fully ordered superstructure containing oxygen vacancies (U_4O_{9-y}), which are progressively filled in, thus inducing once again a continuous contraction of the lattice.

3.1.4. Conclusions

A systematic Raman and XRD study of UO_{2+x} powder oxides with controlled degree of non-stoichiometry from x = 0.03 to x = 0.24 has been for the first time presented.

X-ray diffraction detailed analysis shows that the commonly assumed Vegard's law-like behaviour is not applicable to the whole hyperstoichiometric UO_{2+x} range. Three different equations are required to describe the lattice parameter evolution over such range and precludes using XRD results to calculate x. However, we have found that Raman spectroscopy can be used for this aim after the analysis of the 630 cm^{-1} Raman band and we have proposed a method to characterise the oxidation degree of any UO_{2+x} oxide (for x < 0.20).

The simultaneous analysis of the Raman and XRD results has allowed us to identify three structural transitions around x = 0.05, 0.11 and 0.20, and to provide an explanation of the structural evolution within the cubic lattice, as follows: i) up to $UO_{2.05}$, a progressive incorporation of oxygen atoms within interstitial sites occurs; ii) between $UO_{2.05}$ and $UO_{2.11}$, these point defects start to rearrange themselves in ordered defect structures or Willis clusters; iii) around $UO_{2.11}$, part of the Willis clusters start to develop into more densely packed cuboctahedral clusters; iv) finally, a complete rearrangement of the oxygen atoms in cuboctahedral clusters at around $UO_{2.20}$ leads to a new fully ordered superstructure containing oxygen vacancies (U_4O_{9-y}), which are gradually filled in up to at least $UO_{2.24}$.

3.1.5. Acknowledgements

This work was supported by ENRESA within the project Nº 079000189, entitled "Aplicación de técnicas de caracterización en el estudio de la estabilidad

del combustible nuclear irradiado en condiciones de almacenamiento" (ACESCO).

3.1.6. References

[1] R. J. McEachern and P. Taylor, *J. Nucl. Mater.*, **254**, 87-121 (1998).
[2] C. Ferry, C. Poinssot, C. Cappelaere, L. Desgranges, C. Jégou, F. Miserque, J. P. Piron, D. Roudil and J. M. Gras, *J. Nucl. Mater.*, **352**, 246-253 (2006).
[3] B. T. M. Willis, *Proc. Br. Ceram. Soc.*, **1**, 9-19 (1964).
[4] B. T. M. Willis, *Nature*, **197**, 755-756 (1963).
[5] B. T. M. Willis, *Acta Cryst.*, **A34**, 88-90 (1978).
[6] H. He and D. Shoesmith, *Phys. Chem. Chem. Phys.*, 2010, **12**, 8108-8117.
[7] H. Hering and P. Pério, *Bull Soc. Quim.*, **M. 531** (1952).
[8] L. Desgranges, G. Baldinozzi, P. Simon, G. Guimbretière and A. Canizares, *J. Raman Spectrosc.*, **43**, 455-458 (2012).
[9] P. Jolibois, *C. R. Acad. Sci.*, **224**, 1395-1396 (1947).
[10] L. Desgranges, G. Baldinozzi, G. Rousseau, J. C. Nièpce and G. Calvarin, *Inorg. Chem.*, **48**, 7585-7592 (2009).
[11] G. Rousseau, L. Desgranges, F. Charlot, N. Millot, J.C. Nièpce, M. Pijolat, F. Valdivieso, G. Baldinozzi and J. F. Berar, *J. Nucl. Mater.*, **355**, 10-20 (2006).
[12] L. Quémard, L. Desgranges, V. Bouineau, M. Pijolat, G. Baldinozzi, N. Millot, J. C. Nièpce and A. Poulesquen, *J. Eur. Ceram. Soc.*, **29**, 2791-2798 (2009).
[13] F. Grønvold and H. Haraldsen, *Nature*, **162,** 69-70 (1948).
[14] F. Grønvold, *J. Inorg. Nucl. Chem.*, **1,** 357-370 (1955).
[15] L. Lynds, W. A. Young, J. S. Mohl and G. G. Libowitz, *Adv. Chem.*, **39**, 58-65 (1962).
[16] T. Ishii, K. Naito and K. Oshima, *Solid State Commun.*, **8**, 677-683 (1970).
[17] T. Matsui and K. Naito, *J. Nucl. Mater.*, **56**, 327-335 (1975).
[18] V. A. Alekseyev, L. A. Anan'yeva and R. P. Rafal'skiy, *Int. Geol. Rev.*, **23**, 1229-1236 (1981).
[19] R. E. Rundle, N. C. Baenziger, A. S. Wilson and R. A. McDonald, *J. Am. Chem. Soc.*, **70**, 99-105 (1948).
[20] G. C. Allen, I. S. Butler and N. A. Tuan, *J. Nucl. Mater.*, **144**, 17-19 (1987).
[21] M. L. Palacios and S. H. Taylor, *Appl. Spectrosc.*, **54**, 1372-1378 (2000).
[22] E. A. Stefaniak, A. Alsecz, I. E. Sajó, A. Worobiec, Z. Máthé, S. Török and R. Van Grieken, *J. Nucl. Mater.*, **381**, 278-283 (2008).

[23] F. Pointurier and O. Marie, *Spectrochim. Acta, Part B*, **65**, 797-804 (2010).
[24] D. Manara and B. Renker, *J. Nucl. Mater.*, **321**, 233-237 (2003).
[25] L. Jun-bo, L. Gan and G. Shu-lan, *Spectrosc. Spect. Anal.*, **34 (2)**, 405-409 (2014).
[26] S. Aronson, R. B. Roof and J. Belle, *J. Chem. Phys.*, **27**, 137-144 (1957).
[27] R. Fritsche, Sussieck-Fornefeld C. Min.-Petr. Inst., Univ. Heidelberg, Germany, ICDD Grant-in-Aid (1988).
[28] P. A. Tempest, P. M. Tucker and J. W. Tyler, *J. Nucl. Mater.*, **151**, 251-268 (1988).
[29] P. Taylor, E. A. Burgess and G. G. Owens, *J. Nucl. Mater.*, **88**, 153-160 (1980).
[30] R. E. Einziger, L. E. Thomas, H. C. Buchanan and R. B. Stout, *J. Nucl. Mater.*, **190**, 53-60 (1992).
[31] K. Naito, T. Ishii, Y. Hamaguchi and K. Oshima, *Solid State Commun.*, **5**, 349-352 (1967).
[32] L. Nowicki, F. Garrido, A. Turos and L. Thomé, *J. Phys. Chem. Solids*, **61**, 1789-1804 (2000).
[33] B. E. Schaner, *J. Nucl. Mater.*, **2**, 110-120 (1960).
[34] B. Belbeoch, J. C. Boivineau and P. Pério, *J. Phys. Chem. Solids*, **28**, 1267-1275 (1967).
[35] C. F. Miller, U. Merten and J. T. Porter, *Chemistry of uranium-oxygen systems: Final report*, U.S. Atomic Energy Commission, Division of Technical Information, San Diego, California (1961).
[36] P. R. Graves, *Appl. Spectrosc.*, **144**, 1665-1667 (1990).
[37] P. G. Marlow, J. P. Russell and J. R. Hardy, *Philos. Mag.*, **14**, 409-410 (1966).
[38] T. Livneh and E. Sterer, *Phys. Rev. B*, **73**, 085118-085119 (2006).
[39] J. Shoenes, *J. Chem. Soc., Faraday Trans. 2*, **83**, 1205-1213 (1987).
[40] G. Guimbretière, L. Desgranges, A. Canizares, G. Carlot, R. Caraballo, C. Jégou, F. Duval, N. Raimboux, M. R. Ammar and P. Simon, *Appl. Phys. Lett.*, **100**, 251914 (2012).
[41] C. Onofri, C. Sabathier, H. Palancher, G. Carlot, S. Miro, Y. Serruys, L. Desgranges, M. Legros, *Nucl. Instrum. Meth. B*, **374**, 51-57 (2016).
[42] G. Talsky, *Derivative Spectrophotometry: Low and High Order*, Verlagsgesellschaft, Weinheim (Federal Republic of Germany) and Inc., New York, NY (USA) (1994). ISBN 3-527-28294-7.
[43] A. Vegas, J. Mejía-López, A. H. Romero, M. Kiwi, D. Santamaría-Pérez and V. G. Baonza, *Solid State Sci.*, **6**, 809–814 (2004).

Result 2

Monitoring early-stage oxidation of UO_2: An *in situ* Raman analysis

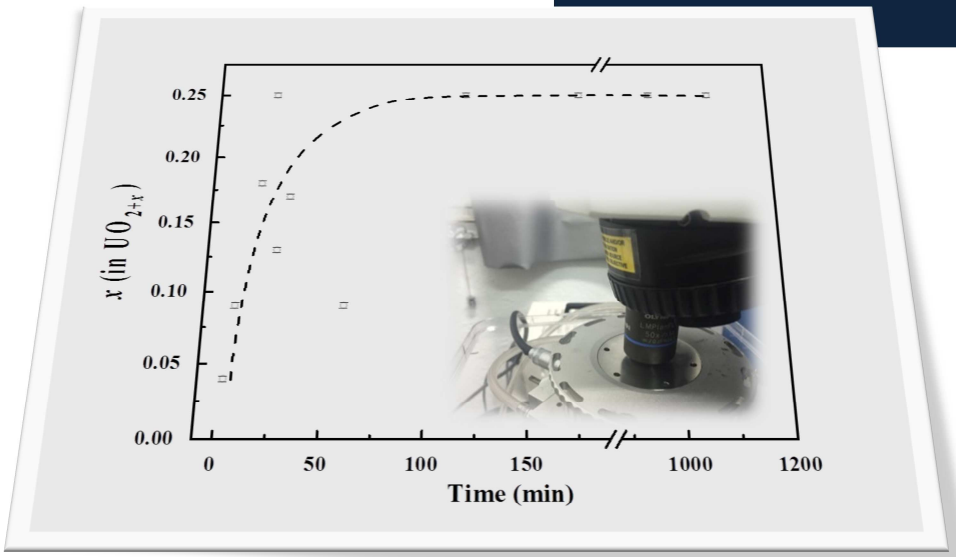

Published as "Spent fuel matrix oxidation studies under dry storage conditions" **J. M. Elorrieta, L. J. Bonales, N. Rodríguez-Villagra, V. G. Baonza and J. Cobos**, *MRS Advances*, **2 (12)**, 675-680 (2017). DOI: 10.1557/adv.2017.3

Abstract

A good understanding of the spent fuel matrix (UO_2) behaviour under predisposal activities conditions is required for the proper performance assessment of a final repository. Hence, the oxidation evolution of UO_2 under dry interim storage conditions, as a main predisposal action within the Spanish strategy, needs to be addressed. For this aim, in this work a detailed in situ Raman spectroscopy study of the surface oxidation of a $UO_{2.00}$ disk heated in the presence of synthetic air at 573 K is presented. The spectra analysis required two previous studies. In the first one, UO_{2+x} powder samples with controlled degree of non-stoichiometry were identified by thermogravimetric analysis and subsequently characterised by Raman spectroscopy. The equations obtained from this study enable estimating the oxidation degree of any UO_{2+x} sample (for $x < 0.20$) at atmospheric conditions. The second one was performed in order to use these equations for the in situ experiments (at 573 K), since the shift of the bands due to temperature needs to be taken into account. Thus, the behaviour of the Raman spectra as a function of temperature was analysed and a correction term thereafter introduced in the initial equations.

3.2.1. Introduction

It is of great significance to understand the oxidation behaviour of the spent nuclear fuel matrix (UO_2) under dry storage conditions in order to correctly assess the feasibility of interim repositories. If any shielding failure occurs while storing this irradiated fuel, the UO_2 matrix might oxidise in the presence of atmospheric oxygen and the high temperatures caused by decay heat [1], what entails an increase in volume of around 36% whether it becomes U_3O_8 [2]. The swelling produced under these conditions might make fuel pellets lose their integrity, what implies a risk for the future handling of such nuclear waste.

UO_2 presents a fluorite-type crystal structure (*Fm-3m* space group, fcc) [3]. The UO_2 lattice can easily accommodate additional oxygen ions owing to the presence of numerous empty interstitial sites, thus leading to hyperstoichiometric UO_{2+x} [4]. The cubic phase is then preserved up to around x = 0.25, usually

referred to as U_4O_9 [5]. Further oxidation produces a change from the cubic to the tetragonal structure, corresponding to $U_3O_{7,}$ and then to orthorhombic U_3O_8 [6].

Micro-Raman spectroscopy is one of the main characterisation techniques that are currently employed on this matter [7-14], due to the fact that it offers a series of advantages over other conventional techniques [15]; perhaps the most important is the possibility of performing *in situ* characterisation. For a better understanding of the structural and chemical evolution of the spent nuclear fuel matrix during its oxidation, a detailed *in situ* characterisation of the different uranium oxides involved in the conversion of UO_2 into U_3O_8 still needs to be done, both quantitatively and as a function of temperature. On this basis, the present study is focused on the first oxidation stage, from UO_2 to U_4O_9, with the aim of assessing the evolution of the UO_{2+x} ($x \leq 0.25$) hyperstoichiometric oxides formed on the surface of a UO_2 disk during its oxidation at 573 K (reasonably conservative value for the temperature that might be reached in an interim repository).

For this purpose, several UO_{2+x} powder oxides with x ranging from ~ 0 to ~ 0.25 were first prepared and quantitatively characterised by means of Raman spectroscopy [16]. In addition, a previous analysis of the Raman spectra as a function of temperature was carried out under inert atmosphere in order to later subtract the effect of temperature on the *in situ* obtained spectra under air conditions.

3.2.2. Experimental details

3.2.2.1. Sample preparation

U_3O_8 powder provided by ENUSA was reduced in an alumina furnace at 1273 K under a constant N_2:H_2 96:4 v/v gas flow to ensure that quasi-stoichiometric UO_2 powder was obtained. Afterwards, this powder was subjected to different times and temperatures in synthetic air atmosphere, thus attaining nine homogeneous UO_{2+x} oxides with x ranging from ~ 0 to ~ 0.25. A UO_2 pellet, also provided by ENUSA and with 10.4 mm in diameter, was cut into disks with parallel faces of ~1 mm thickness which were afterwards polished. In order to ensure stoichiometry, the disks were annealed at 1073 K during 24 hours under reducing conditions (N_2:H_2 96:4 v/v).

3.2.2.2. Characterisation techniques

For the purpose of determining the O/U ratio of every prepared UO_{2+x} powder oxide, thermogravimetry experiments were carried out by means of a TA Instruments Q50 thermobalance under a synthetic air flow with a constant rate of 60 mL/minute. The samples were heated up to 973 K in order to attain a complete conversion to U_3O_8. Their O/U atomic ratios were then calculated by assuming that oxidation to U_3O_8 was fully completed, hence determining their correspondence to the hyper-stoichiometric oxides $UO_{2.03}$, $UO_{2.05}$, $UO_{2.07}$, $UO_{2.09}$, $UO_{2.11}$, $UO_{2.15}$, $UO_{2.17}$, $UO_{2.20}$ and $UO_{2.24}$, with a relative sampling error around 1% (procedure and analysis described elsewhere [16]).

Raman spectroscopy analyses were performed with a Horiba LabRAM HR Evolution spectrometer. All spectra were acquired at an excitation wavelength of 632.8 nm provided by a He-Ne laser. The laser beam was focused onto the sample through the 100x objective of an Olympus BX41 microscope. The excitation power was optimised and minimised to avoid alteration of the samples. The scattered radiation was then collected in backscattering geometry, dispersed using a 600 grooves/mm holographic grating and recorded by a CCD detector (256 x 1024 pixels), obtaining a ~ 1 cm^{-1}/pixel spatial resolution and a spectral resolution better than 3 cm^{-1}.

In situ Raman characterisation of the UO_2 disk oxidation was carried out by using a Linkam temperature-controlled pressure stage, THMS600, coupled to the BX41 Olympus microscope of the Raman spectrometer. The mechanical design and electronics of the Linkam stage provided precise control and temperature stability better than 0.2 K. Spectra were in this case collected with a 50x long-range objective through a silica window at the top of the stage.

3.2.3. Results and discussion

3.2.3.1. Quantitative Raman analysis of UO_{2+x} oxides

Figure 3.2.1 shows the Raman spectra acquired for the different UO_{2+x} powder samples. All spectra contain the same Raman bands as stoichiometric UO_2 (the 445 cm^{-1} band corresponding to the U-O symmetric stretching vibration (T_{2g}) [17] and the 1150 cm^{-1} band associated with the 2LO phonon band [18]), as well as an additional broad and asymmetric feature at 500-700 cm^{-1} which can be considered

the result of two main contributions centred around 560 and 630 cm^{-1} [16]. The band observed around 630 cm^{-1} might be associated with the alteration caused by the excess of oxygen, *i.e.* with oxidation, since it is currently accepted that it can be attributed to anion sublattice distortions [19].

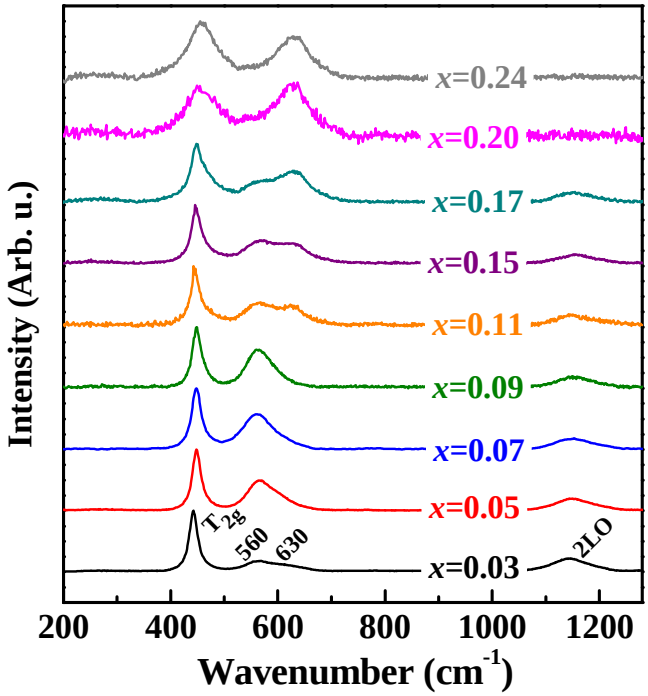

Fig. 3.2.1. Raman spectra of different UO_{2+x} hyper-stoichiometric oxides.

The evolution of the Raman spectrum as oxidation proceeds reveals a continuous broadening and upshifting of the 445 cm^{-1} band and a significant decrease in intensity of the 2LO band (which even disappears for $x > 0.17$, what could be related to the U_4O_9 phase [8]). Apart from this, a continuous growth of the ~ 630 cm^{-1} band can be appreciated as the oxidation degree increases. Thus, a quantitative analysis of both the intensity and wavenumber evolution of the 630 cm^{-1} band, as a function of x (in UO_{2+x}), allowed us to develop a reliable method to characterise the oxidation degree of any UO_{2+x} sample for $x < 0.20$ using Raman spectroscopy [16]. Such method consists basically in the direct relation between x and the wavenumber shift of the 630 cm^{-1} band (ν_{630}), represented by Equations 3.2.1 and 3.2.2, each of which takes into account a different range of the 630 and 445 cm^{-1} bands intensity ratio (I_{630}/I_{445}).

$$v_{630}\,(\mathrm{cm^{-1}}) = 645 \pm 4 - (610 \pm 60)\,x, \quad (I_{630}/I_{445} < 0.24) \qquad \text{(Eq. 3.2.1)}$$

$$v_{630}\,(\mathrm{cm^{-1}}) = 647 \pm 4 - (90 \pm 20)\,x, \quad (0.27 < I_{630}/I_{445} < 1.09) \qquad \text{(Eq. 3.2.2)}$$

3.2.3.2. Behaviour of the 630 cm^{-1} band with temperature

In order to assess the influence of temperature on the *in situ* acquired spectra during the UO_2 disk oxidation, especially on the 630 cm^{-1} band behaviour with the aim of correcting the latter equations, the $UO_{2.24}$ sample was previously subjected to a temperature scanning under inert atmosphere (Ar). In this regard, Figure 3.2.2a shows spectra acquired at different temperatures. Apart from the fact that the absolut intensity of the bands diminished with the increase of temperature (worse signal-to-noise ratio), a shift of the 630 cm^{-1} band towards lower wavenumber values could be appreciated (see dashed line in Figure 3.2.2a). Thus, the second derivative method [20] was applied to obtain the position of the 630 cm^{-1} band (v_{630}) for the different temperature values (see Figure 3.2.2b) and a correction equation, Equation 3.2.3, was subsequently derived from these data.

$$v_{630}\,(\mathrm{cm^{-1}}) = 650 \pm 2 - (0.049 \pm 0.003)\,T\,(\mathrm{K}) \qquad \text{(Eq. 3.2.3)}$$

Taking into account such temperature correction factor and assuming that it holds for the whole fluorite-hyperstoichiometry range, *i.e.* as long as the structure remains cubic, Equations 3.2.1 and 3.2.2 can be rewritten as Equations 3.2.4 and 3.2.5, which now describe the position of the 630 cm^{-1} band as a function of both oxidation degree (x) and temperature (T).

$$v_{630}\,(\mathrm{cm^{-1}}) = 660 \pm 10 - (610 \pm 60)\,x - (0.049 \pm 0.003)\,T\,(\mathrm{K}),\ (I_{630}/I_{445} < 0.24)$$

(Eq. 3.2.4)

$$v_{630}\,(\mathrm{cm^{-1}}) = 660 \pm 10 - (90 \pm 20)\,x - (0.049 \pm 0.003)\,T\,(\mathrm{K}),\ (0.27 < I_{630}/I_{445} < 1.09)$$

(Eq. 3.2.5)

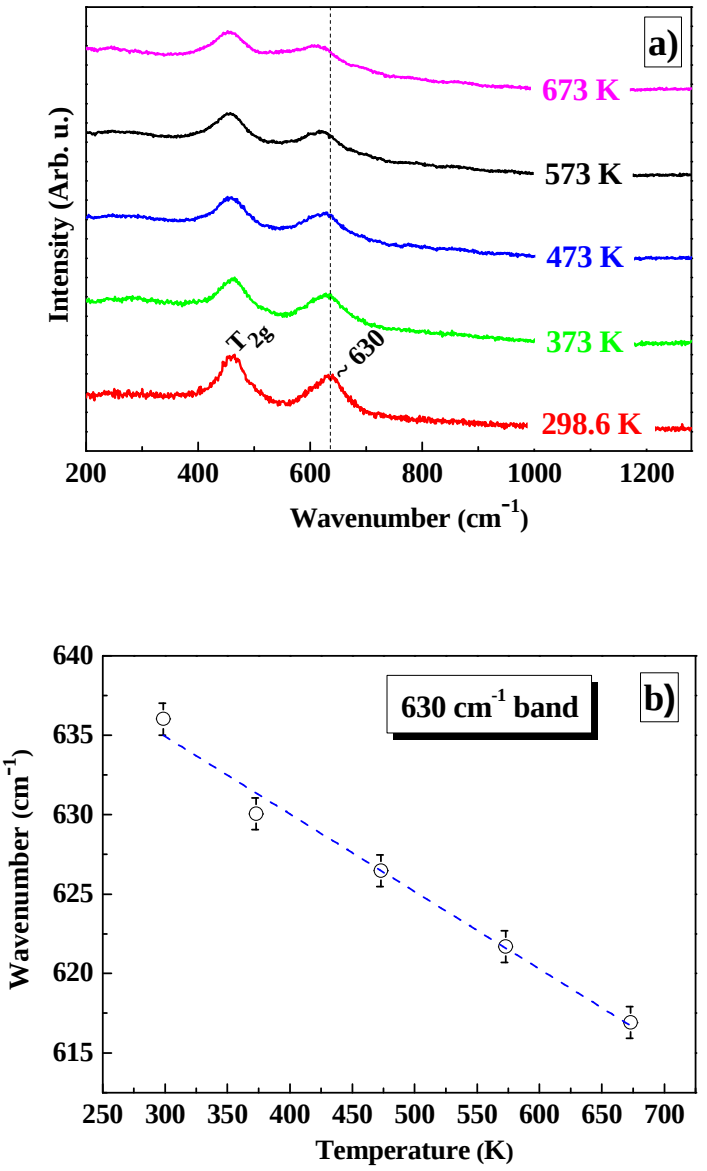

Fig. 3.2.2. a) Raman spectra of the $UO_{2.24}$ oxide at different temperatures under inert atmosphere. b) Position of the 630 cm^{-1} band (ν_{630}) of $UO_{2.24}$ as a function of temperature.

3.2.3.3. *In situ* characterisation of a UO_2 disk oxidation

For the *in situ* analysis of a UO_2 disk oxidation reaction, the latter was housed in the Linkam stage under synthetic air flow and temperature was then maintained at 573 K. Figure 3.2.3 shows spectra acquired on different spots of the sample surface as a function of time. As can be appreciated, under these conditions initial oxidation proceeded quite fast. During the first 10 hours a mixture of UO_{2+x} and U_4O_9 phases was observed, while after this time the U_4O_9 phase seemed to stabilise. Nevertheless, no surface oxidation to U_3O_8 was observed after 19 hours.

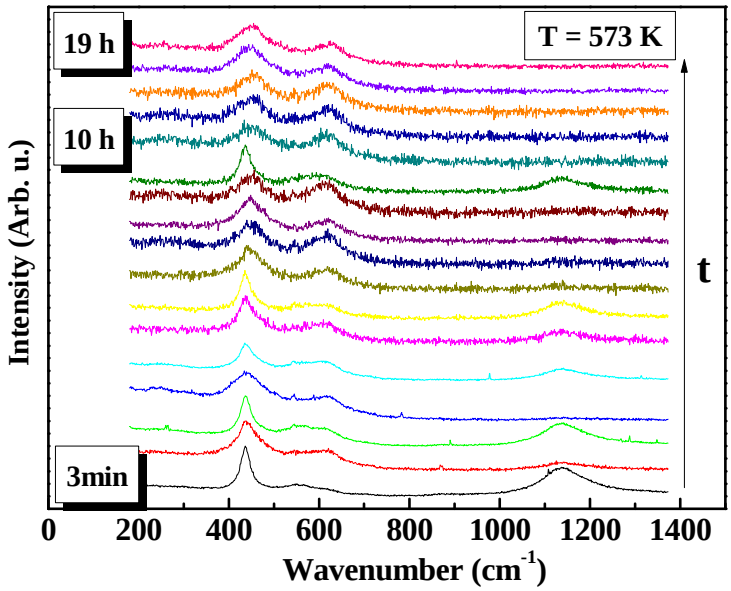

Fig. 3.2.3. Raman spectra of a UO_2 disk, acquired at different times of a 573 K experiment under dry air conditions.

For the purpose of performing a detailed spectral analysis, the second derivative method was again used. Thereafter, Equations 3.2.4 and 3.2.5 were applied to estimate the oxidation degree (x in UO_{2+x}) of the UO_2 disk as a function of time, which allowed us to better assess how the oxidation proceeded. Since these equations solely hold for $x < 0.20$ [16], every spectrum with no 2LO band was assumed to correspond to $x = 0.25$ (stoichiometric U_4O_9) for the sake of simplicity. The oxidation degree evolution of the UO_2 disk surface is reflected in Figure 3.2.4. Hence, it can be considered that a continuous oxidation took place

during the first two hours approximately, before the U_4O_9 phase was almost completely stabilised. This is in good agreement with other studies performed under similar conditions [19].

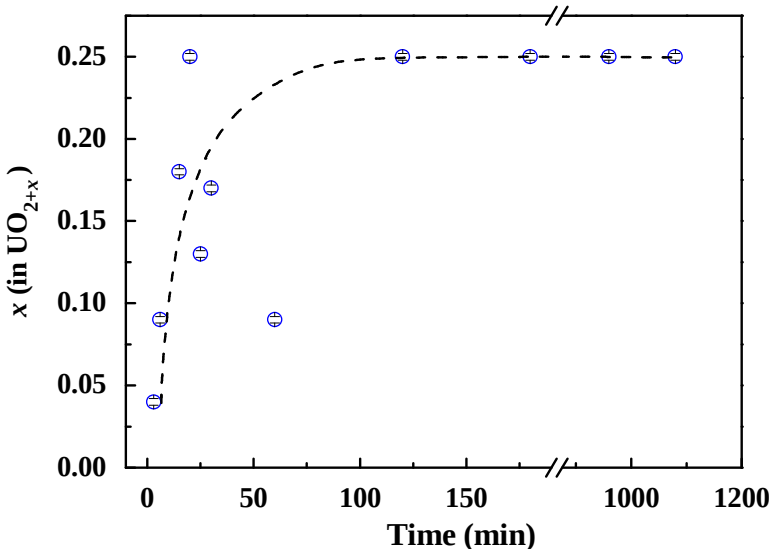

Fig. 3.2.4. Oxidation degree as a function of time of a UO_2 disk surface during a 573 K experiment under dry air conditions.

3.2.4. Conclusions

In situ characterisation of the oxidation of a UO_2 disk under repository conditions has been performed. For this aim, a systematic Raman study of UO_{2+x} powder oxides with controlled degree of non-stoichiometry from x = 0.03 to x = 0.24 was first carried out. The results attained from such study allowed us to propose new equations to characterise the oxidation degree of any UO_{2+x} (for x < 0.20) sample at room temperature, based on the analysis of the 630 cm^{-1} Raman band. A detailed study of the behaviour of the 630 cm^{-1} Raman band as a function of temperature under inert atmosphere was thereafter carried out in order to take into account the temperature effect on the latter equations. Therefore, by using the equations valid at room conditions corrected with the effect of temperature, the Raman spectra of a UO_2 disk in the presence of air at 573 K were analysed as a function of time. The results of this analysis showed a continuous oxidation during the first two hours, before the U_4O_9 phase was almost completely stabilised.

3.2.5. Acknowledgements

This work was supported by ENRESA within the project Nº 079000189, entitled “Aplicación de técnicas de caracterización en el estudio de la estabilidad del combustible nuclear irradiado en condiciones de almacenamiento” (ACESCO).

3.2.6. References

[1] C. Ferry, C. Poinssot, C. Cappelaere, L. Desgranges, C. Jégou, F. Miserque, J. P. Piron, D. Roudil and J. M. Gras, *J. Nucl. Mater.*, **352**, 246-253 (2006).
[2] R. J. McEachern and P. Taylor, *J. Nucl. Mater.*, **254**, 87-121 (1998).
[3] B. T. M. Willis, *Proc. Br. Ceram. Soc.*, **1**, 9-19 (1964).
[4] B. T. M. Willis, *Nature*, **197**, 755-756 (1963).
[5] H. Hering and P. Pério, *Bull Soc. Quim.*, **M. 531** (1952).
[6] P. Jolibois, *C. R. Acad. Sci.*, **224**, 1395-1396 (1947).
[7] H. He and D. Shoesmith, *Phys. Chem. Chem. Phys.*, **12**, 8108-8117 (2010).
[8] L. Desgranges, G. Baldinozzi, P. Simon, G. Guimbretière and A. Canizares, *J. Raman Spectrosc.*, **43**, 455-458 (2012).
[9] G. C. Allen, I. S. Butler and N. A. Tuan, *J. Nucl. Mater.*, **144**, 17-19 (1987).
[10] M. L. Palacios and S. H. Taylor, *Appl. Spectrosc.*, **54**, 1372-1378 (2000).
[11] E. A. Stefaniak, A. Alsecz, I. E. Sajó, A. Worobiec, Z. Máthé, S. Török and R. Van Grieken, *J. Nucl. Mater.*, **381**, 278-283 (2008).
[12] F. Pointurier and O. Marie, *Spectrochim. Acta B*, **65**, 797-804 (2010).
[13] D. Manara and B. Renker, *J. Nucl. Mater.*, **321**, 233-237 (2003).
[14] L. Jun-bo, L. Gan and G. Shu-lan, *Spectrosc. Spect. Anal.*, **34 (2)**, 405-409 (2014).
[15] L. J. Bonales, J. M. Elorrieta, A. Lobato and J. Cobos, *Raman Spectroscopy, a Useful Tool to Study Nuclear Materials*, Applications of Molecular Spectroscopy to Current Research in the Chemical and Biological Sciences, Dr. Mark Stauffer (Ed.), InTech (2016). ISBN 978-953-51-2681-2.
[16] J. M. Elorrieta, L. J. Bonales, N. Rodríguez-Villagra, V. G. Baonza and J. Cobos, *Phys. Chem. Chem. Phys.*, **18**, 28209-28216 (2016).
[17] P. G. Marlow, J. P. Russell and J. R. Hardy, *Philos. Mag.*, **14**, 409-410 (1966).
[18] T. Livneh and E. Sterer, *Phys. Rev. B*, **73**, 085118-085119 (2006).

[19] G. Rousseau, L. Desgranges, F. Charlot, N. Millot, J. C. Nièpce, M. Pijolat, F. Valdivieso, G. Baldinozzi and J. F. Berar, *J. Nucl. Mater.*, **355**, 10-20 (2006).
[20] G. Talsky, *Derivative Spectrophotometry: Low and High Order*, Verlagsgesellschaft, Weinheim (Federal Republic of Germany) and Inc., New York, NY (USA) (1994). ISBN 3-527-28294-7.

Result 3

Development of the Raman laser heating method. Application to UO_2

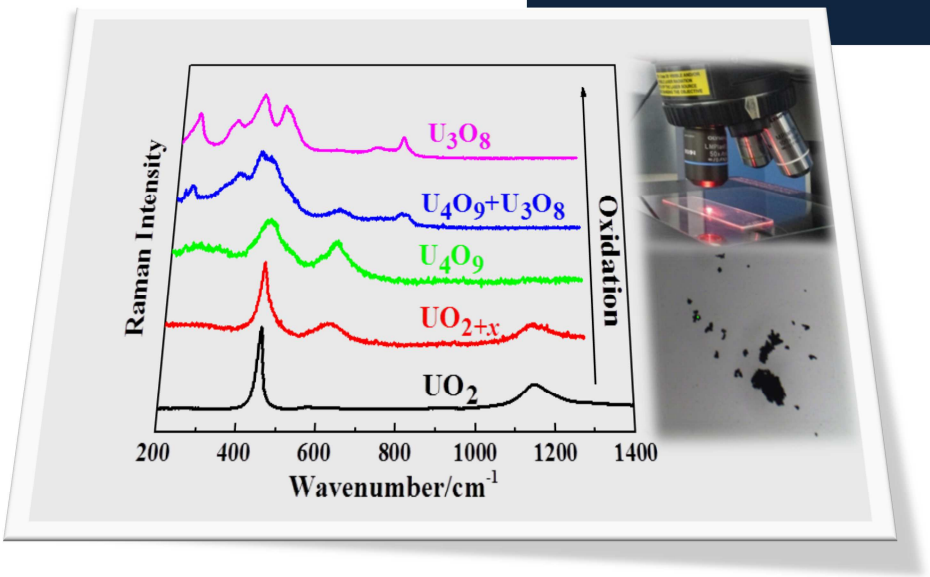

Published as "Laser-induced oxidation of UO_2: A Raman study", **J. M. Elorrieta, L. J. Bonales, M. Naji, D. Manara, V. G. Baonza and J. Cobos**, *J. Raman Spectrosc.*, 1-7 (2018).
DOI: 10.1002/jrs.5347
Supplementary Information: jrs5347-sup-0001-Supplementary_Material.zip

Abstract

A reliable method to probe and characterise the oxidation of actinide oxides by means of Raman spectroscopy is introduced. The present so-called Raman laser heating method enables studying the behaviour of various compounds at high temperatures and under a given atmosphere with the unique alteration of a small amount of sample, which is certainly advantageous in terms of safety when handling hazardous or radioactive materials. The approach is based on a dual use of the laser beam, which is at the same time employed as excitation source for the Raman analysis and as heating source, by exploiting the possibility to vary the beam power density reaching the sample surface. A high laser power density can lead to a significant increase of the analyte surface temperature by up to several hundred of degrees. A sufficiently low power density allows us to subsequently acquire the corresponding Raman spectrum at the same point without distorting the measurement. In this work, UO_2 powder has been subjected to Raman laser heating in air as a proof of this method's applicability, attaining a sequential acquisition of the characteristic Raman spectra of the different oxides involved in the oxidation from UO_2 to U_3O_8. The temperature at which such sequence of phase transformations started to occur was estimated to be around (560 ± 40) K. The temperature at the sample surface was estimated from the Stokes/anti-Stokes intensities ratio, using a similar set-up to that used in the Raman laser heating experiments. These results are particularly appealing in remote analyses, like those required in the study of nuclear fuel and nuclear waste.

3.3.1. Introduction

Knowledge of the structure and reactivity of actinide oxides, AnO_2, is required for designing safe storages for spent nuclear fuel (SNF). Different efforts have been performed in this regard, studying the stability of the SNF under repository conditions or assessing its behaviour under possible accident scenarios [1-4]. From these studies, it is well-known that the oxidation of UO_2 (SNF matrix) and other actinides present in the SNF (Np, Pu, Am, etc.) will influence the overall stability of the spent fuel pellets.

Oxidation of AnO_2 occurs via oxygen incorporation into the fluorite structure (fcc) of the stoichiometric oxide, which has alternating empty and occupied oxygen cubic sites. These vacancies facilitate oxidation, *e.g.* uranium dioxide can oxidise to UO_{2+x}, ($x < 0.25$) maintaining the fcc structure [5,6]. Further oxidation to higher oxidation states (V and VI) is also possible for uranium, leading to different structures such as the tetragonal or orthorhombic structures found for U_3O_7 and U_3O_8, respectively [7].

Although oxidation of AnO_2 has been broadly studied for some actinides, such as U and Pu, some aspects of their structure and reactivity are still under debate. For instance, the exact hyperstoichiometry limits of UO_{2+x} in equilibrium with air, or the reactivity of allegedly hypervalent PuO_{2+x} (with additional atoms within the host lattice) [8-12]. Therefore, additional studies are necessary in this regard, but the intense radiation field inherently associated with these materials makes it difficult to study them in safe conditions.

Raman spectroscopy is an analytical tool that has been established in recent years as a reliable probe for this kind of studies, as confirmed by the large increase in the specialised literature [13-29]. This is due to some of its features, as that 1) it does not require any special preparation of the sample, 2) the technique allows the analysis of a very small amount of sample, 3) it requires no direct contact between the experimental set-up and the analyte, 4) it can be easily implemented (remote analysis, Raman probes, handheld systems, etc.) for different applications, and 5) controlling the excitation laser power density, it is a non-destructive technique.

The effects of the laser power density provided during a Raman measurement and its associated heating have been studied in detail on semi-conducting and insulating materials [30-32], especially those showing a good absorption in the visible range. Actinide dioxides, and precisely UO_2, being a good absorber in the range of 1.9–2.5 eV [33], belong to materials where care needs to be taken when conducting Raman experiments. Owing to AnO_2 absorption profiles, the local spot temperature may increase by hundreds of degrees. This causes several changes in the Raman modes and, sometimes, the sample alteration as a result of effects such as oxidation, photo-reduction, order-disorder transition, phase transition or decomposition.

Despite the fact that this heating action of the laser has been traditionally considered an inconvenience when it comes to perform Raman measurements, as the power is usually optimised to avoid sample alteration, some authors have

taken advantage of this feature for various purposes. On the one hand, detailed Raman studies have recently been performed on PuO_2, NpO_2 and AmO_2, aimed primarily at the complete mode assignment of the observed Raman bands [18,24,25,27]. In order to solve some discrepancies in the reported nature of peaks and their origin, a study of the evolution of their spectra as a function of laser power density has been carried out. It has been shown that increasing the laser power density enhances the anharmonic behaviour of the T_{2g} mode in NpO_2 and PuO_2 [25,27], decoupling of the (Γ_8, *LO*–*TO*) bound state in NpO_2 [25] and, finally, depopulation of $\Gamma_1 \rightarrow \Gamma_5$ and $\Gamma_1 \rightarrow \Gamma_3$ electronic crystal field excitations in PuO_2 [27]. However, no phase alteration has been detected in these materials, even at temperatures above 700 K. On the contrary, in AmO_2 it has been observed that, even at very low power density, the laser may induce an unavoidable photolysis process when visible lasers are used, resulting in the formation of hyperstoichiometric americium sesquioxide Am_2O_{3+z} [24].

On the other hand, laser heating has been employed for analysing the oxidation behaviour and/or resistance of uranium-based materials such as (U, Pu)O_2 [14,28], (U, La)O_2 [23], and even spent fuels [22]. In these studies, oxidation of the samples to higher oxidation-state phases has been observed by Raman spectroscopy, using the laser as a heat source.

Due to the feasibility of this laser-induced heating, the associated temperature estimation has become an attractive target. In a recent study, Naji *et al.* [27] verified that the analysis of the Stokes/anti-Stokes intensities ratio is a reliable method for the temperature estimation in this type of experiments. Thus, in this work we present a new *in situ* approach based on the simultaneous application of the laser-induced heating to gradually oxidise UO_2, and the corresponding temperature estimation by the Stokes/anti-Stokes analysis. The attained sequential oxidation under the laser beam, which has been for the first time systematically studied, is in good agreement with previously reported observations on UO_2 oxidation. The estimated temperature also seems to be consistent with existing literature data.

This paper has been organised as follows. The “Materials and methods” section describes the employed materials, the equipment, and the Raman laser heating method in detail. In the “Results and discussion” section, oxidation of UO_2 is shown as an example of the applicability of this method and, in addition, the Stokes/anti-Stokes spectral analysis is carried out in order to estimate the temperature at which phase transformations start to occur.

3.3.2. Materials and methods

3.3.2.1. Materials

UO_2 powder with a particle size distribution of ~15 µm, measured by dynamic light scattering (DLS), was annealed at 800ºC during 24 hr under reducing conditions (N_2:H_2 4:96 v/v) in order to ensure stoichiometric $UO_{2.00}$ was attained. Initial characterisation carried out on this powder is further described in the "Sample pre-characterisation" section.

3.3.2.2. Pre-characterisation techniques

Thermogravimetric experiments were conducted with a Q50 thermo-balance (TA Instruments, Spain) in synthetic air with a constant rate of 60 mL/min from room temperature up to 973 K, at a 10 K/min rate.

X-ray diffraction (XRD) characterisation was performed by means of a Philips PANalytical X'Pert MPD diffractometer using Cu K_α radiation (λ=1.54056 Å) and operating at 45 kV and 40 mA. Bragg-Brentano configuration geometry was used.

For the acquisition of scanning electron microscopy (SEM) images of the initial sample, a SU6600 (HITACHI) microscope was employed. Its ZrO/W electron cannon permits working with an accelerating voltage that covers from 0.5 to 30kV and with a magnification range from 10x up to 600000x.

3.3.2.3. Raman spectrometers

Raman spectroscopy analyses were mainly carried out at CIEMAT facilities (www.ciemat.es) using a Horiba LabRAM HR Evolution spectrometer (Jobin-Yvon Technology). A red laser of He-Ne with a wavelength of 632.8 nm (1.96 eV) and a nominal power of 20 mW (adjustable by filters) was used as the excitation source. The laser was focused onto the sample surface using a 100x objective (NA (*Numerical Aperture*) = 0.9) which led to a laser spot diameter below 0.9 µm; the scattered light was then collected with the same objective, dispersed with a 600 grooves/mm grating, and finally detected with a Peltier-cooled CCD detector (256 x 1024 pixels).

Stokes/anti-Stokes Raman spectra were acquired using the Raman facility available at the European Commission's Joint Research Centre of Karlsruhe (https://ec.europa.eu/jrc/en/about/jrc-site/karlsruhe). It consists in a Jobin-Yvon T64000 spectrometer equipped with an 1800 grooves/mm grating and a low noise liquid nitrogen cooled Symphony CCD detector. The spectrometer was used in the triple stage mode, which permits access to both Stokes and anti-Stokes spectrum lines while blocking the elastic Rayleigh line. The excitation source used in this case was the 647 nm (1.91 eV) line of a Kr^+ laser with a controllable nominal power up to 0.5 W. The laser was focused using a 50x long focal objective (NA = 0.5) which led to a laser spot diameter below 12.2 μm, and the power density impinging on the sample surface was measured by a Coherent® power-meter placed at a position corresponding to the sample surface.

3.3.2.4. Raman laser heating

Lasers can induce a local temperature increase, by up to several hundreds of degrees, if they are focused on a small spot. Therefore, the excitation source of the Raman spectrometer focused on UO_2 powder can increase its temperature and thereby, subjecting it to laser heating in air, it is possible to produce the conditions under which oxidation of this material takes place, *i.e.* O_2 (g) and high temperature. In practice, the method consists in first heating a selected particle of UO_2 by applying the excitation laser at high power density, thus inducing oxidation. Actually, a sequential oxidation can be attained setting the appropriate parameters: the laser power density at the sample surface, and the heating time or spectrum acquisition (as if we were in the course of a Raman experiment). After each heating step, the spectrum corresponding to the obtained oxide can be subsequently acquired at low power density, enabling the characterisation of the UO_2 phase transitions and the oxidation evolution.

3.3.3. Results and discussion

3.3.3.1. Sample pre-characterisation

UO_2 powder was analysed previous to the laser heating experiments by a variety of characterisation techniques: scanning electron microscopy, X-ray diffraction, Raman spectroscopy, and thermogravimetric analysis (see Figure 3.3.S1 (Supporting Information)). The results obtained from this pre-characterisation confirmed the quasistoichiometry of the initial UO_2 sample.

3.3.3.2. Sequential oxidation by laser

First of all, in order to check that a sequential oxidation of UO_2 was actually feasible with the Raman set-up available at CIEMAT, several combinations of laser power densities and exposure times were performed. In this way, varying both parameters consecutively until a significant change in the spectrum was detected, an *in situ* sequential oxidation of a UO_2 particle was attained. Figure 3.3.1 gathers some of the Raman spectra acquired during this oxidation reaction.

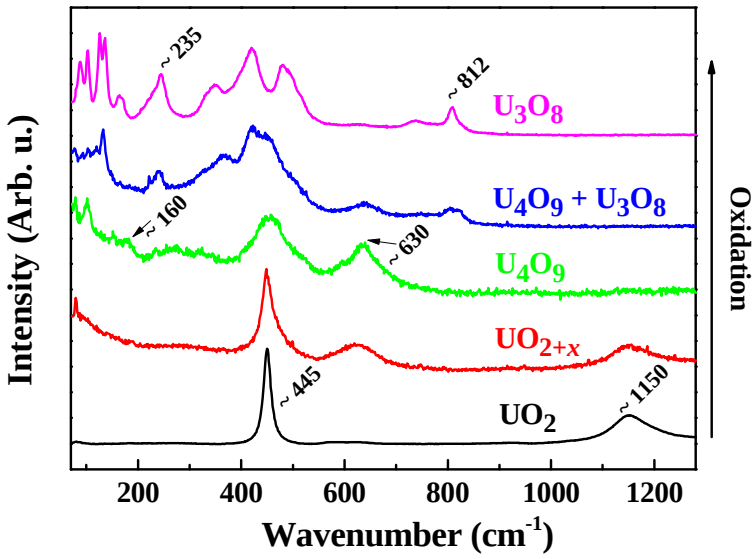

Fig. 3.3.1. Raman spectroscopy *in situ* characterisation (using a 632.8 nm laser and 300 s acquisition time) of the sequential oxidation of a UO_2 particle, where the position of the main characteristic bands of the different stoichiometric oxides is shown.

The bottom spectrum in Figure 3.3.1 corresponds to the initial quasistoichiometric UO_2 (see Supplementary Information for further detail), featuring the T_{2g} band around 445 cm^{-1} and the 2LO mode band at ~1150 cm^{-1} [34,35]. Once oxidation started and additional oxygen was incorporated into the cubic structure of UO_2 (UO_{2+x}), a broad band appeared at 500-700 cm^{-1}. This contribution is commonly attributed to different structure defects [13,16,26,36]. As progressive oxidation occurred, the latter feature grew and the band at 1150 cm^{-1} decreased [13,26,37], even disappearing when U_4O_9 was reached [17], as can be observed in Figure 3.3.1. At this point, a new band appeared at ~160 cm^{-1}, which is also characteristic of the U_4O_9 phase [17]. Further oxidation produced a

marked change in the spectrum: the band at 445 cm^{-1} began to split, the band at 500-700 cm^{-1} decreased and two new bands at ~235 cm^{-1} and ~812 cm^{-1} appeared. This was possibly due to the increasing presence of orthorhombic U_3O_8. Finally, three bands in the range of 300-500 cm^{-1} and the ~235 cm^{-1} and ~812 cm^{-1} features indicated that a complete conversion to U_3O_8 had been accomplished [15,38-41].

Thereafter, the appropriate laser power density and time parameters for the direct attainment of the two phase transformations ($UO_2 \rightarrow U_4O_9 \rightarrow U_3O_8$) were tested. Figure 3.3.2 reflects the results of this Raman laser heating experiment, applied again to a UO_2 particle.

Reproducibility of this Raman laser heating protocol for UO_2 was ensured by heating different particles of similar sizes. The good reproducibility obtained between different measurements allows us to estimate the temperature conditions under which $UO_2 \rightarrow U_4O_9 \rightarrow U_3O_8$ phase transitions take place as a result of the laser-induced heating. It should be noted that this temperature value is strongly dependent on the roughness/grain size of the sample. Thus, the temperature at which these transitions occur can be better inferred by establishing a direct relation between the laser power density and the laser-induced temperature, by performing the Stokes/anti-Stokes analysis as hereafter described.

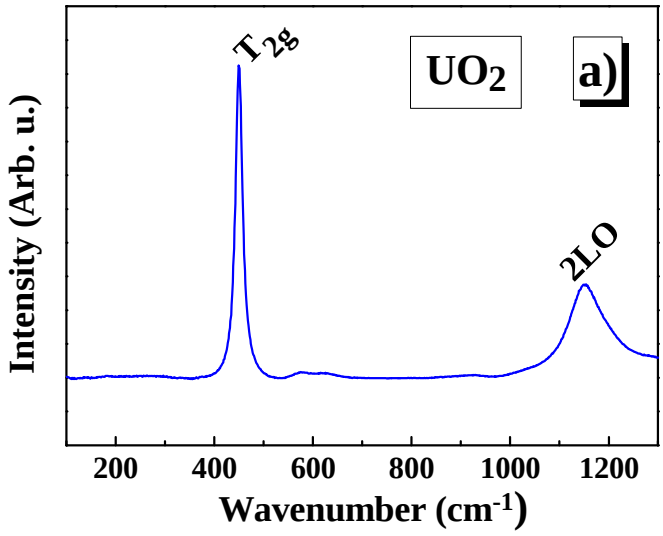

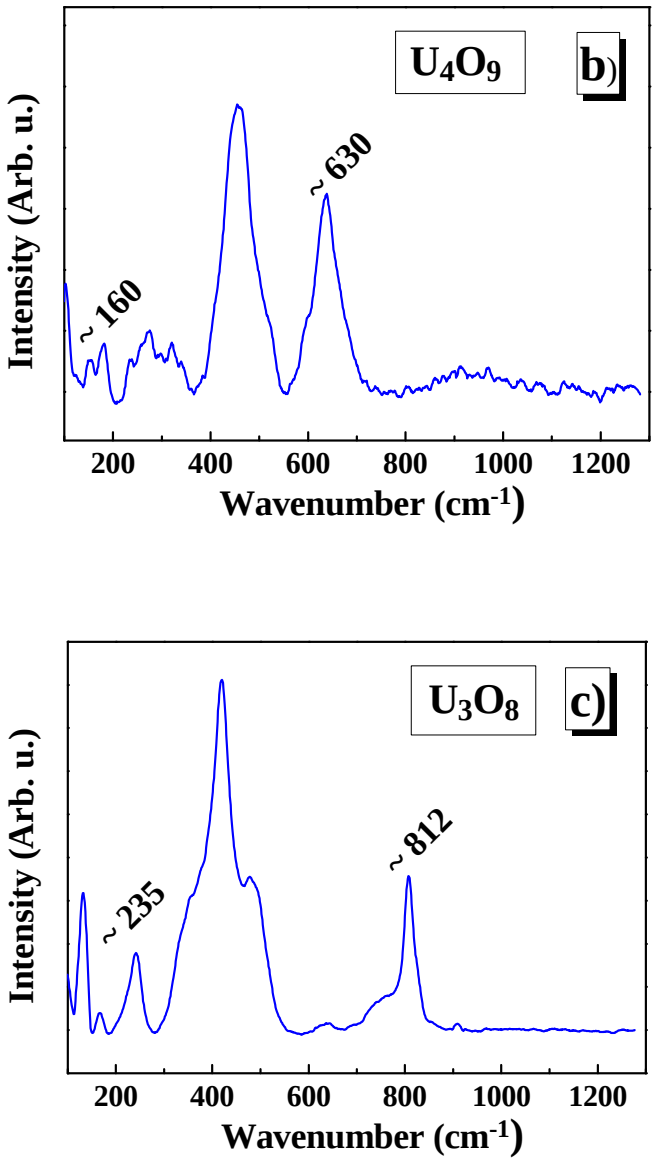

Fig. 3.3.2. Raman spectra (using a 632.8 nm laser and 300 s acquisition time) corresponding to UO_2 laser heating *in situ* oxidation: a) at the start of the experiment, b) after heating the particle during 5 s, where U_4O_9 was detected, and c) after using the same laser power density as in b) during 10 s, where complete oxidation of the particle to U_3O_8 was observed.

3.3.3.3. Stokes/anti-Stokes temperature analysis

The temperature of the laser-heated sample surface at which the transformations started to occur was estimated by evaluating the ratio between the T_{2g} Stokes and anti-Stokes Raman intensities and using the following equation (Equation 3.3.1), based on the Boltzmann distribution of modes between energy levels,

$$\frac{I_{anti-Stokes}}{I_{Stokes}} = \left(\frac{\nu_0+\nu_j}{\nu_0-\nu_j}\right)^4 e^{-\frac{hc\nu_j}{k_B T}} \qquad \text{(Eq. 3.3.1)}$$

where ν_0 and ν_j are the wavenumbers of the excitation line and the Raman modes, respectively, $I_{anti\text{-}Stokes}$ and I_{Stokes} are the intensities of the anti-Stokes and Stokes Raman peaks, k_B is the Boltzmann constant, c is the speed of light, h is Planck's constant, and T is temperature. The estimated uncertainty was obtained by applying the method previously published by LaPlant *et al*. [42]. This method was shown to give satisfactory results as compared by Naji *et al.* [27] for a PuO_2 sample which was externally heated in a Linkam TS1500 temperature stage.

The Raman anti-Stokes spectrum, however, can only be measured with a spectrometer equipped with a triple-mode optical path or any other system for which the use of high-pass filters is not required. Since these conditions are not met with the current Raman equipment at CIEMAT, the latter experiments were performed using the Raman facility available at the European Commission's Joint Research Centre of Karlsruhe (Germany).

Thus, the absolute Stokes/anti-Stokes temperature (T_{SAS}) was derived from the ratio (R_{SAS}) between the experimental integrated intensities of the anti-Stokes and Stokes T_{2g} peaks. It should be pointed out that the T_{SAS} determination based on the T_{2g} peak intensity can only be rigorously performed as far as the original fluorite structure and T_{2g} mode features are maintained. Prior to these calculations, Stokes and anti-Stokes Raman spectra were corrected for the instrumental response according to the procedure described elsewhere [27,32]. Despite the instrumental correction, the value of T_{SAS} can represent the real sample temperature in a rather inaccurate fashion, due to uncontrollable sample-dependent factors affecting the intensities of the Stokes and anti-Stokes lines, such as defect or impurity fluorescence, roughness scattering, etc. Therefore, the value of T_{SAS} should be considered as only indicative of the absolute temperature produced by the laser beam on the irradiated spot. In addition, although it is not the case, it should be noted that for this kind of analysis two important precautions need to be always

taken into account with regard to the wavelength used: the assurance of no Raman resonance effects and the knowledge of the absorption behaviour of the material in that corresponding energy range.

Raman spectra on UO_2 powder were measured in this case using the 647 nm line of a Kr^+ laser. Longer acquisition times (several tens of seconds) were however needed in order to resolve the anti-Stokes spectrum with the triple-mode optical path. The resulting Raman spectra measured at different laser power density levels and the corresponding SAS temperatures are reported in Figure 3.3.3a and Figure 3.3.3b, respectively. The power density levels reflected in Figure 3.3.3 were measured at the exit of the laser cavity. The laser power density impinging on the sample surface was measured to be lower by a factor 5 approximately.

The spectra measured correspond to defective fcc UO_2, showing a broad feature between 550 cm^{-1} and 630 cm^{-1} characteristic of UO_{2+x} [13,16,26,36]. This feature is observed up to ~68 mW/cm^2. Around this laser power density defect modes quickly disappear, and then U_3O_8 spectrum [15,38-41] is observed for higher laser power densities (see Figure 3.3.3a). Due to the longer acquisition times needed, the sequential oxidation of UO_2 to U_4O_9 before final stabilisation of U_3O_8 was not observed in these experiments. Nonetheless, the main goal of these tests consisted in showing that the temperature at which the UO_2 fluorite structure loses its chemical stability in air can be effectively determined by Raman spectroscopy without the help of any other auxiliary techniques. Indeed, the Stokes/anti-Stokes analysis does give an approximate temperature at which the phase transformations observed with the CIEMAT equipment start to take place in the time frame of the current Raman laser heating experiment. Actually, such temperature is close to (560 ± 40) K ((290 ± 40) °C) if we take into account the highest temperature measured before U_3O_8 was detected, in fair agreement with existing literature data [2].

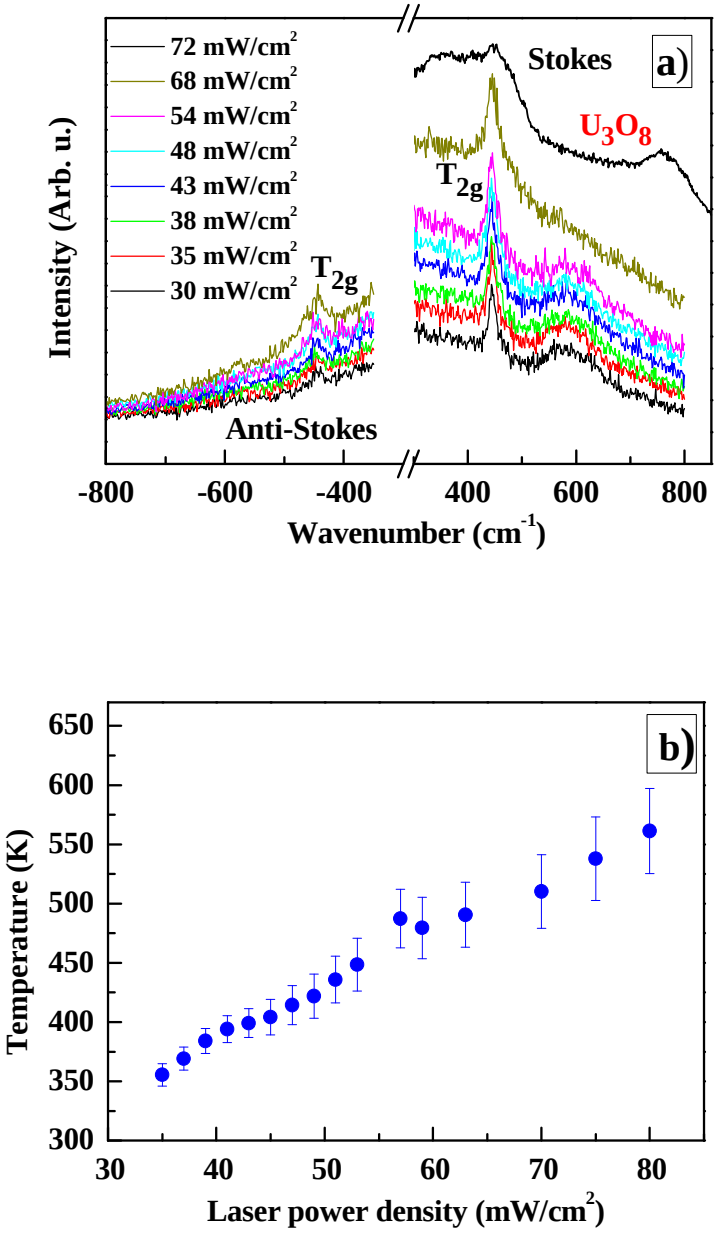

Fig. 3.3.3. a) Selection of Stokes and anti-Stokes Raman spectra (16 min acquisition/heating time) of UO_2 powder measured at JRC Karlsruhe with increasing power density levels of a 647 nm laser. b) Stokes/anti-Stokes temperatures (T_{SAS}), estimated from the spectra acquired at different laser power densities.

3.3.4. Conclusions

The development of a reliable method to characterise *in situ* by means of Raman spectroscopy the chemical reactions occurring in a sample, called Raman laser heating, has been carried out. The method consists of two steps: 1) producing a local heating on the investigated material by increasing the laser power density, and 2) subsequently acquiring, at a non-altering low laser power density, the corresponding Raman spectrum of the sample in order to analyse its reactivity at the high temperatures induced and under a given atmosphere.

In this work, Raman laser heating is especially proposed to evaluate *in situ* the oxidation of actinide dioxides in air. The small size of the laser spot enables analysing such oxidation behaviour with the unique alteration of a minor amount of sample, what constitutes a significant safety advantage when it comes to working with homogeneous radioactive materials.

In order to prove the method's applicability, UO_2 powder has been subjected to Raman laser heating, consequently acquiring different Raman spectra corresponding to the sequential oxides (UO_{2+x} and U_4O_9) involved in the air oxidation of UO_2 to U_3O_8, with good reproducibility of the results.

The temperature at which such phase transformations start to occur, in the time frame of the current laser heating experiments, was estimated to be close to (560 ± 40) K ((290 ± 40) °C) in air by performing, with a different set-up, a Stokes/anti-Stokes spectral analysis in similar Raman laser heating experiments. This is an important result as it shows how it is indeed possible, using only Raman spectroscopy, to reasonably estimate the temperature at which UO_2 starts to oxidise in air.

The present observations will be useful in the analysis of nuclear fuel and nuclear waste, which can be performed remotely by tailored Raman probes, and, at the same time, *in situ* or *ex situ* on highly radioactive samples.

3.3.5. Acknowledgements

This work was supported by ENRESA within the project Nº 079000189, entitled “Aplicación de técnicas de caracterización en el estudio de la estabilidad del combustible nuclear irradiado en condiciones de almacenamiento” (ACESCO).

The Authors are indebted to J.-Y. Colle (JRC Karlsruhe) for his help in the measurement of anti-Stokes Raman spectra and to R.J.M. Konings (JRC Karlsruhe) for his scientific advice.

3.3.6. References

[1] C. Ferry, C. Poinssot, C. Cappelaere, L. Desgranges, C. Jégou, F. Miserque, J. P. Piron, D. Roudil and J. M. Gras, *J. Nucl. Mater.*, **352**, 246-253 (2006).
[2] R. J. McEachern and P. Taylor, *J. Nucl. Mater.*, **254**, 87-121 (1998).
[3] D. G. Boase and T. T. Vandergraaf, *Nucl. Technol.*, **32**, 60-71 (1977).
[4] R. E. Einziger, L. E. Thomas, H. C. Buchanan and R. B. Stout, *J. Nucl. Mater.*, **190**, 53-60 (1992).
[5] B. T. M. Willis, *Nature*, **197**, 755-756 (1963).
[6] H. Hering and P. Pério, *Bull Soc. Quim.*, **M. 531** (1952).
[7] P. Jolibois, *C. R. Acad. Sci.*, **224**, 1395-1396 (1947).
[8] B. E. Schaner, *J. Nucl. Mater.*, **2**, 110-120 (1960).
[9] H. R. Hoekstra, A. Santoro and S. Siegel, *J. Inorg. Nucl. Chem.*, **18**, 166-178 (1961).
[10] S. D. Conradson, B. D. Begg, D. L. Clark, C. Den Auwer, M. Ding, P. K. Dorhout, F. J. Espinosa-Faller, P. L. Gordon, R. G. Haire, N. J. Hess, R. F. Hess, D. W. Keogh, G. H. Lander, D. Manara, L. A. Morales, M. P. Neu, P. Paviet-Hartmann, J. Rebizant, V. V. Rondinella, W. Runde, C. D. Tait, D. K. Veirs, P. M. Villella and F. Wastin, *J. Solid State Chem.*, **178**, 521-535 (2005).
[11] P. Martin, S. Grandjean, M. Ripert, M. Freyss, P. Blanc and T. Petit, *J. Nucl. Mater.*, **320**, 138-141 (2003).
[12] J. M. Haschke, T. H. Allen and L. A. Morales, *Science*, **287**, 285 (2000).
[13] H. He and D. Shoesmith, *Phys. Chem. Chem. Phys.*, **12**, 8108-8117 (2010).
[14] C. Jégou, R. Caraballo, S. Peuget, D. Roudil, L. Desgranges and M. Magnin, *J. Nucl. Mater.*, **405**, 235-243 (2010).
[15] F. Pointurier and O. Marie, *Spectrochim. Acta B*, **65**, 797-804 (2010).

[16] G. Guimbretière, L. Desgranges, A. Canizares, G. Carlot, R. Caraballo, C. Jégou, F. Duval, N. Raimboux, M. R. Ammar and P. Simon, *Appl. Phys. Lett.*, **100**, 251914 (2012).
[17] L. Desgranges, G. Baldinozzi, P. Simon, G. Guimbretière and A. Canizares, *J. Raman Spectrosc.*, **43**, 455-458 (2012).
[18] M. J. Sarsfield, R. J. Taylor, C. Puxley and H. M. Steele, *J. Nucl. Mater.*, **427**, 333-342 (2012).
[19] F. Lebreton, D. Horlait, R. Caraballo, P. M. Martin, A. C. Scheinost, A. Rossberg, C. Jégou and T. Delahaye, *Inorg. Chem.*, **54 (20)**, 9749-60 (2015).
[20] M. Chollet, D. Prieur, R. Böhler, R. Belin and D. Manara, *J. Chem. Thermodyn.*, **89**, 27-34 (2015).
[21] G. Guimbretière, A. Canizares, N. Raimboux, J. Joseph, P. Desgardin, L. Desgranges, C. Jégou and P. Simon, *J. Raman Spectrosc.*, **46**, 353-420 (2015).
[22] C. Jégou, M. Gennisson, S. Peuget, L. Desgranges, G. Guimbretière, M. Magnin, Z. Talip and P. Simon, *J. Nucl. Mater.*, **458**, 343-349 (2015).
[23] Z. Talip, T. Wiss, P. E. Raison, J. Paillier, D. Manara, J. Somers and R. J. M. Konings, *J. Am. Ceram. Soc.*, **98**, 2278-2285 (2015).
[24] M. Naji, J.-Y. Colle, O. Benes, M. Sierig, J. Rautio, P. Lajarge and D. Manara, *J. Raman Spectrosc.*, **46**, 750-756 (2015).
[25] M. Naji, N. Magnani, J. Y. Colle, O. Beneš, S. Stohr, R. Caciuffo, R. J. M. Konings, and D. Manara, *J. Phys. Chem. C*, **120**, 4799 (2016).
[26] J. M. Elorrieta, L. J. Bonales, N. Rodríguez-Villagra, V. G. Baonza and J. Cobos, *Phys. Chem. Chem. Phys.*, **18**, 28209-28216 (2016).
[27] M. Naji, N. Magnani, L. J. Bonales, S. Mastromarino, J.-Y. Colle, J. Cobos and D. Manara, *Phys. Rev. B*, **95**, 104307 (2017).
[28] Z. Talip, S. Peuget, M. Magnin, L. Berardo, C. Valot, R. Vauchy and C. Jégou, *J. Raman Spectrosc.*, **48 (5)**, 765-772 (2017).
[29] J. M. Elorrieta, D. Manara, L. J. Bonales, J. F. Vigier, O. Dieste, M. Naji, R. C. Belin, V. G. Baonza, R. J. M. Konings and J. Cobos, *J. Nucl. Mater.*, **495**, 484-491 (2017).
[30] S. Piscanec, M. Cantoro, A. C. Ferrari, J. A. Zapien, Y. Lifshitz, S. T. Lee, S. Hofmann and J. Robertson, *Phys. Rev. B*, **68**, 241312 (2003).
[31] L. Han, M. Zeman and A. H. M. Smets, *Nanoscale*, **7**, 8389-8397 (2015).
[32] M. Naji, F. Di Lemma, A. Kovács, O. Beneš, D. Manara, J. Y. Colle, G. Pagliosa, P. Raison, and R. J. M. Konings, *J. Raman Spectrosc.*, **46**, 661-668 (2015).
[33] J. Schoenes, *J. App. Phys.*, **49**, 1463-1465 (1978).

[34] P. G. Marlow, J. P. Russell and J. R. Hardy, *Philos. Mag.*, **14**, 409-410 (1966).
[35] T. Livneh and E. Sterer, *Phys. Rev. B*, **73**, 085118-085119 (2006).
[36] P. R. Graves, *Appl. Spectrosc.*, **144**, 1665-1667 (1990).
[37] D. Manara and B. Renker, *J. Nucl. Mater.*, **321**, 233-237 (2003).
[38] G. C. Allen, I. S. Butler and N. A. Tuan, *J. Nucl. Mater.*, **144**, 17-19 (1987).
[39] I. S. Butler, G. C. Allen and N. A. Tuan, *Appl. Spectrosc.*, **42 (5)**, 901-902 (1988).
[40] M. L. Palacios and S. H. Taylor, *Appl. Spectrosc.*, **54**, 1372-1378 (2000).
[41] E. A. Stefaniak, A. Alsecz, I. E. Sajó, A. Worobiec, Z. Máthé, S. Török and R. Van Grieken, *J. Nucl. Mater.*, **381**, 278-283 (2008).
[42] F. LaPlant, G. Laurence and D. Ben-Amotz, *Appl. Spectrosc.*, **50**, 1034-1038 (1996).

Supplementary Information

3.3.S1. UO_2 sample pre-characterisation

SEM images of the UO_2 powder are shown in the upper part of Figure 3.3.S1. As can be observed, the powder is formed by fine pulverised material with a particle size distribution of around 10–15 µm.

Figure 3.3.S1a shows the typical X-ray diffraction pattern of the cubic structure of quasi-stoichiometric UO_2 over the 2θ angle range 25–80º, in agreement with data published by Fritsche *et al.* (open symbols ICCD 00-041-1422) [1]. Assuming the *Fm-3m* space group for UO_2, the cell parameter found is 0.5468(5) nm, also in accordance with those values reported in the literature [2,3].

The Raman spectrum (Figure 3.3.S1b) of this initial powder corresponds as well to the characteristic spectrum of stoichiometric UO_2, *i.e.* it features a sharp band around 445 cm^{-1} assigned to the U-O fundamental stretching vibration (T_{2g}), and a wider and much less intense band at ~1150 cm^{-1} attributed to the 2LO phonon band [4,5]. Less intense spectral features between 550 cm^{-1} and 630 cm^{-1} reveal a small concentration of negligible defects in the fcc crystal structure [6,9].

In addition, the thermogravimetric weight-gain curve obtained (Figure 3.3.S1c) represents the typical curve for UO_2 oxidation, where the first *plateau* corresponds to its transformation into U_4O_9/U_3O_7 and the final one indicates the whole conversion to U_3O_8 [10]. The total weight gain recorded by thermogravimetric analysis, close to 4%, also confirms the quasi-stoichiometry of the initial UO_2 powder.

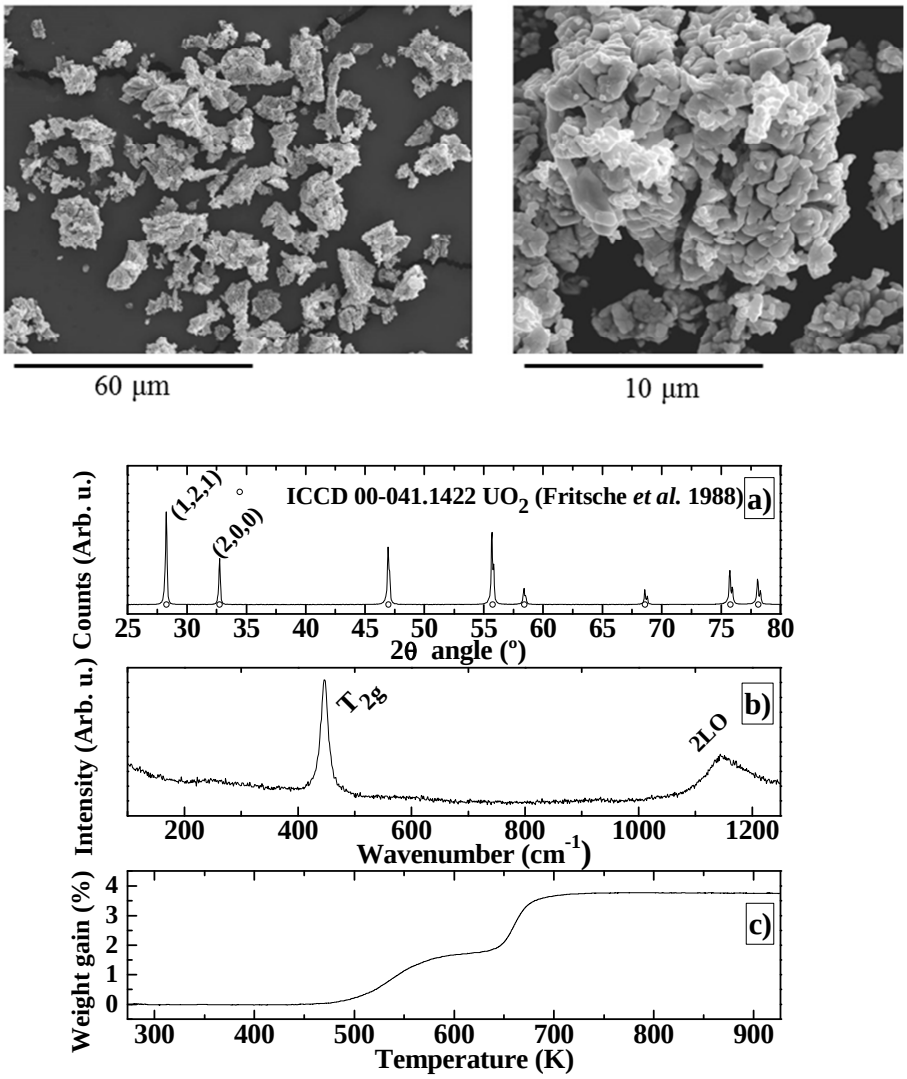

Fig. 3.3.S1. SEM images of UO_2 powder (top). Graphics corresponding to the previous characterisation of the UO_2 sample: a) X-ray powder diffraction pattern, b) Raman spectrum (using a 632.8 nm laser and 300 s acquisition time), and c) Thermogravimetric curve (bottom).

3.3.S2. References

[1] R. Fritsche, Sussieck-Fornefeld C. Min.-Petr. Inst., Univ. Heidelberg, Germany, ICDD Grant-in-Aid (1988).
[2] F. Grønvold, *J. Inorg. Nucl. Chem.*, **1**, 357-370 (1955).
[3] L. Lynds, W. A. Young, J. S. Mohl and G. G. Libowitz, *Adv. Chem.*, **39**, 58-65 (1962).
[4] P. G. Marlow, J. P. Russell and J. R. Hardy, *Philos. Mag.*, **14**, 409-410 (1966).
[5] T. Livneh and E. Sterer, *Phys. Rev. B*, **73**, 085118-085119 (2006).
[6] H. He and D. Shoesmith, *Phys. Chem. Chem. Phys.*, **12**, 8108-8117 (2010).
[7] G. Guimbretière, L. Desgranges, A. Canizares, G. Carlot, R. Caraballo, C. Jégou, F. Duval, N. Raimboux, M. R. Ammara and P. Simon, *Appl. Phys. Lett.*, **100**, 251914 (2012).
[8] J. M. Elorrieta, L. J. Bonales, N. Rodríguez-Villagra, V. G. Baonza and J. Cobos, *Phys. Chem. Chem. Phys.*, **18**, 28209-28216 (2016).
[9] P. R. Graves, *Appl. Spectrosc.*, **144**, 1665-1667 (1990).
[10] S. Aronson, R. B. Roof and J. Belle, *J. Chem. Phys.*, **27**, 137-144 (1957).

Result 4

Temperature dependence of the Raman spectrum of UO_2

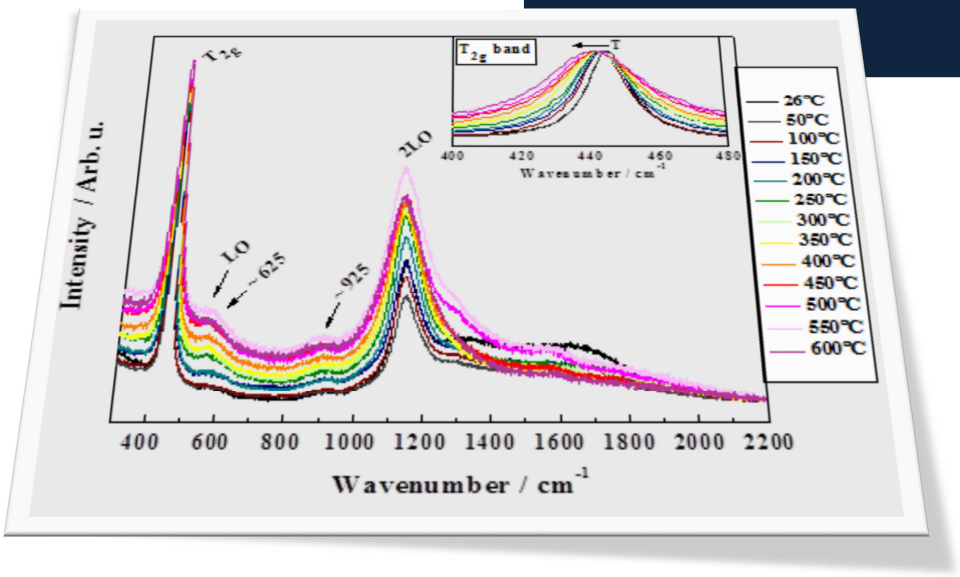

Published as "Temperature dependence of the Raman spectrum of UO_2", **J. M. Elorrieta, L. J. Bonales, V. G. Baonza and J. Cobos**, *J. Nucl. Mater.*, **503**, 191-194 (2018).
DOI:10.1016/j.jnucmat.2018.03.015
Supplementary Information: Not included in the article.

Abstract

The position of the main spectral features (located at ~445, ~575, ~625, ~925 and ~1145 cm^{-1}) in the Raman spectrum of UO_2 has been examined from room temperature up to 600°C. The wavenumber shifts measured for the observed bands have allowed us to obtain the temperature dependence ($d\omega/dT$) of the different vibrational modes. Our measurements corroborate the assignment of the band observed at ~1145 cm^{-1} to the 2LO overtone. In addition, the temperature dependence of the bandwidths of the T_{2g} and 2LO modes has been analysed.

3.4.1. Introduction

Raman spectroscopy is becoming an essential technique for the study of nuclear materials, owing to its multiple advantages with respect to other traditional techniques [1]. In this sense, Raman characterisation of UO_2 and, especially, of its higher oxidation-state oxides has been often addressed in the last years [2-8]. This is due to the fact that the majority of nuclear power plants in operation worldwide use UO_2 as fuel, and the sensitivity provided by Raman spectroscopy enables extracting valuable information for a correct understanding of the UO_2 oxidation reaction, what becomes particularly relevant for the spent fuel assessment under repository conditions. Most of the studies carried out to date have been focused on identifying the Raman spectra of the different uranium oxides involved in the oxidation process and on shedding light on the structural evolution leading to such phase changes [2-8]. However, in order to extract as much information as possible from Raman experiments, a better comprehension of all the spectral features is mandatory, and analysing the effect of both pressure and temperature on Raman spectra may help to clarify the spectral assignment of the target compounds.

Livneh and Sterer studied the effect of pressure on the Raman spectrum of UO_2 and assigned the band located around 1150 cm^{-1} to the first overtone of the LO mode [9], previously assigned to the Γ_5- Γ_3 crystal field electronic transition [10]. However, to the best of our knowledge, further studies to corroborate the broadly assumed 2LO mode assignment have not been reported to date.

Concerning the temperature effects on the Raman spectrum of UO_2, Guimbretière *et al.* studied only the T_{2g} band as a function of temperature and provided a set of empirical equations to estimate such parameter on a given UO_2 sample, taking into account the variation of both the position and width of this Raman band [11]. Nonetheless, as far as we know, the temperature dependence of the full Raman spectrum of UO_2 has not yet been reported. Here we present a detailed analysis of the temperature coefficients ($d\omega/dT$) of the most representative spectral features found in the Raman spectrum of UO_2, which have been used to verify the 2LO assignment of the Raman band located at ~1145 cm^{-1}. Furthermore, the variation with temperature of the bandwidths of both T_{2g} and 2LO bands has been examined as well.

3.4.2. Experimental details

3.4.2.1. Materials

The sample used in this work consisted in an annealed UO_2 disk supplied by ENUSA.

3.4.2.2. Raman spectroscopy

In situ Raman characterisation of UO_2 as a function of temperature was performed using a Linkam THMS600 temperature stage coupled to the BX41 Olympus microscope of a Horiba LabRAM HR Evolution Raman spectrometer. The mechanical design and electronics of the temperature stage provided precise control and a temperature stability better than 0.2 degrees over the whole temperature range.

The atmosphere used while heating the UO_2 disk was a (N_2+4.7%H_2) flow, with the aim of preventing oxidation (what was verified by ensuring that the Raman spectrum after the heat treatment was identical to the initial). A heating ramp of 10°C/min was applied to reach the measured temperatures –from room temperature to 600°C at 25°C steps–, and a thermalisation time of 15 minutes at each selected temperature before acquiring the Raman spectra.

Raman spectra were excited at 632.8 nm provided by a He-Ne laser. The laser beam was focused on the sample through a 50x long-working distance objective, allowing us to measure through the silica window of the Linkam stage. The

excitation power was optimised to avoid both alteration and overheating of the samples. The collected backscattered radiation was dispersed with a 600 grooves/mm grating and recorded using a CCD detector, obtaining a spectral resolution of better than 3 cm^{-1}. The acquired spectra were calibrated with the emission lines of a Ne discharge lamp, recorded just before measuring at each temperature.

3.4.3. Results and discussion

3.4.3.1. Raman spectrum of UO_2 as a function of temperature

Figure 3.4.1 gathers some of the Raman spectra obtained on the UO_2 disk over the whole temperature range studied (26ºC-600ºC), where five spectral features were detected.

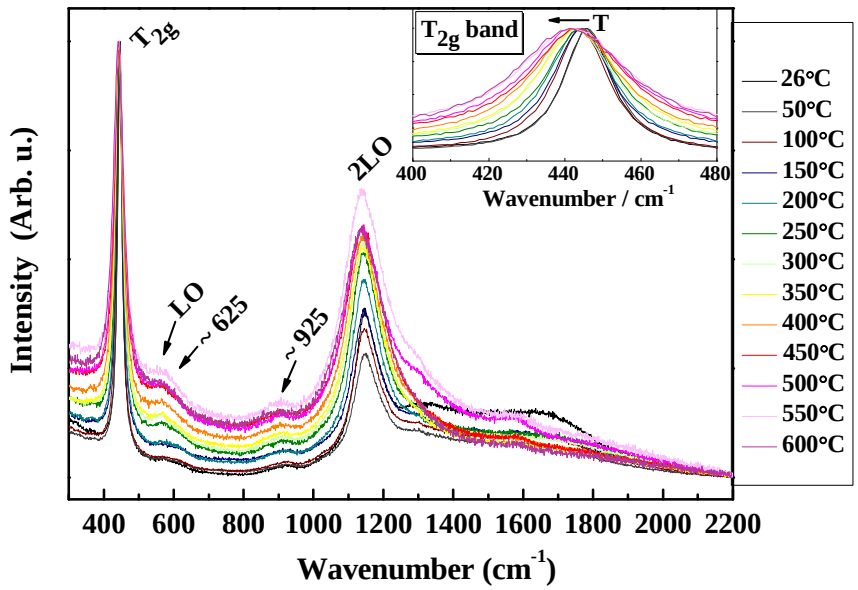

Fig. 3.4.1. UO_2 Raman spectrum acquired at different temperatures under H_2/N_2 atmosphere, normalised with respect to the T_{2g} band. Inset shows the shift experienced by the T_{2g} band due to the temperature increase.

These features correspond to (all wavenumbers measured at room temperature): 1) the main characteristic T_{2g} band located at 445 cm^{-1} [12], 2) the ~575 cm^{-1} band, attributed to the Raman-forbidden LO mode [13,14], that becomes active due to the combined effect of lattice defects and resonance enhancement [6,15], 3) the band around 625 cm^{-1}, recently associated with oxidation [7,8] (thus suggesting a minor surface oxidation of the UO_2 disk), 4) the band located at ~925 cm^{-1} which has been reported as $2TO_R$ [9], and 5) the ~1145 cm^{-1} band, whose 2LO mode assignment [9] confirmation is one of the aims of this work.

As expected, all Raman bands downshift in wavenumber with increasing temperature due to both volume and anharmonic effects. This is especially evident for the T_{2g} band, given its narrower bandwidth (inset in Figure 3.4.1). It is widely assumed that the temperature dependence of each phonon frequency consists of two additive contributions [16,17]. The so-called 'implicit' contribution is that due to the thermal expansion of the lattice, which can be calculated from available experimental volumetric data. The second contribution arises from anharmonic interactions between phonons. It is labelled the 'explicit' contribution and is usually modelled using three-phonon and four-phonon processes. In our case, we were unable to model the frequency softening because accurate thermal expansion or equation of state data are lacking across the temperature range covered in our experiments.

3.4.3.2. Temperature dependence of the bands wavenumber

A precise analysis of the wavenumber variation with temperature of each Raman feature of UO_2 is shown in Figure 3.4.2. For this purpose, a second derivative analysis [18-20] was previously performed on all the acquired Raman spectra. The temperature coefficients ($d\omega/dT$) were subsequently obtained for all the vibrational modes (Figures 3.4.2a-3.4.2e). These coefficients are gathered in Table 3.4.SI (see Section 3.4.S1 in Supplementary Information).

For the sake of comparison with existing results, we compare in Figure 3.4.2a the evolution of the T_{2g} band with temperature with those reported by Guimbretière *et al.* [11]. Both sets of data are in excellent agreement, showing a downshift of around 3-4 cm^{-1} across the temperature range covered in both studies.

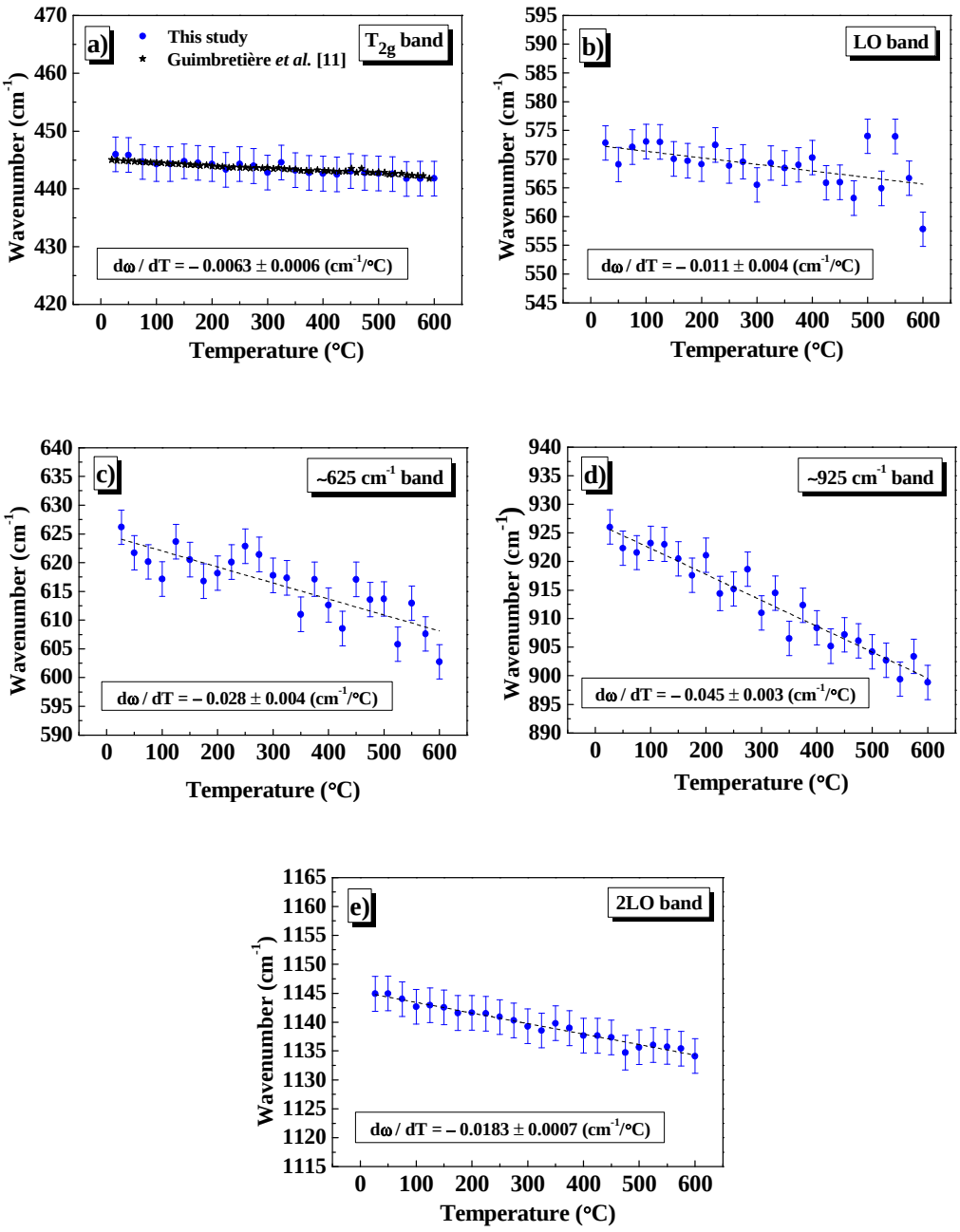

Fig. 3.4.2. Wavenumber shift with temperature of the different bands featured in the Raman spectrum of UO_2: a) T_{2g}, b) LO, c) ~625 cm^{-1}, d) ~925 cm^{-1} and e) 2LO bands.

3.4.3.3. Confirmation of the 2LO mode assignment

These results allow us to check the assignment for the ~1145 cm^{-1} band [9], since the wavenumber of an overtone must fit twice the corresponding fundamental wavenumber under an external perturbation, in our case the temperature. We therefore compare in Figure 3.4.3 the temperature dependences of ω_{LO} (Figure 3.4.2b) and half the 1145 cm^{-1} band (Figure 3.4.2e).

It is readily observed that both sets of data match accurately and exhibit similar temperature dependencies. This finding corroborates that the ~1145 cm^{-1} band corresponds indeed to the first overtone of the LO mode band [9], so we have labelled $\omega_{2LO}/2$ in the figure.

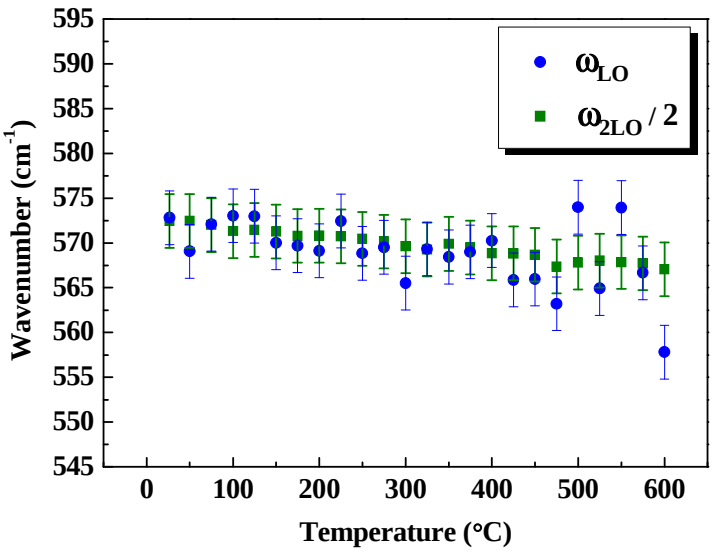

Fig. 3.4.3. Comparison between the LO band shift (ω_{LO}) and half the 2LO band shift ($\omega_{2LO}/2$) as a function of temperature.

3.4.3.4. Temperature dependence of the bandwidths

Likewise, the variation with temperature of the bandwidth has also been analysed for the most prominent bands of the Raman spectrum, *i.e.* T_{2g} and 2LO. It was not possible to properly carry out such analysis on the other bands due to their much lower signal-to-noise ratios.

Figure 3.4.4a shows, by way of example, those band-shape fits performed on T_{2g} and 2LO bands of the Raman spectrum acquired at room temperature (setting the band position/wavenumber value previously obtained by the second derivative analysis). In the case of the 2LO band, the second derivative analysis was not sufficient to resolve other contributions on the right side of the band profile which have been related to crystal field transitions [10].

The evolution of the T_{2g} and 2LO bandwidths as a function of temperature is plotted in Figures 3.4.4b and 3.4.4c, respectively. Again, our data are in very good agreement with those reported by Guimbretière *et al.* [11] over the whole measured range (Figure 3.4.4b), despite the fact that the bandwidth may be influenced by impurities and defects on the sample. In addition, the temperature dependence of the T_{2g} mode bandwidth has been satisfactorily modelled in terms of the anharmonic decay of phonons (see Section 3.4.S2 in Supplementary Information).

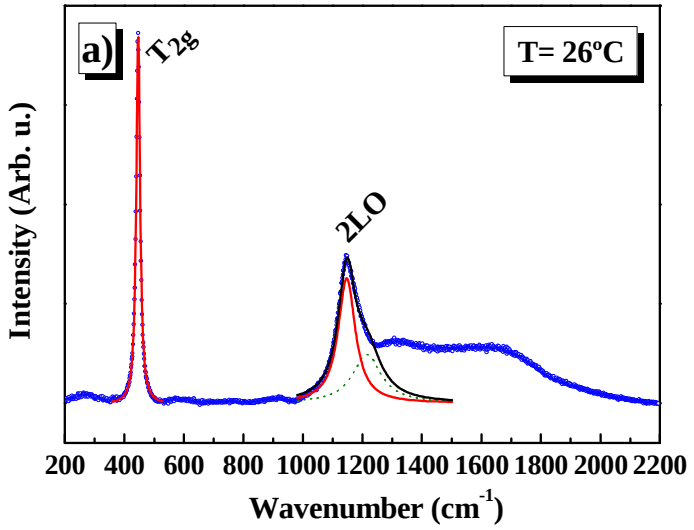

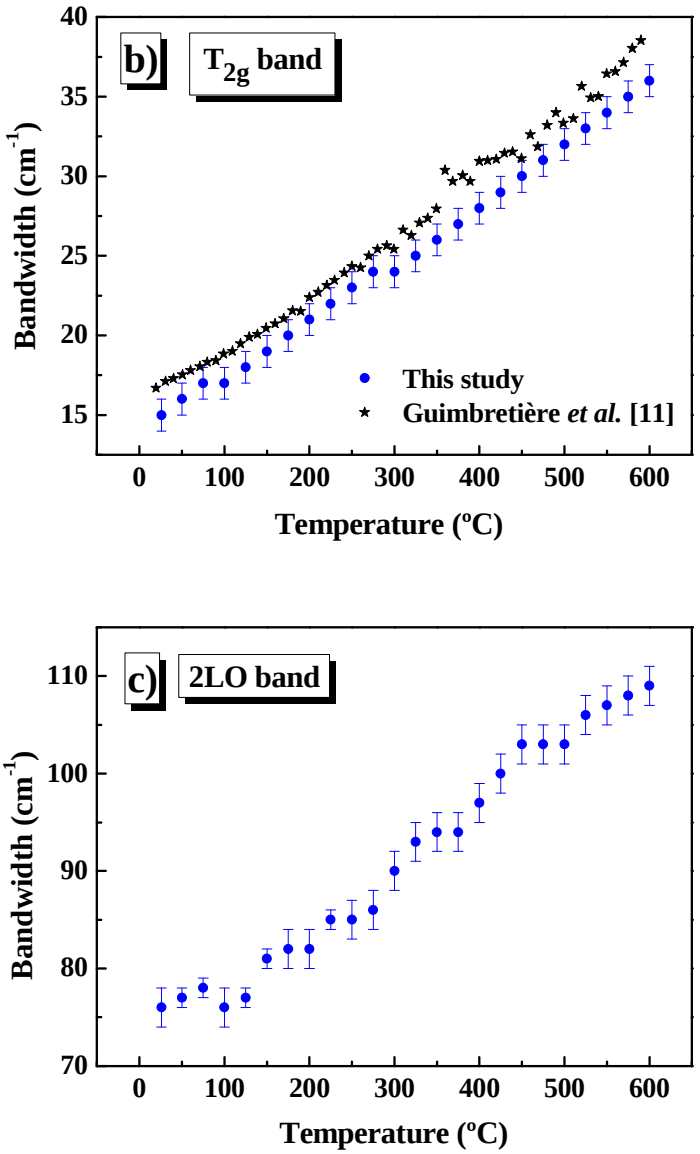

Fig. 3.4.4. Raman spectrum of UO_2 acquired at room temperature, where the Lorentzian band-shape fits performed on T_{2g} and 2LO bands are shown (a)). Variation with temperature of the bandwidth of b) T_{2g} and c) 2LO bands. As a tentative analysis, we have included in a) a Lorentzian fit of the ~1209 cm^{-1} Crystal Field (CF) contribution (see dashed band) [10], since it appears as a slight distortion on the right side of the 2LO band in the second derivative spectrum obtained at room temperature.

3.4.4. Conclusions

The Raman spectrum of UO_2 has been assessed as a function of temperature. In particular, a detailed analysis of the position (wavenumber) of every featured band from room temperature up to 600°C has been conducted.

Consequently, the temperature coefficient $d\omega/dT$ of every characteristic Raman band has been obtained, being the one corresponding to the T_{2g} band in good agreement with the sole data reported in the literature in this regard. At the same time, these results have allowed us to confirm the assignment of the ~1145 cm^{-1} band to the first overtone (2LO) of the LO band.

In addition, the temperature dependence of the bandwidths of the main characteristic Raman bands of UO_2, *i.e.* T_{2g} and 2LO modes, has been analysed. These results have also been found to be in agreement with the existing data in relation to the T_{2g} bandwidth evolution with temperature.

3.4.5. Acknowledgements

This work was supported by ENRESA within the project Nº 079000189, entitled “Aplicación de técnicas de caracterización en el estudio de la estabilidad del combustible nuclear irradiado en condiciones de almacenamiento” (ACESCO). VGB acknowledges support from MINECO under project CTQ2015-67755-C02-01-R.

3.4.6. References

[1] L. J. Bonales, J. M. Elorrieta, A. Lobato and J. Cobos, Raman Spectroscopy, a Useful Tool to Study Nuclear Materials, Applications of Molecular Spectroscopy to Current Research in the Chemical and Biological Sciences, Dr. Mark Stauffer (Ed.), InTech (2016). ISBN 978-953-51-2681-2. DOI: 10.5772/64436.
[2] G. C. Allen, I. S. Butler and N. A. Tuan, J. Nucl. Mater., 144, 17-19 (1987).
[3] I. S. Butler, G. C. Allen and N. A. Tuan, Appl. Spectrosc., 42 (5), 901-902 (1988).
[4] M. L. Palacios and S. H. Taylor, Appl. Spectrosc., 54, 1372-1378 (2000).
[5] D. Manara and B. Renker, J. Nucl. Mater., 321, 233-237 (2003). DOI:10.1016/S0022-3115(03)00248-4.

[6] H. He and D. Shoesmith, Phys. Chem. Chem. Phys., 12, 8108-8117 (2010). DOI: 10.1039/B925495A.
[7] L. Desgranges, G. Baldinozzi, P. Simon, G. Guimbretière and A. Canizares, J. Raman Spectrosc., 43, 455-458 (2012). DOI: 10.1002/jrs.3054.
[8] J. M. Elorrieta, L. J. Bonales, N. Rodriguez-Villagra, V. G. Baonza and J. Cobos, Phys. Chem. Chem. Phys., 18, 28209-28216 (2016). DOI: 10.1039/c6cp03800j.
[9] T. Livneh and E. Sterer, Phys. Rev. B, 73, 085118-085119 (2006). DOI: 10.1103/PhysRevB.73.085118.
[10] J. Shoenes, J. Chem. Soc., Faraday Trans. 2, 83, 1205-1213 (1987). DOI: 10.1039/F298783FX025.
[11] G. Guimbretière, A. Canizares, N. Raimboux, J. Joseph, P. Desgardin, L. Desgranges, C. Jégou and P. Simon, J. Raman Spectrosc., 46 (4), 418-420 (2015). DOI 10.1002/jrs.4661.
[12] P. G. Marlow, J. P. Russell and J. R. Hardy, Philos. Mag., 14, 409-410 (1966). DOI: 10.1080/14786436608219022.
[13] J. D. Axe and G. D. Pettit, Phys. Rev., 151 (2), 676-680 (1966). DOI: 10.1103/PhysRev.151.676.
[14] J. Schoenes, Phys. Rep., 63 (6), 301-336 (1980). DOI: 10.1016/0370-1573(80)90158-1.
[15] G. Guimbretière, L. Desgranges, A. Canizares, G. Carlot, R. Caraballo, C. Jégou, F. Duval, N. Raimboux, M. R. Ammar and P. Simon, Appl. Phys. Lett., 100, 251914 (2012). DOI: 10.1063/1.4729588.
[16] M. Balkanski, R. F. Wallis and E. Haro, Phys. Rev. B, 28, 1928-1934 (1983). DOI: https://doi.org/10.1103/PhysRevB.28.1928.
[17] S. D. Pandey, J. Singh, K. Samanta, N. D. Sharma and A. K. Bandyopadhyay, J. Nanomat., 16, 492967 (2015). DOI: 10.1155/2015/492967.
[18] G. Talsky, Derivative Spectrophotometry: Low and High Order, Verlagsgesellschaft, Weinheim (Federal Republic of Germany) and Inc., New York, NY (USA) (1994). ISBN 3-527-28294-7.
[19] M. Cáceres, A. Lobato, N. J. Mendoza, L. J. Bonales and V. G. Baonza, *Phys. Chem. Chem. Phys.*, **18**, 26192-26198 (2016). DOI: 10.1039/C6CP03857C.
[20] E. del Corro, M. Taravillo, J. González and V. G. Baonza, *Carbon*, **49**, 973-979 (2011). DOI:10.1016/j.carbon.2010.09.064.

Supplementary Information

3.4.S1. Temperature coefficients ($d\omega/dT$)

Table 3.4.SI. List of the temperature coefficients obtained for the different vibrational modes featured in the Raman spectrum of UO_2. The wavenumber value assigned to each mode refers to that corresponding to room temperature.

VIBRATIONAL MODE	TEMPERATURE COEFFICIENT ($d\omega/dT$) ($cm^{-1}/^oC$)
T_{2g} (~445 cm^{-1})	-0.0063 ± 0.0006
LO (~575 cm^{-1})	-0.011 ± 0.004
~625 cm^{-1}	-0.028 ± 0.004
~925 cm^{-1}	-0.045 ± 0.003
2LO (~1145 cm^{-1})	-0.0183 ± 0.0007

3.4.S2. Modelling the T_{2g} mode bandwidth behaviour

The changes in the bandwidth Γ should reflect the anharmonic decay of phonons with temperature, which can be modelled using the following expression [1]:

$$\Gamma(T) = \Gamma_0 + C\left[1 + \frac{2}{e^{\hbar\omega_0/2kT} - 1}\right] + D\left[1 + \frac{3}{e^{\hbar\omega_0/3kT} - 1} + \frac{3}{(e^{\hbar\omega_0/3kT} - 1)^2}\right]$$

(Eq. 3.4.S1)

in which C and D are constants accounting for cubic (three phonon) and quartic (four phonon) anharmonic processes, respectively, and ω_0 is the frequency of the phonon considered.

By inserting the frequency of the T_{2g} phonon (445 cm^{-1}) into Equation 3.4.S1 and using the values of C = 1.66 and D = 0.33 reported by Pandey *et al.* [2] for nanocrystalline CeO_2, we were able to accurately fit $\Gamma(T)$ with Γ_0 = 10 cm^{-1} (continuous line in Figure 3.4.S1). This result is quite interesting, since it suggests that both UO_2 and CeO_2 lattices exhibit similar anharmonic mechanisms for the decay of phonons.

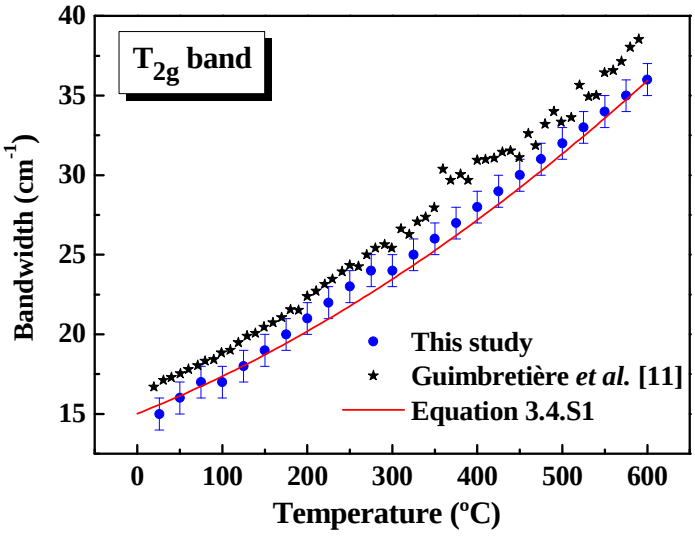

Fig. 3.4.S1. Variation with temperature of the bandwidth of the T_{2g} mode (Figure 3.4.4b), where the modelled data have been included.

3.4.S3. References

[1] M. Balkanski, R. F. Wallis and E. Haro, *Phys. Rev. B*, **28**, 1928-1934 (1983). DOI: https://doi.org/10.1103/PhysRevB.28.1928.
[2] S. D. Pandey, J. Singh, K. Samanta, N. D. Sharma and A. K. Bandyopadhyay, *J. Nanomat.*, **16**, 492967 (2015). DOI: 10.1155/2015/492967.

Result 5

Pu effect on $(U, Pu)O_2$ oxidation

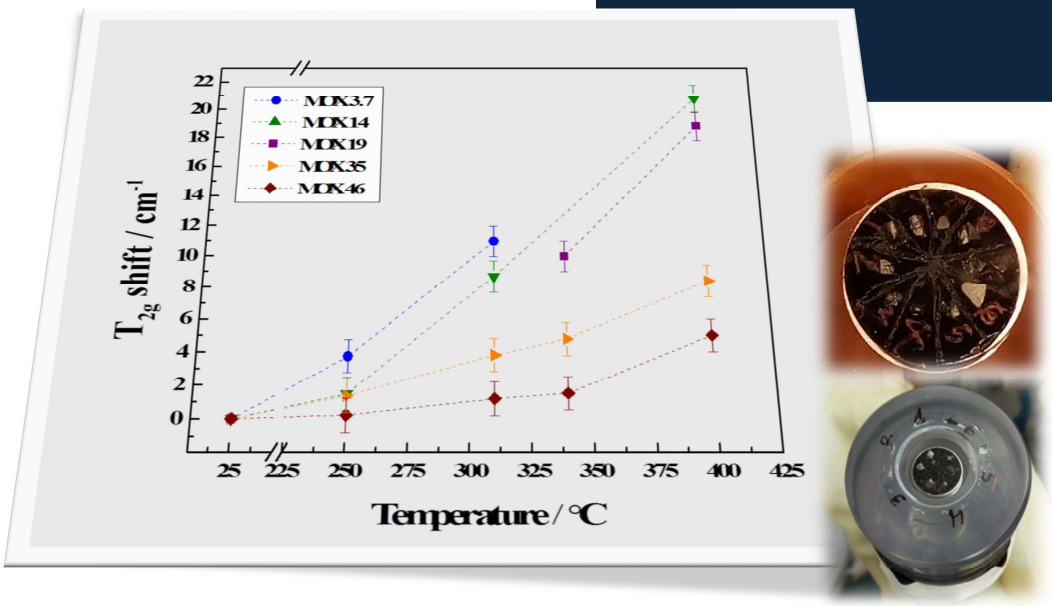

Published as "Raman study of the oxidation in $(U, Pu)O_2$ as a function of Pu content", **J. M. Elorrieta, D. Manara, L. J. Bonales, J. F. Vigier, O. Dieste, M. Naji, R. C. Belin, V. G. Baonza, R. J. M. Konings and J. Cobos** , *J. Nucl. Mater.*, **495**, 484-491 (2017).
DOI: 10.1016/j.jnucmat.2017.08.043

Abstract

This work presents a systematic Raman study of the matrix oxidation in a variety of (U_{1-y}, Pu_y)O_2 compositions ($0 \leq y \leq 0.46$) at different temperatures, between 250ºC and 400ºC. Our results indicate that the increase in Pu content hinders the oxidation process of the dioxide matrix. Further oxidation of the uranium-plutonium mixed dioxides in air starts between 250°C and 310°C, on a time scale of several hours. M_4O_9 seems to be the most stable intermediate phase formed upon oxidation of all the investigated mixed oxides, before final oxidation to M_3O_8. In addition, X-ray diffraction measurements and SEM images confirm the trend observed by Raman spectroscopy, i.e. Pu stabilises the fcc structure of the dioxide.

3.5.1. Introduction

The performance assessment of spent nuclear fuel (SNF) stability under dry interim storage conditions is of great importance in nuclear waste technology. In case of failure of the engineered containment barriers, oxidation of the spent fuel matrix (UO_2) might take place depending on the oxygen concentration in the surroundings and the temperature produced by the decay heat. As is well known, oxidation of UO_2 to U_3O_8 involves an increase in volume of around 36% that might affect fuel integrity and, consequently, storage safety [1]. Hence, it becomes necessary to understand in detail how this reaction proceeds, analysing step-by-step not only the different uranium oxides that take part in the oxidation, but also the reaction mechanisms responsible for the consecutive structural transitions along the $UO_2 \rightarrow U_4O_9/U_3O_7 \rightarrow U_3O_8$ transformation [2].

In particular, the first stage of the latter reaction, *i.e.* UO_2 evolution to U_4O_9/U_3O_7, takes on special interest owing to the fact that various crystal symmetry transitions occur along this compositional range while the overall structure remains cubic [3]. Such transitions have been experimentally detected by means of Raman spectroscopy and X-ray diffraction (XRD) [4,5]. As additional oxygen atoms are incorporated into the *Fm-3m* cubic lattice, they continuously rearrange without altering it in a significant way, eventually giving rise to a so-called superstructure. This corresponds to the U_4O_9 phase, which

consists of a very densely packed cubic structure where oxygen atoms arrange themselves into cuboctahedral clusters [6]. Likewise, U_3O_7 has a distorted cubic lattice, only differing from U_4O_9 in the slight alteration caused by the excess of oxygen [3].

Full comprehension of this oxidation reaction becomes even a greater challenge when, instead of dealing with pure uranium dioxide, it concerns uranium-based mixed oxides like (U, Pu)O_2, commonly referred to as MOX, and (U, Am)O_{2-x}. Such is the case of the potential fuels for fast neutron reactors, mainly intended for nuclear waste radiotoxicity reduction. In this sense, it is certainly necessary to assess the behaviour of the transuranium elements within the UO_2 matrix and their influence on the stability of this kind of SNF against oxidation/corrosion during storage.

Especially, the effect of Pu incorporation into the UO_2 matrix has been frequently addressed, since MOX fuels have been used for at least 30 years in some countries, *e.g.* France, Belgium or Germany, with the aim of recycling Pu in Light Water (thermal) Reactors (LWR) [7]. In this way, (U_{1-y}, Pu_y)O_2 oxides with different *y* values as well as a few spent MOX fuels have been characterised and their oxidation in some cases investigated [8-21]. In these studies, a variety of experimental techniques have been employed, although XRD is by far the most frequent. Already in the 1970s, XRD measurements were applied for analysing the oxidation products of uranium-plutonium mixed oxides obtained in a thermal balance [8,9]. More recently, the effect of Pu content on the mixed dioxide lattice parameter at room temperature and the structure evolution after oxidation have been assessed [10-17]. In all of them the lattice parameter has been reported to follow Vegard's law, decreasing linearly as a function of plutonium concentration. With regard to oxidation of (U_{1-y}, Pu_y)O_2 oxides at different temperatures, it has been found that Pu stabilises the cubic phase during the reaction and that the temperature of M_3O_8 formation is higher as Pu content increases [15].

Furthermore, Raman spectroscopy of nuclear materials and actinide compounds has been broadly developed in the last decade [4,5,18-34]. This is not only due to advances in Raman spectroscopy approaches, their versatility, and potential non-contact analyses, but also to the improvement of confinement techniques for highly radioactive materials [21,30,31], which have allowed the study of hazardous compounds practically unexplored until the last decade of the Twentieth Century.

Concerning uranium-plutonium mixed oxides, certain studies have provided Raman characterisation of both unirradiated samples and spent fuels corresponding to different Pu contents [18-22]. A higher oxidation resistance of this kind of mixed dioxides as Pu concentration increases has also been reported [20,21].

Nevertheless, none of these studies has systematically evaluated, directly by Raman spectroscopy, the matrix oxidation of (U, Pu)O_2 mixed oxides under different temperature conditions and as a function of Pu content. Such a detailed Raman analysis of the matrix oxidation, within a varying range of Pu concentrations, is presented here for the first time.

3.5.2. Experimental

3.5.2.1. Materials

A variety of starting (U_{1-y}, Pu_y)O_2 fragments, averaging 1-3 mm in surface size, with different Pu contents ranging from y = 0 up to y = 0.46 were used in this work. Some of them were provided by CEA (Commissariat à l'Energie Atomique, France) and others by JRC Karlsruhe (Joint Research Centre, Germany). CEA samples were prepared and characterised by a well established powder metallurgy procedure described in previous publications [17]. JRC samples were prepared by sintering powders produced by sol-gel technique, as described elsewhere [22]. Table 3.5.I comprises data concerning the samples, such as the *MOX* reference utilised hereafter for each one, the proportion of Pu they contain and their provider.

Table 3.5.I. List of (U, Pu)O_2 mixed oxides used in this work.

REFERENCE	Pu CONTENT (mol%) (±2)	PROVIDER
UO_2	0	JRC
MOX 3.7	3.7	JRC
MOX 14	14	CEA
MOX 19	19	CEA
MOX 35	35	CEA
MOX 46	46	CEA

3.5.2.2. Sample preparation

Starting samples listed in Table 3.5.I were annealed at 1600°C during 15 min under reducing conditions (Ar + 6.5% H_2 flow), enabling the removal of lattice defects expected from alpha self-irradiation. Thereafter, the oxidation procedure consisted in heating them at a constant rate of 10°C/min up to a given temperature in each experiment, *i.e.* 250, 310, 340 and 400°C, under a synthetic air flow and maintaining the selected temperature for three hours. The samples were withdrawn immediately after this time period elapsed, with the aim of avoiding further oxidation due to the slow inertial cooling of the furnace tube. Both annealing and oxidation experiments were carried out in an alumina tube furnace.

3.5.2.3. Raman spectroscopy

Due to the radioactivity of the MOX samples, it was necessary to encapsulate them prior to Raman spectra measurements into α-shielding Plexiglas capsules recently designed and developed by JRC Karlsruhe [31]. The spectra were recorded through the quartz window on top of these capsules.

Raman measurements were performed with a Jobin-Yvon T64000 spectrometer. All spectra were acquired at an excitation wavelength of 647 nm, provided by a Kr^+ laser. The laser beam was focused on the sample through a long focal distance objective (NA (*Numerical Aperture*) = 0.5) with 50x magnification. The excitation power was optimised between 50-100 mW (being around 5 times lower at the sample surface [29]) in order to prevent further oxidation of the samples by the laser. The scattered radiation was dispersed using an 1800 grooves/mm holographic grating and recorded by a liquid-nitrogen cooled CCD detector. The single spectrograph configuration applied enabled a spectral resolution of ±1 cm^{-1}. The spectrometer was daily calibrated using the T_{2g} phonon (520.5 cm^{-1}) of a silicon single crystal [35].

3.5.2.4. X-ray diffraction

XRD analyses were performed on crushed samples. About 20 mg of powder were loaded in an epoxy resin to avoid excessive dispersion of radioactive powder. A Seifert XRD-3003 X-ray diffractometer (Cu Kα radiation) with a Bragg-Brentano θ/θ configuration was used for the analyses. The device is implemented in a glove-box for radioactive material confinement. The powder

patterns were recorded using a step size of 0.02° across the angular range 10° ≤ 2θ ≤ 120°. Structural analyses were performed by the Rietveld method using Jana2006 software [36]. Peak-profile analysis was carried out using pseudo-Voigt band-shapes.

3.5.2.5. Scanning electron microscopy

The scanning electron microscopy used in this work is a Philips XL40 SEM (Philips, Amsterdam, Netherlands), which has been modified in order to be used for the examination of highly active or irradiated nuclear materials [37,38]: the chamber, column, turbomolecular pump and the high voltage unit are mounted inside a glove-box in order to keep the contamination in a confined space, whereas the primary vacuum system, water cooling circuit and acquisition electronics are placed outside, provided those parts are not contaminated by the active samples, thus facilitating the equipment maintenance. The microscope is equipped with Secondary-electron detector (SE) which gives a morphology-related signal, Backscattered-electron detector (BSE) which provides images with Z-related contrast, and Energy dispersive X-ray spectroscopy (EDS) used to obtain elemental analysis of the samples. The beam was operated during this work at 25 kV.

3.5.3. Results and discussion

3.5.3.1. Initial characterisation

XRD and X-ray absorption spectroscopy (XAS) characterisation of the samples was performed on as-fabricated materials. Both their composition and the attainment of single phase materials were confirmed, based on XRD. The results of these characterisation campaigns are published in previous papers [15,22].

Prior to conducting the different oxidising heat treatments, Raman spectra of each annealed MOX sample were acquired, as shown in Figure 3.5.1. UO_2 spectrum features two characteristic bands at about 445 and 1150 cm^{-1}, which are well known and correspond to the T_{2g} mode [39] and the 2LO phonon overtone [40], respectively. Inasmuch as Pu content increases, the general aspect of the spectra changes: a) the T_{2g} band shifts continuously to higher wavenumbers, b) the 2LO band diminishes until it is no longer discernible, c) a broad band appears

at 500-600 cm^{-1} (labelled with a rhombus), and d) another feature is observed around 850-1000 cm^{-1}.

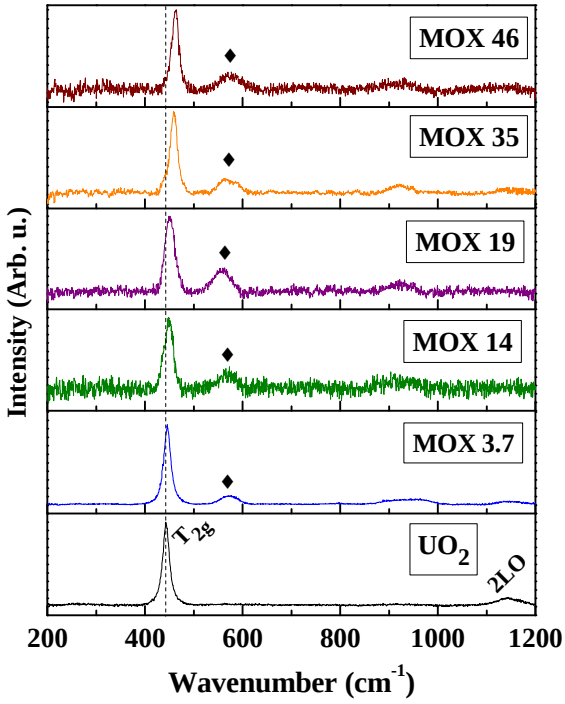

Fig. 3.5.1. Raman spectra of the initial $(U_{1-y}, Pu_y)O_2$ samples, with $0 \leq y \leq 0.46$.

The continuous shift to higher wavenumbers of the T_{2g} band with the increase of Pu content is caused by the shortening of the M(U, Pu)-O bonds [20]. The upshift in the T_{2g} mode is essentially linear, ranging from around 445 cm^{-1} for pure UO_2 to 478 cm^{-1} for pure PuO_2 [4,22,24,25,29,30,39-44]. Both the attenuation of the 2LO peak and the appearance of a new band *ca.* 500-600 cm^{-1} can be associated with lattice distortions (non-perfect fluorite structure) [4,27,42,44], due in this case to the partial substitution of U atoms by Pu atoms. The simultaneous presence of Pu^{3+} and U^{5+} cations, already observed in this kind of compounds for example by X-ray absorption spectroscopy [22], might in fact foster the formation of Frenkel-like defects, which have been proposed to be responsible for an analogue spectral feature found around 575 cm^{-1} in UO_2 [45] and at ~578 cm^{-1} in PuO_2 [29]. The broad band at 850-1000 cm^{-1} might be related to the first overtone of the T_{2g} mode of PuO_2 [29,46]. Slight differences in the intensity ratios of some bands when comparing with previous studies [19,20] may be attributed to the different excitation wavelength used in this work [3].

A second derivative analysis [47] was applied to every spectrum with the aim of determining the position of the T_{2g} band more accurately for each MOX sample. The approximately linear behaviour of the T_{2g} position as a function of Pu content in the mixed oxides (Figure 3.5.2a) reflects the correct estimation of the Pu content value for all the samples, assuming a one-mode T_{2g} vibration [48].

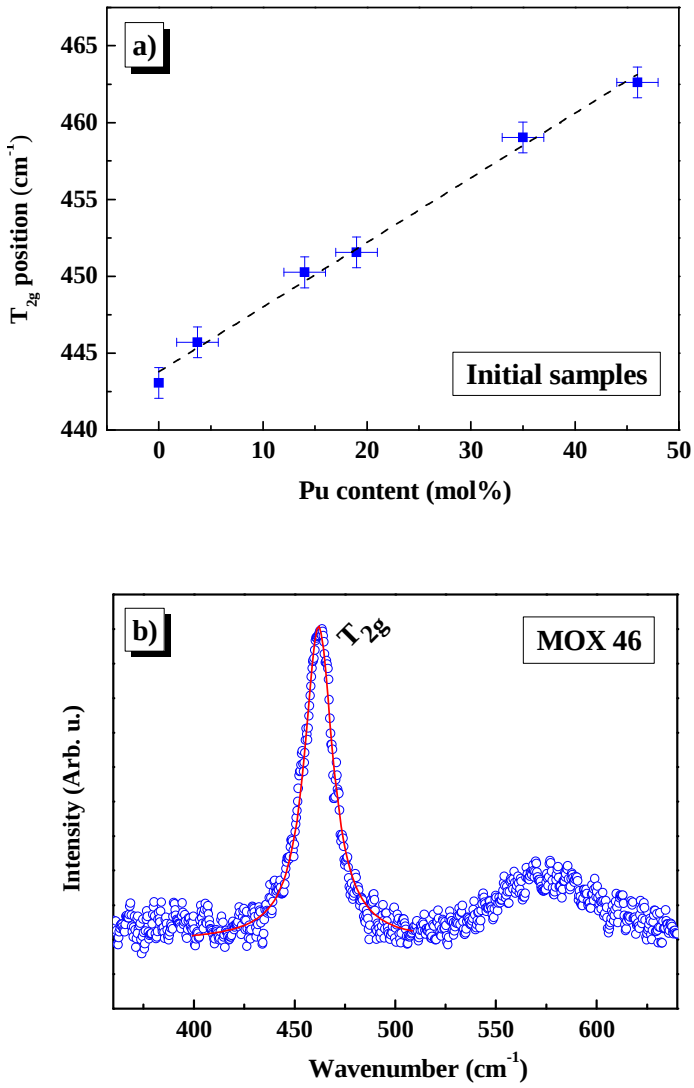

Fig. 3.5.2. a) Position of the T_{2g} band vs. Pu content of the different MOX samples. b) Peak fitting performed on the T_{2g} band of MOX 46 Raman spectrum.

This one-mode model assumption, already reported in previous studies [19,20,22], was confirmed by fitting the T_{2g} band and ascertaining a single-peak contribution. Figure 3.5.2b shows these peak fitting results in the case of MOX 46, where a two-mode behaviour should be noticeable (if existing), but a sole peak is likewise observed. T_{2g} positions are also in good agreement with those reported by Böhler et al. [22].

3.5.3.2. Behaviour under different temperature conditions

3.5.3.2.1. Raman analysis

Following every oxidising heat treatment, characterisation of the treated MOX samples was carried out by Raman spectroscopy. Figure 3.5.3 compiles the recorded spectra, organised on the basis of the temperature maintained in each experiment (250, 310, 340 and 400°C). A few spectra are missing due to lack or damage of certain samples when the measurements were performed.

Figure 3.5.3a shows that the spectra of those oxides subjected to 250°C remained almost unaltered, featuring essentially the same bands as the initial samples: T_{2g} and 2LO bands in the case of UO_2, and T_{2g} and 500-600cm^{-1} bands (marked again with a rhombus) for MOX samples. This suggests that no significant oxidation occurred, at least within the Raman laser penetration depth scale, which is estimated to be around 500 nm for our set-up and materials. However, a slight superficial oxidation seems to have taken place, as pointed out by: 1) an appreciable symmetry loss of the T_{2g} band-shape and the appearance of a very broad feature around 700-800 cm^{-1} (characteristic of U_3O_8) in the UO_2 spectrum, and 2) the slight T_{2g} shift detected for those MOX samples with the lowest Pu content (particularly in MOX 3.7).

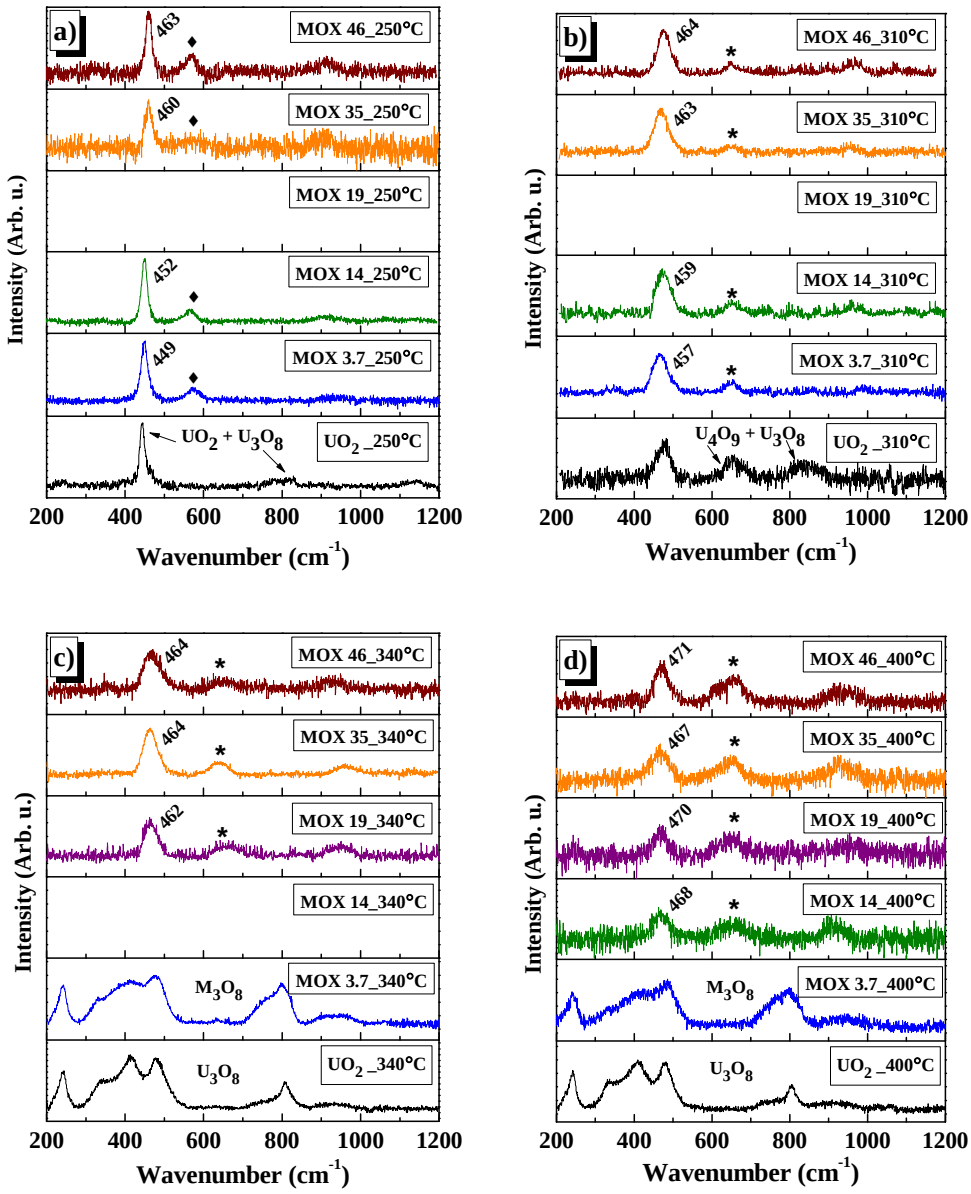

Fig. 3.5.3. Raman spectra of $(U_{1-y}, Pu_y)O_2$ oxides, with $0 \leq y \leq 46$, after 3 hour heat treatments at a) 250°C, b) 310°C, c) 340°C and d) 400°C under a synthetic air flow. Blank spaces correspond to missing spectra (due to lack or damage of certain samples when the measurements were performed) and have not been removed for the sake of clarity.

On the other hand, results obtained for the treatments at higher temperatures (Figures 3.5.3b-3.5.3d) indicate that all samples were oxidised to a greater or lesser extent. Indeed, apart from UO_2, where traces of U_3O_8 could also be deduced from an additional band detected around 800 cm^{-1}, the M_4O_9 phase was found to be stable in all the compositions after 3 hours at 310°C (Figure 3.5.3b). The sole presence of a remarkably shifted T_{2g} mode and a broad and asymmetric band around 630 cm^{-1} was previously assigned to U_4O_9 [3]. Likewise, this shifted and broadened T_{2g} band and a wide feature observed around 640-645 cm^{-1} have been recently associated with the M_4O_9 phase when oxidising both an aged MOX 24 and an agglomerate (with about 20% Pu content) of a spent MOX fuel under the laser beam [19,21]. The same two features can be observed in every spectrum of Figure 3.5.3b, where an asterisk marks the appearance of the *ca.* 640 cm^{-1} band. It should be noted that the 500-600 cm^{-1} band is no longer observed, what might suggest the disappearance of Frenkel-like defects and thus the formation of M_4O_9 as a new ordered structure where even the defects manage to rearrange.

With regard to the other two treatments at higher temperatures (Figure 3.5.3c and Figure 3.5.3d), M_4O_9 was again the predominant phase, and the T_{2g} band for each MOX composition was found to be more shifted to higher wavenumbers as temperature increased. In this case, the exceptions were UO_2 and the MOX oxide with the lowest Pu concentration (*i.e.* MOX 3.7), which showed complete oxidation to M_3O_8 after the 340°C (Figure 3.5.3c) and the 400°C (Figure 3.5.3d) treatments. Conversion to M_3O_8 can be easily distinguished, owing to the appearance of several bands located at around 236, 342, 408, 480, 752 and 798 cm^{-1} [41,49]. The intensity of the 752 cm^{-1} line seems to be higher and the 342-480 cm^{-1} bands not so clearly defined for those oxides containing plutonium than for pure U_3O_8. No reference about this observation has been made in the literature before, to the best of our knowledge. In addition, a slight contribution can be detected around 800 cm^{-1} in the spectra of those MOX oxides that were not completely converted to M_3O_8 after the 400ºC treatment, especially MOX 14 and MOX 19 (Figure 3.5.3d). This might point out a minor presence of the M_3O_8 phase, although the low signal-to-noise ratio of these spectra makes it difficult to clearly assess such possibility.

All the latter results indicate that the main phase transitions ($MO_2 \rightarrow M_4O_9 \rightarrow M_3O_8$) of the uranium-plutonium mixed dioxides take place in air between 250°C and 310°C (on a time scale of several hours) and that, as previously quoted [1], Pu content plays a significant role with regard to the fcc dioxide matrix preservation. In every heat treatment the M_4O_9 phase seems to be stabilised for

high Pu content samples, hence preventing, in overall terms, further oxidation to M_3O_8. Besides, the shift in the T_{2g} mode of each partially oxidised MOX sample with respect to its initial T_{2g} position, due to oxygen incorporation into the fluorite lattice [4,5], is less significant as the Pu proportion increases (Figure 3.5.4), what points out that a higher Pu content also helps to slow down the dioxide matrix oxidation.

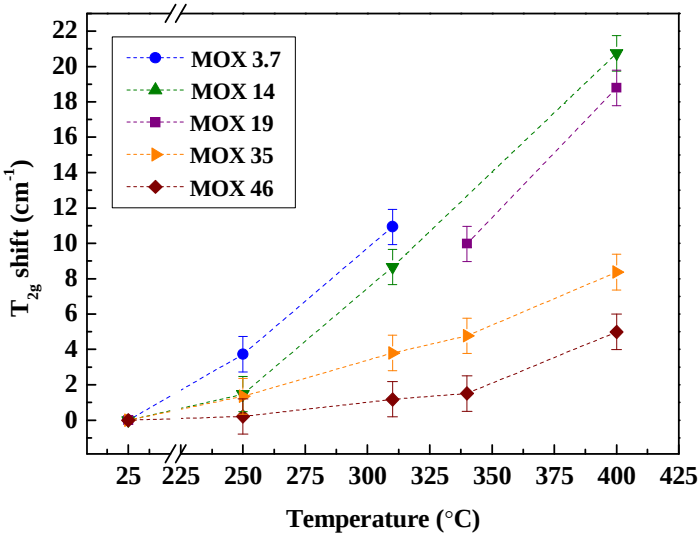

Fig. 3.5.4. T_{2g} shift of the partially oxidised $(U_{1-y}, Pu_y)O_2$ samples ($0.037 \leq y \leq 0.46$) with respect to their initial position, as a function of the heat treatment temperature.

3.5.3.2.2. XRD measurements

Due to the small quantity (some mg) of the current MOX samples available, it was possible to perform a post-heat treatment powder XRD analysis only on a few of them. The results are shown in Figure 3.5.5.

One can see in the lattice parameter vs. composition graph of Figure 3.5.5b that the formation of new oxides with O/M > 2 occurs in UO_2-richer compositions heat-treated in air. This is signified by the fact that lattice parameters of fluorite-like phases heat treated in air at 310°C are slightly, but systematically, below the values predicted by Vegard's law –except for MOX 46– (see Table 3.5.II for further detail) [52]. This effect is larger the lower the Pu content, confirming that a higher oxidation takes place in U-richer samples. The only XRD measurement performed on a MOX sample treated at 400°C (MOX 19) clearly shows a much greater deviation with respect to Vegard's-law

prediction in lattice parameter, as well as a large segregation of a M_3O_8 phase ($(U, Pu)_3O_8$ in Figure 3.5.5a). Raman results are therefore qualitatively corroborated by XRD analyses. Since powder XRD is essentially a bulk characterisation technique, the agreement between XRD and Raman results also confirms that the current Raman data are representative of bulk oxidation behaviour, and not just for the "deep surface".

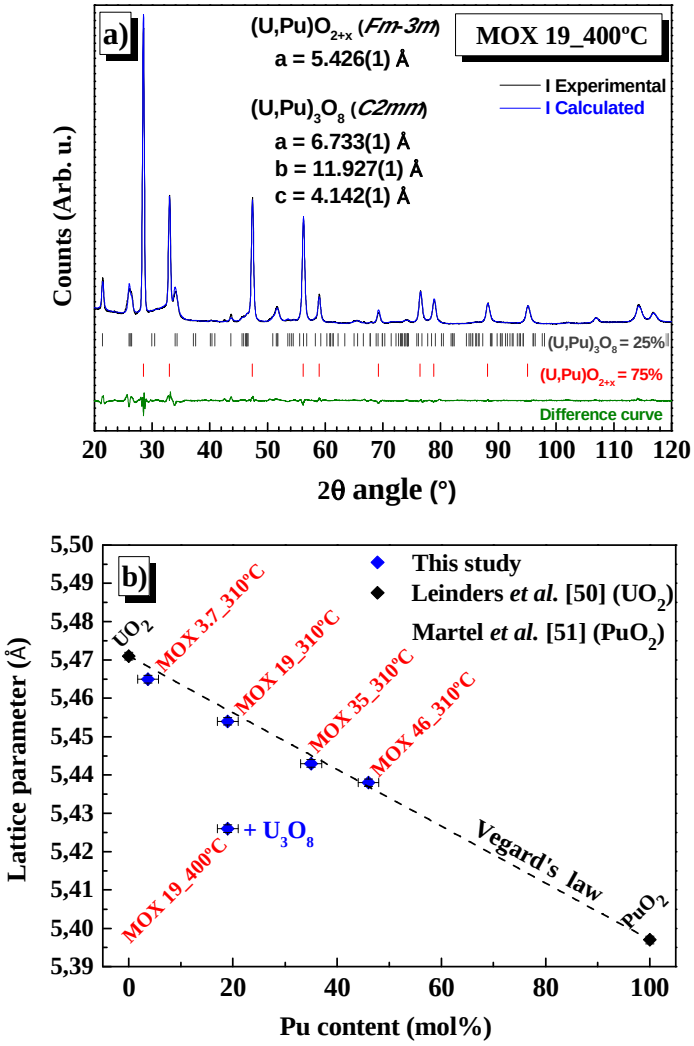

Fig. 3.5.5. a) X-ray diffraction pattern of MOX 19 after the 400ºC heat treatment. b) Lattice parameters obtained for all the measured MOX samples, as a function of Pu content. The dashed line represents values predicted by Vegard's law, taking as a reference UO_2 and PuO_2 experimental lattice parameters [50,51].

Table 3.5.II. Experimental and predicted (from Vegard's law for stoichiometric samples) lattice parameter values of the measured MOX oxides.

SAMPLE	HEAT TREATMENT APPLIED	EXPERIMENTAL LATTICE PARAMETER (Å)	VEGARD'S LAW PREDICTED LATTICE PARAMETER (Å)
MOX 3.7	3h at 310ºC	5.465(1)	5.468(1)
MOX 19	3h at 310ºC	5.454(1)	5.457(1)
MOX 19	3h at 400ºC	5.426(1)	5.457(1)
MOX 35	3h at 310ºC	5.443(1)	5.445(1)
MOX 46	3h at 310ºC	5.438(1)	5.437(1)

3.5.3.2.3. SEM images

SEM images were acquired for a variety of MOX samples treated at 250ºC (Figure 3.5.6) and 400ºC (Figure 3.5.7), in order to qualitatively investigate the crystal grain morphology and correlate it to Raman and XRD results.

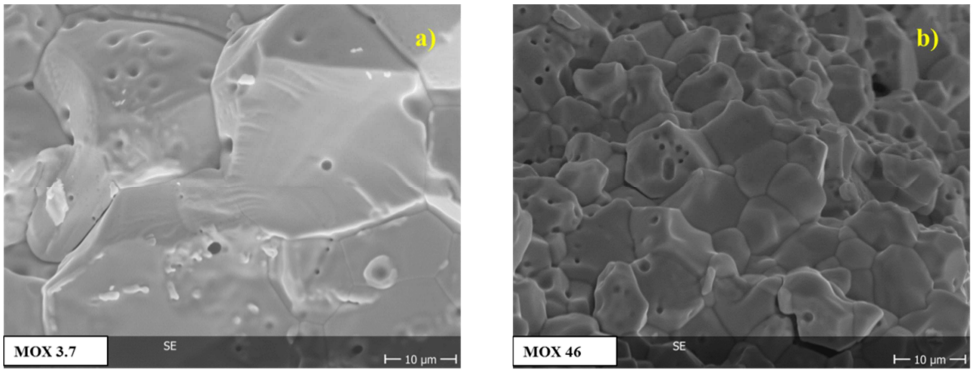

Fig. 3.5.6. SEM images obtained for a) MOX 3 and b) MOX 46, after the 250ºC heat treatment.

Figure 3.5.6 shows that grains in both MOX 3.7 and MOX 46 are large (≥ 10 µm) and regular after the 250ºC heat treatment, suggesting that no significant microstructural evolution has taken place, in good agreement with Raman results. Nevertheless, MOX 3.7 grains seem to be slightly swollen (see pores

surroundings in Figure 3.5.6a), what might be ascribed to the minor superficial oxidation previously noticed by Raman spectroscopy for this sample.

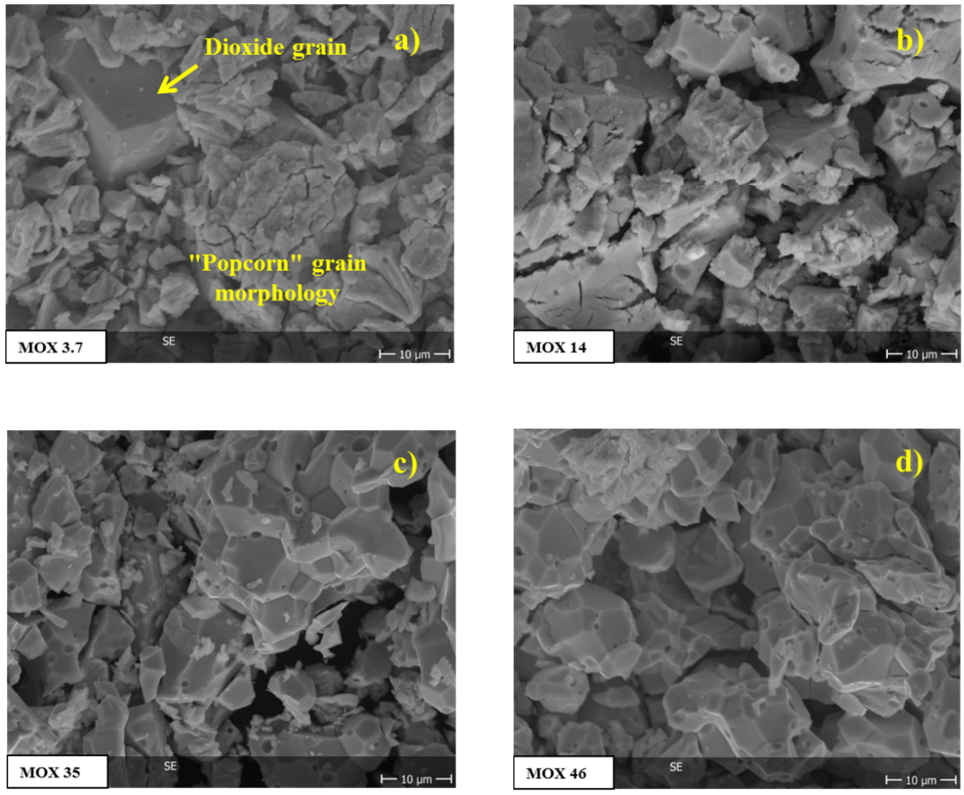

Fig. 3.5.7. SEM images obtained for a) MOX 3, b) MOX 14, c) MOX 35 and d) MOX 46, after the 400ºC heat treatment.

On the other hand, the sequence of images presented in Figure 3.5.7 fairly depicts the hindering effect of Pu on the dioxide matrix oxidation, as observed by Raman and XRD. After subjecting them to 400ºC during 3 hours, each MOX sample exhibits a different surface aspect. If one compares Figure 3.5.7a with Figure 3.5.6a, it is evident that larger – most likely cubic – grains of MOX 3.7 appear to be covered by a superficial layer of M_3O_8, commonly associated with a so-called "popcorn" effect [1]. A similar popcorn morphology can be partly seen also in MOX 14 (Figure 3.5.7b), which also shows considerably swollen and cracked grains (both inter and intragranularly). MOX 35 presents intergranular cracking only, with some swollen areas located in the openings originated by this

effect. MOX 46 looks similar to MOX 35, although with a more compact aspect, indicating a lower loss of integrity might have taken place.

This qualitative analysis of the crystal grain aspect in various MOX samples shows an evolution of the sample surface morphology, which is in line with the trend derived from Raman spectroscopy analyses, *i.e.* the lower the Pu content, the larger the oxidation effects.

3.5.4. Conclusions

The surface oxidation of the matrix in a variety of uranium-plutonium mixed dioxides has been analysed by Raman spectroscopy under different temperature conditions, thereby assessing the effect of Pu content.

In the case of MOX samples subjected to 250°C during 3 hours, no significant oxidation has been observed in any of the Raman spectra, except for the slight appearance of U_3O_8 traces in pure UO_2. Higher temperatures are needed in order to trigger appreciable chemical reactions between oxygen and the present samples. However, for all other heat treatments (310, 340 and 400°C) oxidation does occur and the obtained data point out that a higher proportion of Pu slows down the dioxide matrix oxidation. In fact, M_4O_9 is observed as the intermediate stable phase in every MOX sample before oxidising to M_3O_8. XRD measurements and SEM images are in good agreement with Raman results, confirming the stabilising effect of Pu^{4+} on the fcc dioxide structure.

The present study therefore shows, with the sole help of Raman spectroscopy, that (U, Pu) mixed dioxides are subject to further oxidation in air starting at a temperature between 250°C and 310°C, at least on a time scale of several hours.

In any case, this work demonstrates that Raman spectroscopy is highly reliable for evaluating the uranium-plutonium dioxide fuel oxidation, since its transformation to M_4O_9 or M_3O_8 can be easily and quickly monitored with this technique.

In addition, thanks also to its intrinsically non-contact nature and versatility, Raman spectroscopy can be envisaged as a suitable technique for the analysis of the oxidation behaviour of spent nuclear fuel, in case of shielding failure, under interim storage conditions.

3.5.5. Acknowledgements

This work was carried out within the collaboration framework established between CIEMAT and EC-JRC Karlsruhe (*Collaboration Agreement Nº 34231* and *User Access Agreement Nº 930009*), and supported by the *Graduate and Executive Nuclear Training and Longlife Education* (GENTLE) project (EURATOM FP7 contract number 323304). The authors are indebted to J.-Y. Colle, M. Sierig and E. Dahms (JRC Karlsruhe) for their help in the samples characterisation and the Raman measurements.

3.5.6. References

[1] R. J. McEachern and P. Taylor, *J. Nucl. Mater.*, **254**, 87-121 (1998).
[2] G. Rousseau, L. Desgranges, F. Charlot, N. Millot, J.C. Nièpce, M. Pijolat, F. Valdivieso, G. Baldinozzi and J. F. Berar, *J. Nucl. Mater.*, **355**, 10-20 (2006).
[3] L. Desgranges, G. Baldinozzi, G. Rousseau, J. C. Nièpce and G. Calvarin, *Inorg. Chem.*, **48**, 7585-7592 (2009).
[4] H. He and D. Shoesmith, *Phys. Chem. Chem. Phys.*, **12**, 8108-8117 (2010).
[5] J. M. Elorrieta, L. J. Bonales, N. Rodriguez-Villagra, V. G. Baonza and J. Cobos, *Phys. Chem. Chem. Phys.*, **12**, 8108-8117 (2016).
[6] R. I. Cooper and B. T. M. Willis, *Acta Cryst. A*, **60**, 322 (2004).
[7] K. Fukuda, J.-S. Choi, R. Shani, L. van den Durpel, E. Bertel and E. Sartori (2000). *MOX fuel use as a back-end option: Trends, main issues and impacts on fuel cycle management* (IAEA-CSP--3/P). International Atomic Energy Agency (IAEA).
[8] V. J. Tennery and T. G. Godfrey, *J. Am. Ceram. Soc.*, **56**, 129-133 (1973).
[9] N. C. Jayadevan, R. G. Hadap and D. M. Chackraburtty, *J. Nucl. Mater.*, **82**, 195-198 (1979).
[10] T. Tsuji, M. Iwashita, T. Yamashita and K. Ohuchi, *J. Alloys Compd.*, **271-273**, 391-394 (1998).
[11] P. Martin, S. Grandjean, C. Valot, G. Carlot, M. Ripert, P. Blanc and C. Hennig, *J. Alloys Compd.*, **444-445**, 410-414 (2007).
[12] R. C. Belin, M. Strach, T. Truphémus, C. Guéneau, J. -C. Richaud and J. Rogez, *J. Nucl. Mater.*, **465**, 407-417 (2015).
[13] R. Vauchy, A.-C. Robisson, R. C. Belin, P. M. Martin, A. C. Scheinost, F. Hodaj, *J. Nucl. Mater.*, **465**, 349-357 (2015).

[14] J. F. Vigier, P. M. Martin, L. Martel, D. Prieur, A. C. Scheinost and J. Somers, *Inorg. Chem.*, **54 (11)**, 5358-5365 (2015).
[15] M. Strach, R. C. Belin, J. -C. Richaud and J. Rogez, *Inorg. Chem.*, **53**, 12757-12766 (2014).
[16] M. Strach, R. C. Belin, J. -C. Richaud and J. Rogez, *J. Phys. Chem.C*, **119 (40)**, 23159-23167 (2015).
[17] T. Truphémus, R. C. Belin, J. -C. Richaud, M. Reynaud, M. -A. Martínez, I. Félines, A. Arredondo, A. Miard, T. Dubois, F. Adenot and J. Rogez, *J. Nucl. Mater.*, **432**, 378-387 (2013).
[18] C. Jégou, R. Caraballo, J. De Bonfils, V. Broudic, S. Peuget, T. Vercouter and D. Roudil, *J. Nucl. Mater.*, **399**, 68-80 (2010).
[19] Z. Talip, S. Peuget, M. Magnin, L. Berardo, C. Valot, R. Vauchy and C. Jégou, *J. Raman Spectrosc.*, **48 (5)**, 765-772 (2017).
[20] C. Jégou, R. Caraballo, S. Peuget, D. Roudil, L. Desgranges and M. Magnin, *J. Nucl. Mater.*, **405**, 235-243 (2010).
[21] C. Jégou, M. Gennisson, S. Peuget, L. Desgranges, G. Guimbretière, M. Magnin, Z. Talip and P. Simon, *J. Nucl. Mater.*, **458**, 343-349 (2015).
[22] R. Böhler, M. J. Welland, D. Prieur, P. Cakir, T. Vitova, T. Pruessmann, I. Pidchenko, C. Hennig, C. Guéneau, R. J. M. Konings and D. Manara, *J. Nucl. Mater.*, **448**, 330-339 (2014).
[23] L. J. Bonales, J. M. Elorrieta, A. Lobato and J. Cobos, *Raman Spectroscopy, a Useful Tool to Study Nuclear Materials*, Applications of Molecular Spectroscopy to Current Research in the Chemical and Biological Sciences, Dr. Mark Stauffer (Ed.), InTech (2016). ISBN 978-953-51-2681-2.
[24] F. Pointurier and O. Marie, *Spectrochim. Acta B*, **65**, 797-804 (2010).
[25] E. A. Stefaniak, A. Alsecz, I. E. Sajó, A. Worobiec, Z. Máthé, S. Török and R. Van Grieken, *J. Nucl. Mater.*, **381**, 278-283 (2008).
[26] L. Desgranges, G. Baldinozzi, P. Simon, G. Guimbretière and A. Canizares, *J. Raman Spectrosc.*, **43**, 455-458 (2012).
[27] G. Guimbretière, L. Desgranges, A. Canizares, G. Carlot, R. Caraballo, C. Jégou, F. Duval, N. Raimboux, M. R. Ammar and P. Simon, *Appl. Phys. Lett.*, **100**, 251914 (2012).
[28] D. Ho Mer Lin, D. Manara, P. Lindqvist-Reis and T. Fanghänel, *Vib. Spectrosc.*, **73**, 102-110 (2014).
[29] M. Naji, N. Magnani, L. J. Bonales, S. Mastromarino, J.-Y. Colle, J. Cobos and D. Manara, *Phys. Rev. B*, **95**, 104307 (2017).
[30] M. J. Sarsfield, R. J. Taylor, C. Puxley and H. M. Steele, *J. Nucl. Mater.*, **427**, 333-342 (2012).

[31] M. Naji, J.-Y. Colle, O. Benes, M. Sierig, J. Rautio, P. Lajarge and D. Manara, *J. Raman Spectrosc.*, **46**, 750-756 (2015).
[32] F. Lebreton, D. Horlait, R. Caraballo, P. M. Martin, A. C. Scheinost, A. Rossberg, C. Jégou and T. Delahaye, *Inorg. Chem.*, **54 (20)**, 9749-9760 (2015).
[33] D. Horlait, R. Caraballo, F. Lebreton, C. Jégou, P. Roussel and T. Delahaye, *J. Solid State Chem.*, **217**, 159-168 (2014).
[34] M. Chollet, D. Prieur, R. Böhler, R. Belin and D. Manara, *J. Chem. Thermodyn.*, **89**, 27-34 (2015).
[35] H. Richter, Z. Wang, and L. Ley, *Solid State Commun.*, **39**, 625 (1981).
[36] V. Petříček, M. Dušek and L. Palatinus, *Z. Kristallogr.*, **229**, 345-352 (2014).
[37] S. Amelinckx, D. van Dyck, J. van Landuyt and G. van Tendeloo, *Handbook of Microscopy, Applications in Materials Science, Solid-State Physics and Chemistry, in: Applications*, VCH Verlagsgesellschaft mbH, Weinheim (1997).
[38] T. Wiss, H. Thiele, A. Janssen, D. Papaioannou, V. V. Rondinella and R. J. M. Konings, *JOM*, **64**, 1390–1395 (2013).
[39] P. G. Marlow, J. P. Russell and J. R. Hardy, *Philos. Mag.*, **14**, 409-410 (1966).
[40] T. Livneh and E. Sterer, *Phys. Rev. B*, **73**, 085118-085119 (2006).
[41] G. C. Allen, I. S. Butler and N. A. Tuan, *J. Nucl. Mater.*, **144**, 17-19 (1987).
[42] P. R. Graves, *Appl. Spectrosc.*, **144**, 1665-1667 (1990).
[43] M. L. Palacios and S. H. Taylor, *Appl. Spectrosc.*, **54**, 1372-1378 (2000).
[44] D. Manara and B. Renker, *J. Nucl. Mater.*, **321**, 233-237 (2003).
[45] L. Desgranges, G. Guimbretière, P. Simon, C. Jégou and R. Caraballo, *Nucl. Instrum. Methods Phys. Res. Sect. B*, **315**, 169-172 (2013).
[46] Q. Yin and S. Y. Savrasov, *Phys. Rev. Lett.*, **100**, 225504 (2008).
[47] G. Talsky, *Derivative Spectrophotometry: Low and High Order*, Verlagsgesellschaft, Weinheim (Federal Republic of Germany) and Inc., New York, NY (USA), 1994. ISBN 3-527-28294-7.
[48] L. Genzel, T. P. Martin and C. H. Perry, *Phys. Stat. Sol.(b)*, **62**, 83-92 (1974).
[49] I. S. Butler, G. C. Allen and N. A. Tuan, *Appl. Spectrosc.*, **42 (5)**, 901-902 (1988).
[50] G. Leinders, T. Cardinaels, K. Binnemans and M. Verwerft, *J. Nucl. Mater.*, **459**, 135-142 (2015).
[51] L. Martel, N. Magnani, J.-F. Vigier, J. Boshoven, C. Selfslag, I. Farnan, J.-C. Griveau, J. Somers and T. Fanghänel, *Inorg. Chem.*, **53**, 6928-6933 (2014).
[52] C. Guéneau, A. Chartier and L. Van Brutzel, *Compr. Nucl. Mater.*, **2**, 21–59 (2012).

Result 6

Ce effect on (U, Ce)O_2 oxidation: is it an adequate surrogate for Pu?

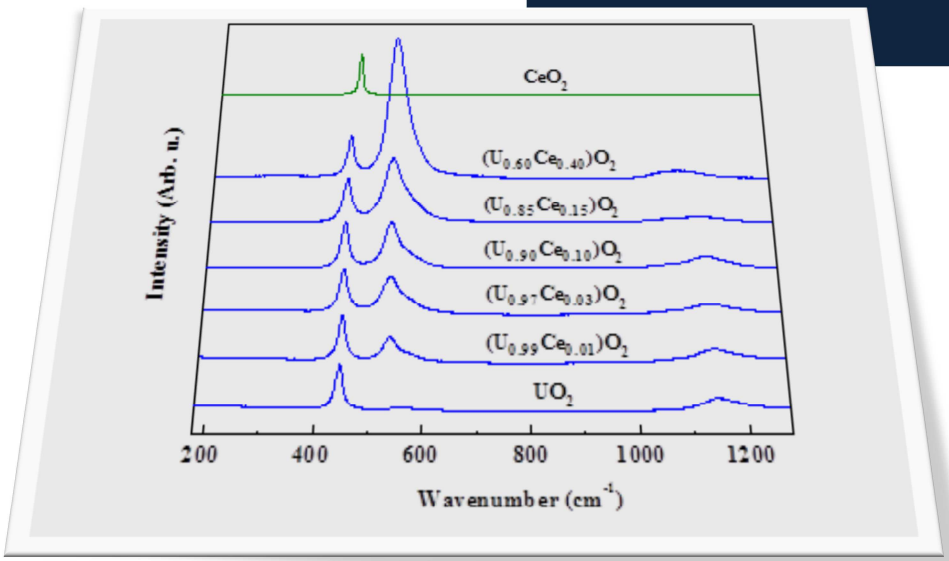

Published as "Pre- and post-oxidation Raman analysis of (U, Ce)O_2 oxides", **J. M. Elorrieta, L. J. Bonales, S. Fernández, N. Rodríguez-Villagra, L. Gutiérrez-Nebot, V. G. Baonza and J. Cobos**, *J. Nucl. Mater.* (2018). (Submitted)

Abstract

A pre- and post-oxidation detailed Raman analysis has been carried out on a variety of (U_{1-y},Ce_y)O_2 stoichiometries (y = 0.01, 0.03, 0.10, 0.15, 0.40). The changes undergone in the Raman spectrum of UO_2 as a function of Ce incorporation have been examined, thus extracting valuable information on the structural features and changes of these solid solutions, including the presence of vacancies in the cations' surroundings. Comparison of the results extracted from the post-oxidation analyses of Ce-containing samples with those obtained for pure UO_2 confirms that a Ce content as low as 1 mol% leads to a protective effect on the dioxide matrix against oxidation and that, under identical conditions, the oxidation process is slowed down as Ce concentration increases.

3.6.1. Introduction

Uranium-cerium mixed oxides deserve special attention when addressing the stability of uranium-based spent nuclear fuel. This is not only because Ce is one of the fission products that is present in greater proportion in this type of fuel [1], but also because of the frequent use of CeO_2 to simulate highly radioactive PuO_2 in the MOX fuel [2-4].

CeO_2 and UO_2 have similar structural properties, presenting both fluorite-type cubic ordering, which promotes the formation of solid solutions when combined [2-5]. In such (U, Ce)O_2 mixed oxides, charge transfer between U^{4+} and Ce^{4+} ions has been widely reported [1,6-9]. While uranium tends to oxidise (up to U^{5+} and U^{6+}), cerium tends to reduce to its lower oxidation state (Ce^{3+}). The proportion of each chemical state of U and Ce in a given (U, Ce)O_2 oxide is strongly dependent on Ce content, as observed by Bera *et al.* in their detailed XPS analysis [1]. These authors suggested that reduction from Ce^{4+} to Ce^{3+} results in the creation of defects, specifically in the form of stable oxygen vacancies.

To understand the oxidation behaviour of (U, Ce)O_2 and to explain how the chemical states of U and Ce evolve during this reaction, a couple of studies have been carried out at high temperatures (> 500ºC), mainly focused on X-ray diffraction data [2,4]. In these studies, an oxidation hindering effect has been

observed as Ce content increases. For instance, in both cases [2,4], for $y < 0.4$ –in $(U_{1-y}Ce_y)O_2$– oxidation of the solid solutions leads to a mixture of an orthorhombic M_3O_8 phase (M=U,Ce) and a cubic M_4O_9 or MO_{2+x} phase, while for $y > 0.4$ M_3O_8 is no longer observed. In addition, Kumar *et al.* [4] detected the sole presence of Ce^{4+} ions in the oxidised samples, what might indicate that the initially existing oxygen vacancies disappear before uranium oxidation begins.

Despite the valuable information that could be extracted from Raman spectroscopy, especially with regard to the monitoring of oxygen vacancies observed on other mixed oxides [10-14], there is only one study that applies this technique to acquire a better understanding of uranium-cerium dioxides [15]. Furthermore, there is no account of Raman analyses on their oxidation products. Therefore, this paper presents for the first time a thorough Raman characterisation of a variety of (U, Ce)O_2 oxides, paying special attention to the evolution of the UO_2 Raman spectrum as Ce content increases, with the aim of understanding the changes occurring due to the incorporation of Ce. In addition, a post-oxidation Raman analysis is also addressed, in particular by comparing the spectra corresponding to the different oxidised samples to show the sensitivity of this technique to detect the influence of Ce concentration on the oxidation of mixed dioxides.

3.6.2. Experimental

3.6.2.1. Sample preparation

The starting UO_2 and CeO_2 powders, both with an average particle size of ~15 µm, were provided by ENUSA and Alfa Aesar, respectively. These materials were mixed in the intended proportions, together with 3% w/w of EBS (Ethyl Bis Stearamide, supplied by Tokyo Chemical Industry Co.) as binder and lubricant [16], using low-energy ball milling. Following a conventional metallurgical procedure, the mixtures obtained were subjected to uniaxial pressing at 700 MPa. Subsequently, a heating process under a N_2-4.7%H_2 flow –in order to avoid UO_2 oxidation– was conducted on all the green pellets, applying four consecutive steps: three isotherms at 100ºC (2 hours), 300ºC (4 hours) and 500ºC (4 hours) for calcination of the incorporated EBS, followed by the sintering isotherm at 1600ºC for 4 hours. The binder proportion used, applied pressure and sintering cycle were established elsewhere [17] and adapted to this study. Polishing and thermal annealing were then carried out, which consisted in a 10 minutes

treatment at 1520ºC (95% of the sintering temperature) under the same N_2-4.7%H_2 atmosphere. As a result, a series of $(U_{1-y}Ce_y)O_2$ homogeneous solid solutions, with y = 0.01, 0.03, 0.10, 0.15 and 0.40, were obtained. The undoped UO_2 disk used as a reference was also supplied by ENUSA, while pure CeO_2 characterised for extrapolation was previously fabricated following the procedure reported in Ref. 17.

3.6.2.2. Oxidation procedure

The oxidation of the UO_2 and (U, Ce)O_2 samples was performed by a Linkam THMS600 temperature controlled stage. The mechanical design and electronics of the Linkam stage provided precise control and stability of the temperature better than 0.2 degrees. A 10°C/min heating ramp was applied to reach the isothermal temperature, 350ºC, which was then maintained for 3 hours. A dry air flow was supplied throughout the process. Cooling was subsequently conducted with the help of the in-house refrigeration system.

3.6.2.3. Characterisation techniques

X-ray diffraction measurements on the mixed oxides were carried out by a Bruker D8 Advance Eco diffractometer, using Cu Kα radiation (λ = 1.54056 Å) and operating at 40 kV and 25 mA. The Bragg-Brentano configuration geometry was used.

Raman spectroscopy analyses were performed with a Horiba LabRAM HR Evolution spectrometer. All spectra were acquired at an excitation wavelength of 632.8 nm provided by a He-Ne laser. The scattered radiation was then collected in backscattering geometry, dispersed using a 600 grooves/mm holographic grating and recorded using a CCD detector (256 x 1024 pixels), obtaining a ~1 cm^{-1}/pixel spatial resolution and a spectral resolution of better than 3 cm^{-1}. The obtained spectra were calibrated with the emission lines of a Ne lamp. The scattered radiation was collected through a 100x objective for characterisation of the pre-oxidation samples, while a 50x long focal distance objective was used to probe the oxidised samples in order to average the signal and to minimise the effect of the surface irregularities formed during oxidation. In all cases, the excitation power was minimised to avoid alteration of the samples.

3.6.3. Results and discussion

3.6.3.1. Pre-oxidation characterisation

Prior to oxidation, a systematic X-ray diffraction and Raman characterisation of all samples was performed. Figure 3.6.1 shows the values of the lattice parameters measured for the undoped UO_2 disk and the sintered $(U_{1-y}Ce_y)O_2$ oxides ($0.01 \leq y \leq 0.40$), assuming that the cubic structure of UO_2 prevails. The estimated lattice parameter value for pure CeO_2, which is consistent with literature values [18], has also been included.

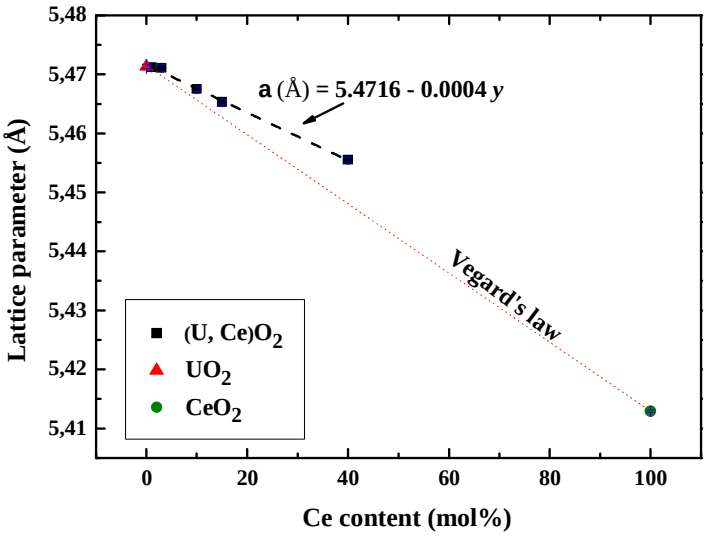

Fig. 3.6.1. Lattice parameter values estimated for pure UO_2 and the sintered $(U_{1-y}Ce_y)O_2$ oxides, with $0.01 \leq y \leq 0.40$. The lattice parameter value obtained for pure CeO_2 is also included.

A steady contraction of the lattice parameter is observed as Ce content increases (dashed line and equation inserted in Figure 3.6.1), as is expected from the partial substitution of U^{4+} ions by the smaller Ce^{4+} ions [19]. However, these data do not follow Vegard's law, as they do not fall on a straight line between the pure UO_2 and CeO_2 values (dotted line in Figure 3.6.1). Some of the earlier studies on (U, Ce)O_2 oxides were in good agreement with Vegard's law [19,20] and attributed such behaviour to a near-stoichiometric state of their oxides [20]. In our case, an increasing deviation towards higher lattice parameter values, with regard to those predicted by Vegard's law, is observed as a function of Ce

content. This would therefore imply that formation of stable oxygen vacancies had occurred in our samples, most likely related to an increasing presence of Ce^{3+} ions [1] (presenting larger atomic radii than Ce^{4+} ions [21]), leading to an expansion of the lattice (*e.g.* ~0.4 % for 40 mol% of Ce) [22].

Results of Raman characterisation are shown in Figure 3.6.2. Each spectrum actually consists of the average of 10 spectra acquired on different spots of the corresponding dioxide surface, with the aim of both confirming the samples homogeneity and enhancing the signal-to-noise ratio of the final spectra. In general terms, the UO_2 Raman spectrum presents its two well-reported main features at ~445 cm^{-1} (T_{2g} mode) and ~1150 cm^{-1} (2LO phonon overtone) [23,24]. As for the Ce-containing samples, a remarkable additional feature is observed around 500-600 cm^{-1}, which continuously increases in intensity with increasing Ce content. Indeed, this feature grows in such a way that it even exceeds the intensity of the other bands at high doping concentrations. The Raman spectrum of pure CeO_2, on the other hand, shows the expected single T_{2g} mode at 465 cm^{-1} [25].

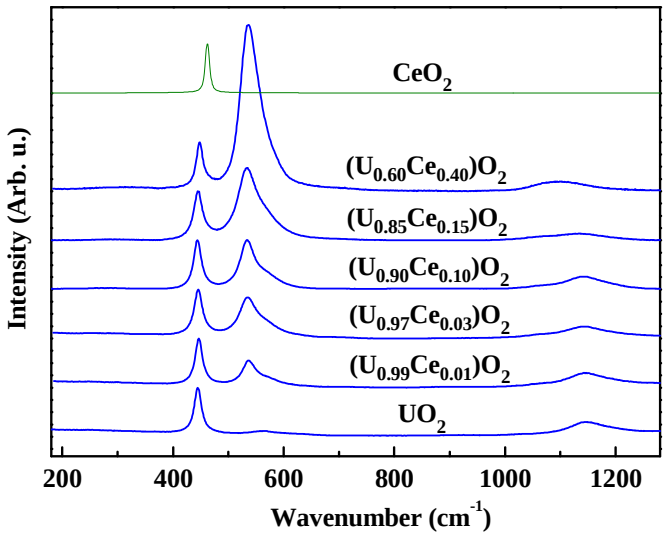

Fig. 3.6.2. Raman spectra of pure UO_2 and CeO_2 and the sintered $(U_{1-y}Ce_y)O_2$ oxides, with $0.01 \leq y \leq 0.40$.

In order to better examine the spectra evolution as a function of Ce incorporation within the UO_2 fluorite-like structure, a detailed peak-profile analysis was conducted making use of Lorentzian bandshapes. Figure 3.6.3

shows the UO_2 and (U, Ce)O_2 Raman spectra with the different contributions extracted from their corresponding profile fitting. The resulting fitted profiles are also shown for comparison purposes.

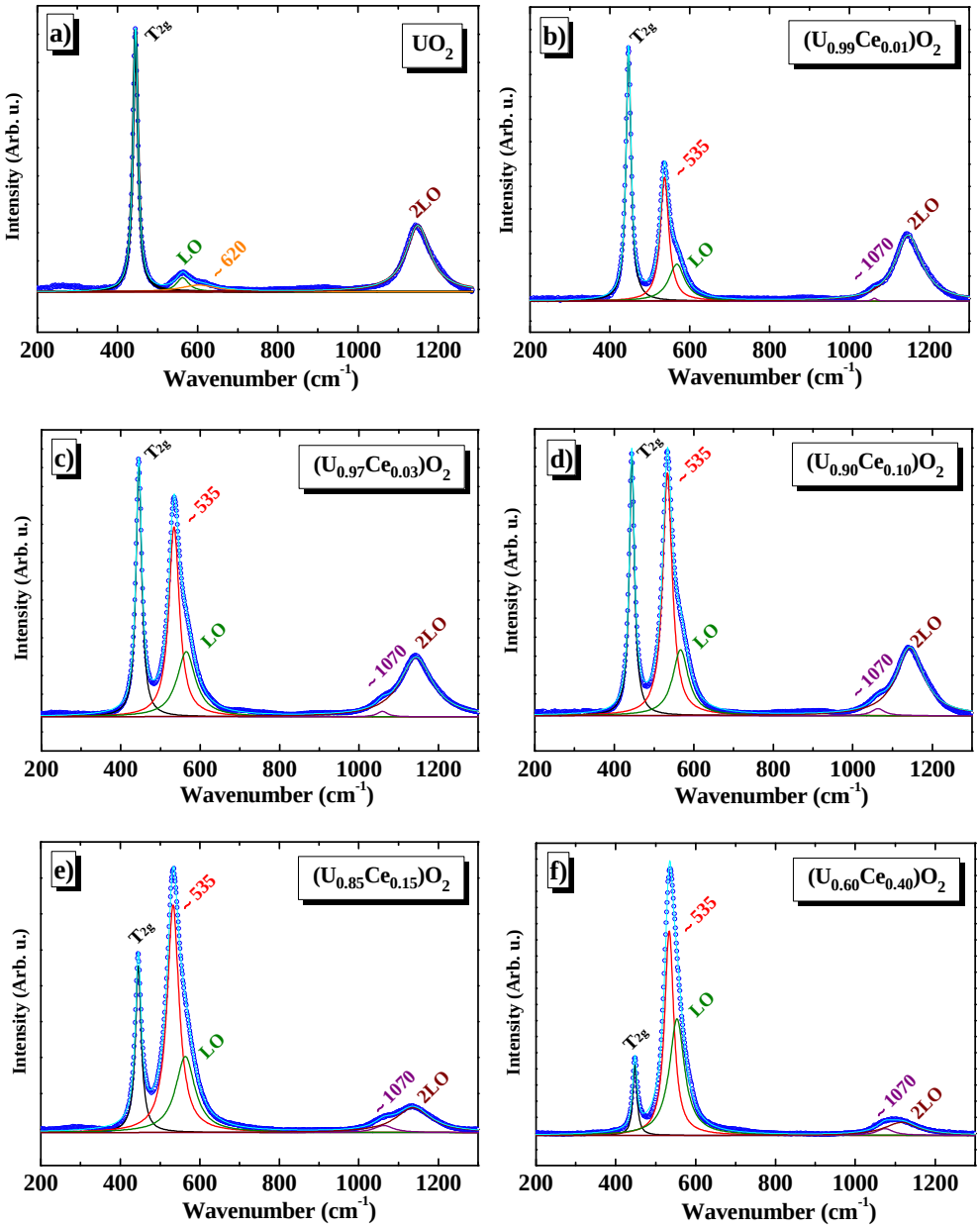

Fig. 3.6.3. Profile analysis of the different $(U_{1-y}Ce_y)O_2$ Raman spectra ($0 \leq y \leq 0.4$).

In the case of pure UO_2, apart from the T_{2g} and 2LO characteristic bands, two weak bands are observed at ~575 cm^{-1} and ~620 cm^{-1} (see Figure 3.6.3a), which are usually associated with lattice defects [26-29]. In particular, some studies have assigned a band at ~575 cm^{-1} to the LO mode and its observation has been related to a breakdown in the selection rules due to lattice distortions [27,28]. Likewise, a band around 620-630 cm^{-1} has often been attributed to oxidation, more precisely to cuboctahedral clusters formation due to further oxidation to U_4O_9 [27-30]. The appearance of the latter features in the UO_2 spectrum might thus indicate that a minor surface oxidation affects slightly the lattice ordering. In accordance with the experimental equations published elsewhere [29], the oxidation degree of such hyperstoichiometric UO_{2+x} would roughly correspond to $x \sim 0.07$.

Raman spectra shown in Figures 3.6.3b-3.6.3f correspond to Ce-containing samples and present five bands. In addition to T_{2g}, LO and 2LO peaks, two features are observed around 535 cm^{-1} and 1070 cm^{-1}; but in this case the ~620 cm^{-1} band is not observed, thus indicating that not even surface oxidation has been produced.

A single-peak contribution is noticed for the T_{2g} band of all the mixed oxides, what ascertains that it follows a one-mode vibration model, as expected for heavy metal dioxides mixtures [31,32]. The variation of this band position with Ce content has been quantitatively analysed in Figure 3.6.4 and compared to the expected values (dotted line in Figure 3.6.4), which have been calculated taking into account the influence on the T_{2g} Raman shift of the changes produced in both the reduced mass and force constant by Ce incorporation. The force constant dependency on the interatomic distance has been modelled using the Guggenheimer model as described by Jules and Lombardi [33].

As can be seen, a small upshift is detected, just ~3 cm^{-1} up to $(U_{0.60}Ce_{0.40})O_2$ instead of the slightly larger move that should be observed if assuming a one-mode behaviour, where the T_{2g} band would upshift on a proportional basis as Ce concentration increases, from pure UO_2 to CeO_2 corresponding wavenumbers [34]. For instance, this is what occurs in the case of $(U,Pu)O_2$: the T_{2g} band, which presents one-mode vibration behaviour [35-38], shifts towards higher wavenumbers between its position in UO_2 and that in PuO_2 as a function of Pu content [37,38]. The observed small upshift for $(U,Ce)O_2$ oxides was already noticed by Ravindran and Krishnan [15], who reported it to be “only of the order of 5 cm^{-1} over 80 at.% substitution of cerium”. These authors did not provide any

explanation, but claimed that the contrast observed with regard to (U, Pu)O_2 indicates a quite different effect of Pu and Ce on UO_2. We suggest that the contribution of Ce^{4+}-O bonds, which are shorter [19] and hence stiffer than U-O bonds in the fluorite-like structure, is partially balanced with the weakness produced by the presence of stable oxygen vacancies in the surroundings of Ce^{3+} atoms, as also deduced from the X-ray diffraction analysis.

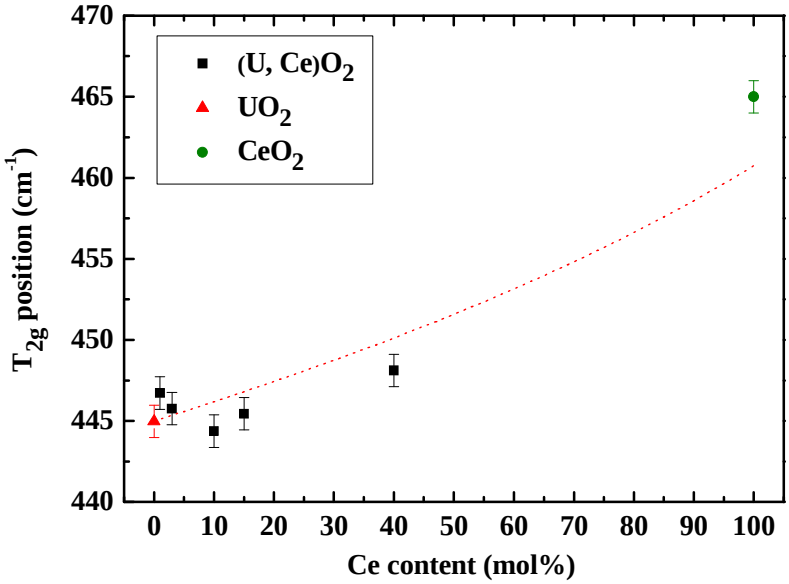

Fig. 3.6.4. T_{2g} band position of the characterised $(U_{1-y}Ce_y)O_2$ oxides as a function of Ce content ($0.01 \leq y \leq 0.4$). The corresponding values obtained for pure UO_2 and CeO_2 are also included. The dotted line represents the expected values according to changes in both force constants (interatomic distance) and reduced mass.

Furthermore, since various studies have associated a peak observed around 530-540 cm^{-1} with the presence of oxygen vacancies [10-14,28], the occurrence of a band at ~535 cm^{-1} in the mixed oxides spectra (Figures 3.6.3b-3.6.3f) would confirm the reported presence of Ce^{3+} ions that lead to creation of stable oxygen vacancies [1]. On the other hand, to the best of our knowledge, no mention to the band found at ~1070 cm^{-1} has been made in the literature before. Indeed, these two new bands in the spectra of Ce-containing samples seem to continuously grow with the increase in Ce content, especially the one at ~535 cm^{-1}, what corroborates the increasing presence of Ce^{3+} atoms that lead to a growing amount of oxygen vacancies. Such evolution has been quantitatively estimated by analysing, as a function of Ce content, the area ratio of both bands with respect to

that of the T_{2g} band (A_{535}/A_{T2g} and A_{1070}/A_{T2g}). As can be seen in Figure 3.6.5, the two bands experiment a linear growth with the increase in Ce content. This parallel behaviour, as well as the fact that the wavenumber value of the ~1070 cm^{-1} band is precisely twice the one corresponding to the ~535 cm^{-1} band, suggest that the ~1070 cm^{-1} band is actually the first overtone of the latter band.

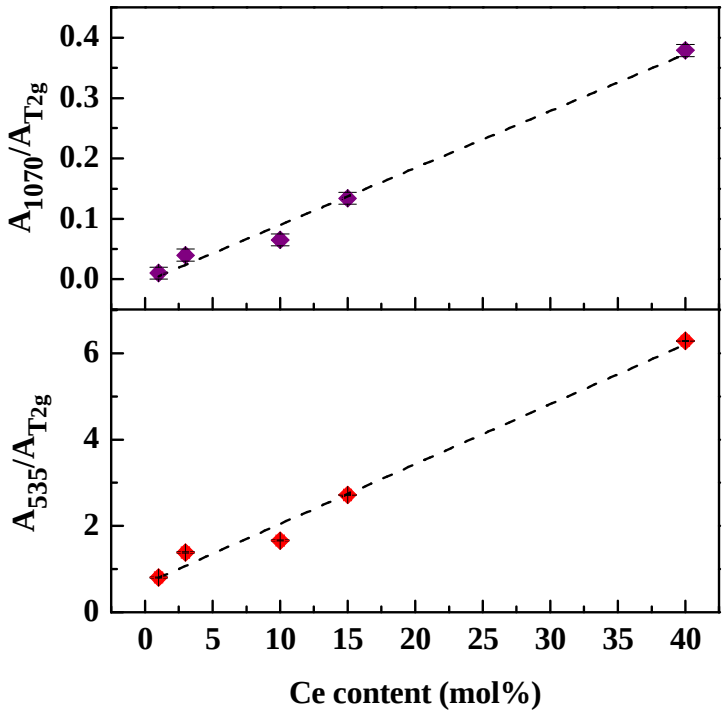

Fig. 3.6.5. Evolution with Ce content of the normalised area, with respect to the T_{2g} band, of the ~535 cm^{-1} and ~1070 cm^{-1} bands.

3.6.3.2. Post-oxidation characterisation

After the air oxidation treatment, which consisted in the 10°C/min heating ramp and the subsequent three hours isotherm at 350ºC, a detailed Raman spectroscopy analysis was performed on all the oxidised $(U_{1-y}Ce_y)O_2$ specimens ($0 \leq y \leq 0.40$) in order to examine the influence of Ce content in the dioxide oxidation.

Except for pure UO_2, where complete oxidation to U_3O_8 was detected in various zones of the sample surface as shown in Figure 3.6.6, the intermediate

M_4O_9 phase (M=U,Ce) was found to stabilise in all cases [30]. This is reflected in Figure 3.6.7, which gathers the spectra acquired for the different uranium-cerium mixed oxides, as well as for UO_2 on the zones that had not been completely turned into U_3O_8 (light areas in Figure 3.6.6a). Again, each Raman spectrum consists of the sum of ~10 similar spectra obtained on distinct spots of the corresponding dioxide surface. The various contributions extracted from the peak-profile analysis of these Raman spectra over the 350-750 cm^{-1} range are included.

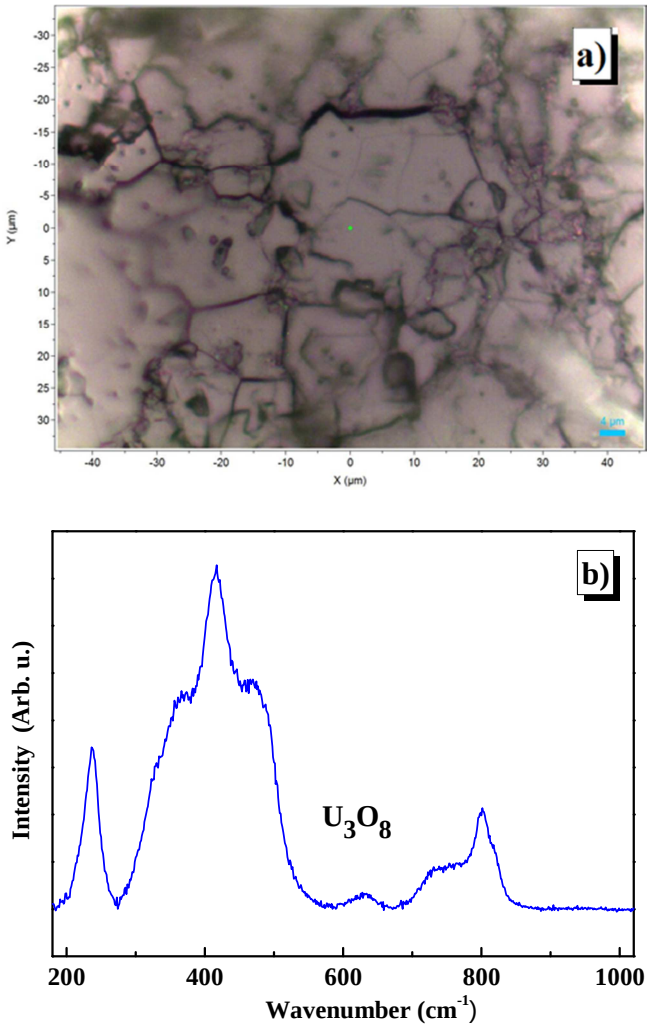

Fig. 3.6.6. a) Optical image of the oxidised UO_2 sample surface. b) Typical Raman spectrum of U_3O_8 [39,40],acquired on the dark shiny areas in a).

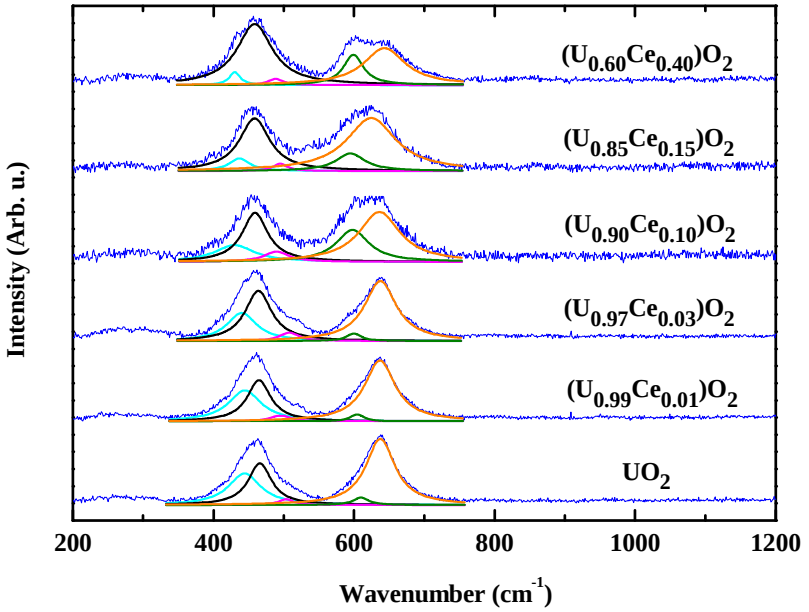

Fig. 3.6.7. Raman spectra corresponding to the oxidised $(U_{1-y}Ce_y)O_2$ samples ($0 \leq y \leq 0.4$). Lorentzian peaks obtained from their profile analysis are also plotted.

In this way, each oxide features the same five bands over the studied range. The three peaks observed at ~435, ~460 and ~495 cm^{-1} might correspond to the triplet (A_{1g}, A_{1g} and E_g modes, respectively) originated by the splitting of the triply degenerate T_{2g} band due to symmetry loss, as occurs when it is transformed to the orthorhombic U_3O_8 phase [39,40]. The other peaks located at ~605 and ~635 cm^{-1} seem to be the LO and oxidation-related bands, accordingly, although now considerably shifted with respect to their pre-oxidation positions. Indeed, Desgranges *et al.* observed in U_4O_9 a similar broad band centred on ~630 cm^{-1} which they associated with oxidation [30].

Therefore, an oxidation degree comparison of the treated (U, Ce)O_2 oxides was carried out by analysing the area ratio of the ~635 cm^{-1} band with respect to that of the T_{2g} band (A_{635}/A_{T2g}) in each case. The ~460 cm^{-1} peak was taken as a reference of T_{2g} for the analysis, since it is the most representative among the triplet if considering a single broad T_{2g} band. As can be seen in Figure 3.6.8a, the latter area ratio decreases in general terms as a function of Ce content, suggesting the detection of higher oxidation degrees on U-richer samples. For greater reliability, the T_{2g} band shift undergone by every oxide, with regard to its

corresponding pre-oxidation position, was also examined. This method allows us to extract the oxidation contribution, as previously performed on heat treated (U, Pu)O_2 oxides [38]. Figure 3.6.8b shows how the studied shift is continuously smaller, and thus the oxidation degree lower, as Ce concentration increases, in good agreement with the results obtained from the preceding analysis.

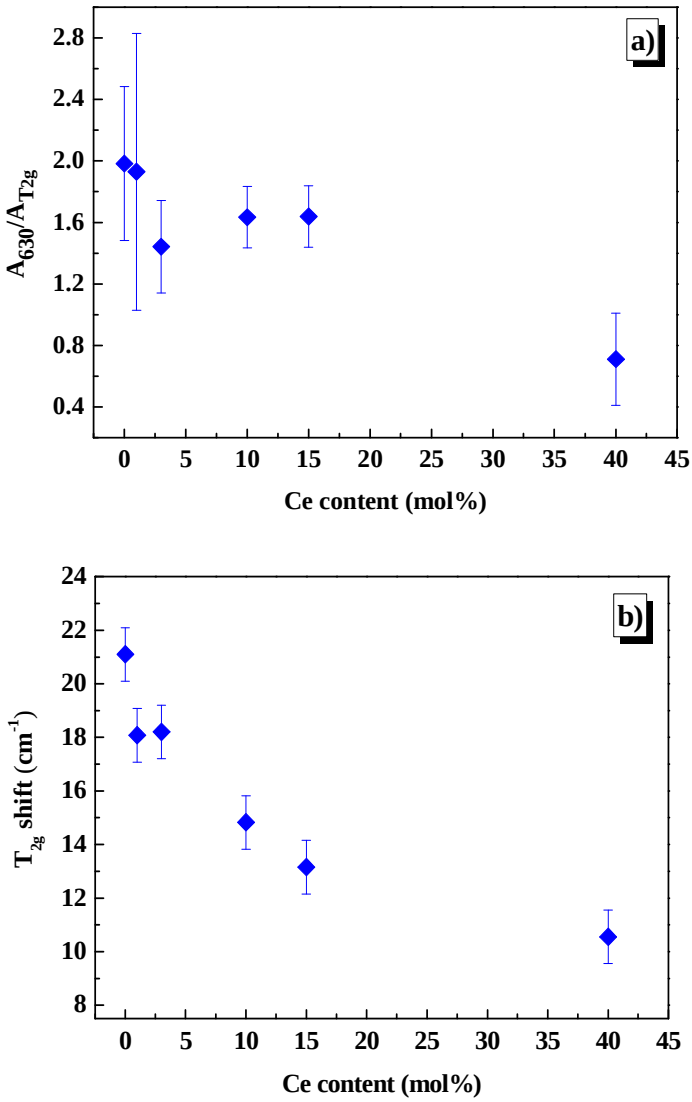

Fig. 3.6.8. a) Evolution of the normalised area –with respect to T_{2g} band– of the ~630 cm^{-1} oxidation-related peak and b) T_{2g} band shift due to oxidation, as a function of Ce content.

The latter tendency, observed by the sole means of Raman spectroscopy in this work, is in line with the previously noticed hindering effect on (U, Ce)O_2 oxidation caused by the increasing presence of Ce [2,5], what might be attributed to a diminished oxygen mobility in the contracted lattice. In addition, unlike UO_2, Ce-containing dioxides presented no trace of further oxidation to M_3O_8; not even the one with only 1 mol% substituted. Thus, these Raman results also confirm that the presence of Ce within the UO_2 lattice helps to preserve the dioxide integrity longer, *i.e.* to resist the formation of M_3O_8 [2,5]. A similar effect due to the presence of Pu within the UO_2 fluorite structure has been recently noted [38], pointing out the comparable overall behaviour of (U, Ce)O_2 and (U, Pu)O_2 against oxidation.

3.6.4. Conclusions

Pre- and post-oxidation Raman characterisation has been conducted on various ($U_{1-y}Ce_y$)O_2 oxides, with y = 0.01, 0.03, 0.10, 0.15, 0.40, in order to attain a better understanding of the structural features of these uranium-cerium mixed dioxides.

In this way, previous to oxidation, the evolution of UO_2 Raman spectrum as a function of Ce incorporation has been examined. The linear increase with Ce content of the band related to vacancies, located at ~535 cm^{-1}, confirms the previously reported presence of Ce^{3+} ions. Besides, a new band found at ~1070 cm^{-1} has been proposed as the first overtone of the latter band, since it follows the same growing behaviour with Ce content. The T_{2g} band position has also been studied as a function of Ce concentration, showing a smaller upshift than that expected; a fact that can be interpreted as an evidence of the vacancies influence in the corresponding cations surroundings.

With regard to the oxidised samples analysis, it has been observed that the oxidation degree attained is less significant as Ce concentration increases, what sustains the protective effect of Ce. Furthermore, comparison with pure UO_2 indicates that even 1 mol% Ce doping is sufficient to induce a hindering effect on the dioxide matrix oxidation, resisting M_3O_8 formation and stabilising the M_4O_9 phase on the time scale studied.

Thus, it can be concluded that (U, Ce)O_2 behaves, in general terms, like (U, Pu)O_2, at least with regard to the delay it provokes on the dioxide matrix

oxidation. Nevertheless, care should be taken when comparing them at a local level, since our Raman spectroscopy analysis reveals that the structure of these two materials is not exactly similar. This raises the question as to whether it is certainly adequate to use (U, Ce)O_2 as a surrogate for MOX fuel in research studies.

3.6.5. Acknowledgements

This work was supported by ENRESA within the project Nº 079000189, entitled “Aplicación de técnicas de caracterización en el estudio de la estabilidad del combustible nuclear irradiado en condiciones de almacenamiento” (ACESCO). VGB acknowledges support from MINECO under project CTQ2015-67755-C02-01-R.

3.6.6. References

[1] S. Bera, V. K. Mittal, R. V. Krishnan, T. Saravanan, S. Velmurugan, K. Nagarajan and S. V. Narasimhan, *J. Nucl. Mater.*, **393**, 120-125 (2009).
[2] H. P. Nawada, P. Sriramamurti, K. V. Govindan Kutty, S. Rajagopalan, R. B. Yadav, P. R. Rasudeva Rao and C. K. Mathews, *J. Nucl. Mater.*, **139**, 19-26 (1986).
[3] P. Martin, M. Ripert, T. Petit, T. Reich, C. Hennig, F. D’Acapito, J. L. Hazemann and O. Proux, *J. Nucl. Mater.*, **312**, 103-110 (2003).
[4] K. S. Kumar, T. Mathews, H. P. Nawada and N. P. Bhat, *J. Nucl. Mater.*, **324**, 177-182 (2004).
[5] T. L. Markin, R. S. Street and E. C. Crouch, *J. Inorg. Nucl. Chem.*, **32**, 59-75 (1970).
[6] Y. Hinatsu and J. Fujino, *Chem. Phys. Lett.*, **172**, 131-136 (1990).
[7] T. R. Griffiths, St. HV, A. Hubbard and M. J. Davies, *Inorg. Chim. Acta*, **225**, 305-317 (1994).
[8] S. -H. Kang, J. -D. Yi, H. -I. Yoo, S. -H. Kim and Y. W. Lee, *J. Phys. Chem. Solids*, **63**, 773-780 (2002).
[9] B. E. Hanken, C. R. Stanek, N. G-Jensen and M. Asta, *Phys. Rev. B*, **84**, 085131-1-085131-9 (2011).
[10] J. R. McBride, K. C. Hass, B. D. Poindexter and W. H. Weber, *J. Appl. Phys.*, **76**, 2435 (1994).

[11] L. Desgranges, Y. Pontillon, P. Matheron, M. Marcet, P. Simon, G. Guimbretière and F. Porcher, *Inorg. Chem.*, **51**, 9147-9149 (2012).
[12] Z. Talip, T. Wiss, P. E. Raison, J. Paillier, D. Manara, J. Somers and R. J. M. Konings, *J. Am. Ceram. Soc.*, **98**, 2278-2285 (2015).
[13] J. Lee, J. Kim, Y. -S. Youn, N. Liu, J. -G. Kim, Y. -K. Ha, D. W. Shoesmith and J. -Y. Kim, *J. Nucl. Mater.*, **486**, 216-221 (2017).
[14] M. Razdan and D. W. Shoesmith, *J. Electrochem. Soc.*, **161**, H105-H113 (2013).
[15] T. R. Ravindran and R. V. Krishnan, *Vib. Spectrosc.*, **73**, 97-101 (2014).
[16] J. Auborn and J. Choo, *Adv. Powder Metall. Part. Mater.*, **2**, 17-25 (1993).
[17] S. Fernández, M. I. Nieto, J. Cobos and R. Moreno, *J. Eur. Ceram. Soc.*, **36**, 3505-3512 (2016).
[18] A. Magneli, L. Kihlborg, *Acta Chem. Scand.*, **5**, 578-580 (1951).
[19] R. V. Krishnan, G. Panneerselvam, B. M. Singh, B. Kothandaram, G. Jogeswararao, M. P. Anthony and K. Nagarajan, *J. Nucl. Mater.*, **414**, 393-398 (2011).
[20] D. J. Kim, Y. S. Kim, S. H. Kim, J. H. Kim, J. H. Yang, Y. W. Lee and H. S. Kim, *Thermochim. Acta*, **441**, 127-131 (2006).
[21] R. D. Shannon, *Acta Cryst.*, A**32**, 751-767 (1976).
[22] R. K. Hailstone, A. G. DiFrancesco, J. G. Leong, T. D. Allston and K. J. Reed, *J. Phys. Chem. C*, **113**, 15155-15159 (2009).
[23] P. G. Marlow, J. P. Russell and J. R. Hardy, *Philos. Mag.*, **14**, 409-410 (1966).
[24] T. Livneh and E. Sterer, *Phys. Rev. B*, **73**, 085118-085119 (2006).
[25] V. G. Keramidas and W. B. White, *J. Chem. Phys.*, **59**, 1561-1562 (1973).
[26] P. R. Graves, *Appl. Spectrosc.*, **144**, 1665-1667 (1990).
[27] H. He and D. Shoesmith, *Phys. Chem. Chem. Phys.*, **12**, 8108-8117 (2010).
[28] G. Guimbretière, L. Desgranges, A. Canizares, G. Carlot, R. Caraballo, C. Jégou, F. Duval, N. Raimboux, M. R. Ammar and P. Simon, *Appl. Phys. Lett.*, **100**, 251914 (2012).
[29] J. M. Elorrieta, L. J. Bonales, N. Rodriguez-Villagra, V. G. Baonza and J. Cobos, *Phys. Chem. Chem. Phys.*, **18**, 28209-28216 (2016).
[30] L. Desgranges, G. Baldinozzi, P. Simon, G. Guimbretière and A. Canizares, *J. Raman Spectrosc.*, **43**, 455-458 (2012).
[31] I. Chang and S. Mitra, *Phys. Rev.*, **172**, 924 (1968).
[32] D. Peterson, A. Petrou, W. Giriat, A. Ramdas and S. Rodriguez, *Phys. Rev. B*, **33**, 1160 (1986).

[33] J. L. Jules and J. R. Lombardi, *J. Mol. Struct. (Theochem)*, **664-665**, 255–271 (2003).
[34] L. Genzel, T. P. Martin and C. H. Perry, *Phys. Stat. Sol.(b)*, **62**, 83-92 (1974).
[35] Z. Talip, S. Peuget, M. Magnin, L. Berardo, C. Valot, R. Vauchy and C. Jégou, *J. Raman Spectrosc.*, **48 (5)**, 765-772 (2017).
[36] C. Jégou, R. Caraballo, S. Peuget, D. Roudil, L. Desgranges and M. Magnin, *J. Nucl. Mater.*, **405**, 235-243 (2010).
[37] R. Böhler, M. J. Welland, D. Prieur, P. Cakir, T. Vitova, T. Pruessmann, I. Pidchenko, C. Hennig, C. Guéneau, R. J. M. Konings and D. Manara, *J. Nucl. Mater.*, **448**, 330-339 (2014).
[38] J. M. Elorrieta, D. Manara, L. J. Bonales, J. F. Vigier, O. Dieste, M. Naji, R. C. Belin, V. G. Baonza, R. J. M. Konings and J. Cobos, *J. Nucl. Mater.*, **495**, 484-491(2017).
[39] G. C. Allen, I. S. Butler and N. A. Tuan, *J. Nucl. Mater.*, **144**, 17-19 (1987).
[40] I. S. Butler, G. C. Allen and N. A. Tuan, *Appl. Spectrosc.*, **42 (5)**, 901-902 (1988).

Part 4

Overall conclusions

Taking into consideration the specific outcomes reflected throughout the scientific publications that compose this work (Part 3), certain overall inferences can be hereinafter drawn.

Above all, one thing has become clear: the feasibility of the Raman spectroscopy technique for obtaining reliable data on nuclear materials, with an obvious subtlety and safety advantage over other conventional techniques.

The performance of a detailed analysis on the Raman spectra acquired for the different characterised samples has allowed us to obtain relevant information on the studied materials.

In fact, the furnished data have demonstrated to be extremely valuable for gaining a better understanding of structural features at the local level, being capable of tracking the evolution of defects associated with oxygen incorporation during oxidation (Result 1 and Result 2), cations substitution (Result 5 and Result 6) or presence of vacancies (Result 6). In some cases, the completion of a quantitative analysis has even helped to test theoretical assumptions on structural transitions as well as to elaborate a specific method to characterise the oxidation degree of the samples (Result 1).

On the other hand, the Raman technique has proven to be pretty useful for *in situ* characterising the chemical reactions taking place on a given sample, either by making use of an external temperature controlled stage (Result 2) or by applying the developed Raman laser heating method (Result 3), placing special value on the role of temperature in both cases. In addition, fundamental analyses, such as those involving the *in situ* assessment of the Raman spectrum temperature dependence (Result 4), can be carried out with this technique.

Furthermore, it has been shown that Raman spectroscopy is highly reliable for evaluating the effect of the presence of transuranic elements on the SNF dioxide matrix oxidation, since its transformation to the various oxidation products can be easily and quickly monitored (Result 5 and Result 6).

All in all, the Raman technique can be regarded as an optimal tool for analysing the spent nuclear fuel condition and its stability against oxidation under dry interim storage conditions. In addition, its intrinsically non-contact nature and

versatility paves the way to use this technique for the assessment of the spent fuel condition at the time of its future retrieval from the temporary storage. Such a simple evaluation would enable properly and safely refurbishing the spent fuel either for its reprocessing or its final deep geological disposal.